Convergent organization of aberrant MYB complex controls oncogenic gene expression in acute myeloid leukemia

Sumiko Takao[1†], Lauren Forbes[1,2†], Masahiro Uni[1†], Shuyuan Cheng[1,2], Jose Mario Bello Pineda[3,4], Yusuke Tarumoto[5,6], Paolo Cifani[1], Gerard Minuesa[1], Celine Chen[1], Michael G. Kharas[1,2], Robert K. Bradley[3], Christopher R. Vakoc[5], Richard P. Koche[7], Alex Kentsis [1,2,8*]

[1] Molecular Pharmacology Program, Sloan Kettering Institute, New York, NY, USA.
[2] Departments of Pharmacology and Physiology & Biophysics, Weill Cornell Graduate School of Medical Sciences, Cornell University, New York, NY, USA.
[3] Computational Biology Program, Public Health Sciences Division, Fred Hutchinson Cancer Research Center, Seattle, WA, USA; Basic Sciences Division, Fred Hutchinson Cancer Research Center, Seattle, WA, USA; Department of Genome Sciences, University of Washington, Seattle, WA, USA.
[4] Medical Scientist Training Program, University of Washington, Seattle, WA, USA
[5] Cold Spring Harbor Laboratory, Cold Spring Harbor, NY, USA.
[6] Institute for Frontier Life and Medical Sciences, Kyoto University, Kyoto, Japan
[7] Center for Epigenetics Research, Sloan Kettering Institute, New York, NY, USA.
[8] Tow Center for Developmental Oncology, Department of Pediatrics, Memorial Sloan Kettering Cancer Center, New York, NY, USA.

[†] These authors contributed equally to this work

* Correspondence: kentsisresearchgroup@gmail.com, @KentsisResearch

ABSTRACT

Dysregulated gene expression contributes to most prevalent features in human cancers. Here, we show that most subtypes of acute myeloid leukemia (AML) depend on the aberrant assembly of MYB transcriptional co-activator complex. By rapid and selective peptidomimetic interference with the binding of CBP/P300 to MYB, but not CREB or MLL1, we find that the leukemic functions of MYB are mediated by CBP/P300 co-activation of a distinct set of transcription factor complexes. These MYB complexes assemble aberrantly with LYL1, E2A, C/EBP family members, LMO2 and SATB1. They are organized convergently in genetically diverse subtypes of AML, and are at least in part associated with inappropriate transcription factor co-expression. Peptidomimetic remodeling of oncogenic MYB complexes is accompanied by specific proteolysis and dynamic redistribution of CBP/P300 with alternative transcription factors such as RUNX1 to induce myeloid differentiation and apoptosis. Thus, aberrant assembly and sequestration of MYB:CBP/P300 complexes provide a unifying mechanism of oncogenic gene expression in AML. This work establishes a compelling strategy for their pharmacologic reprogramming and therapeutic targeting for diverse leukemias and possibly other human cancers caused by dysregulated gene control.

INTRODUCTION

Gene dysregulation is one of the most prevalent features in human cancers (Bradner et al., 2017). In many tumors, this is due to the pathogenic mutations of promoters, enhancers, and genes encoding either transcription factors or factors that regulate chromatin and gene expression. In blood cancers, and acute myeloid leukemias (AML) in particular, aberrant gene expression is thought to contribute to most important properties of leukemia cells, including self-renewal, growth, and resistance to therapy. For example, numerous pathogenic chromosomal translocations in AML, such as those involving *AML1* (*RUNX1*) and *MLL1* (*KMT2A*) produce chimeric transcription or chromatin remodeling factors that cause disease (Look, 1997). Consequently, therapeutic strategies aimed at restoring normal gene expression are compelling because of their ability to target the causal molecular processes and induce leukemia cell differentiation and elimination, leading in principle to durable disease control.

While specific molecular dependencies have been identified for some genetic subtypes of AML, such as DOT1L or Menin inhibition for *MLL*-rearranged leukemias (Krivtsov et al., 2019), and CARM1 inhibition for *AML1*-rearranged leukemias (Greenblatt et al., 2019), distinct pathogenetic mechanisms of diverse AML subtypes also appear to converge on shared molecular pathways. For example, approximately 25% of adult and childhood AMLs, including both *MLL*-rearranged and non-rearranged cases, require aberrant activation of the transcription factor MEF2C, conferring susceptibility to MARK and SIK inhibitors, which are currently being explored for clinical trials for patients (Brown et al., 2018; Tarumoto et al., 2018; Vakoc & Kentsis, 2018). Similarly, nearly 50% of examined AML specimens exhibit aberrant activation of HGF/MET/FGFR signaling (Kentsis et al., 2012), and are being currently targeted therapeutically in the ongoing clinical trial of combined MET and FGFR inhibitors in patients with relapsed or refractory AML (ClinicalTrials.gov Identifier NCT03125239). Even for therapies targeting leukemogenic proteins directly, such as inhibitors of IDH1/2, FLT3, KIT, SYK, as well as epigenetic and apoptotic therapies such as decitabine and venetoclax, their therapeutic efficacy and resistance depend on the underlying gene expression phenotypic states of AML cells (Tyner et al., 2018). Thus, there is intense interest in defining shared molecular dependencies controlling leukemogenic gene expression in AML that can provide effective therapeutic options for patients.

Recently, MYB has emerged as a therapeutic target in AML, as transient suppression of *Myb* nearly completely eliminates leukemia development in mouse models *in vivo* while sparing normal hematopoietic cells (Zuber, Rappaport, et al., 2011). Indeed, pioneering studies have implicated Myb as a key mediator of leukemias (Klempnauer & Bishop, 1984; Luger et al., 2002). MYB is the cellular homologue of the viral *v-Myb* oncogene that can cause avian leukemias and function as a pioneer transcription factor in mammalian cells (Biedenkapp et al., 1988). MYB functions as a master regulator of gene expression in diverse cell types, including hematopoietic cells where it controls cell proliferation and differentiation (Ramsay and Gonda, 2008). Both mutations and translocations of *MYB* have causal roles in various human malignancies, including leukemias. For example, aberrant expression of *TAL1* in T-cell acute lymphoid leukemia (T-ALL) is induced by pathogenic somatic mutations that create neomorphic MYB binding sites (Mansour et al., 2014). Likewise, *MYB* is recurrently rearranged in distinct subtype of blastic plasmacytoid dendritic cell neoplasms (BPDCN), a highly refractory hematologic malignancy (Suzuki et al., 2017).

Notably, the *Booreana* strain of mice that impairs the binding of Myb by its co-activator CBP/P300 (Crebbp/Ep300) due to the mutation of Myb E308G in its transcriptional activation domain is resistant to leukemogenesis induced by the otherwise fully penetrant *MLL-AF9* and *AML1-ETO* oncogenes, but has largely normal hematopoiesis (Diwakar R. Pattabiraman et al., 2014). Altogether, these findings indicate that MYB and its co-factor CBP/P300 are fundamentally dysregulated in AML, presumably through disordered gene expression that characterizes most

forms of this disease. However, the specific details of this mechanism remain poorly understood, largely due to the lack of suitable tools.

Recently, we developed a peptidomimetic inhibitor of MYB:CBP/P300 (Ramaswamy et al., 2018). Here, we report its second-generation version that has significantly increased potency, and consequently suppresses leukemic MYB functions in most AML subtypes tested, while relatively sparing normal hematopoietic progenitor cells. By rapid and selective peptidomimetic interference with the binding of CBP/P300 to MYB, but not CREB or MLL1, we find that the leukemic functions of MYB are mediated by CBP/P300-mediated co-activation of a distinct set of transcriptional factor complexes that are aberrantly assembled with MYB in AML cells, which is associated at least in part with their inappropriate expression. This therapeutic remodeling is accompanied by dynamic redistribution of CBP/P300 complexes to genes that control cellular differentiation and growth. These findings provide a unifying mechanism of oncogenic gene control, involving aberrant assembly of transcription factor complexes and sequestration of CBP/P300 to promote oncogenic gene expression and block cellular differentiation. This paradigm should apply to other human cancers caused by dysregulated gene control, elucidate specific molecular determinants of leukemia pathogenesis, and enable the development of definitive therapies for patients.

RESULTS

Genome-wide CRISPR screen identifies CBP requirement for the susceptibility of AML cells to peptidomimetic blockade of MYB:CBP/P300

In prior work, we used genetic and structural evidence to design a peptidomimetic inhibitor of the MYB:CBP/P300 transcription coactivation complex, termed MYBMIM (Ramaswamy et al., 2018). To elucidate its mechanisms of action in an unbiased manner, we carried out a genome-wide CRISPR knockout screen to identify genes whose depletion affects the susceptibility of AML cells to MYBMIM. We used MOLM13 cells stably expressing Cas9 and transduced them with lentiviruses encoding the genome-wide GeCKOv2 library at a multiplicity of infection of 0.3 (Figure 1A). Following selection of transduced cells, we treated them with MYBMIM or PBS control in independent biological replicates, and quantified the enrichment and depletion of cell clones expressing specific sgRNAs by DNA sequencing of lentiviral barcodes (Figure 1A). This screen revealed a variety of genes whose depletion confers relative resistance

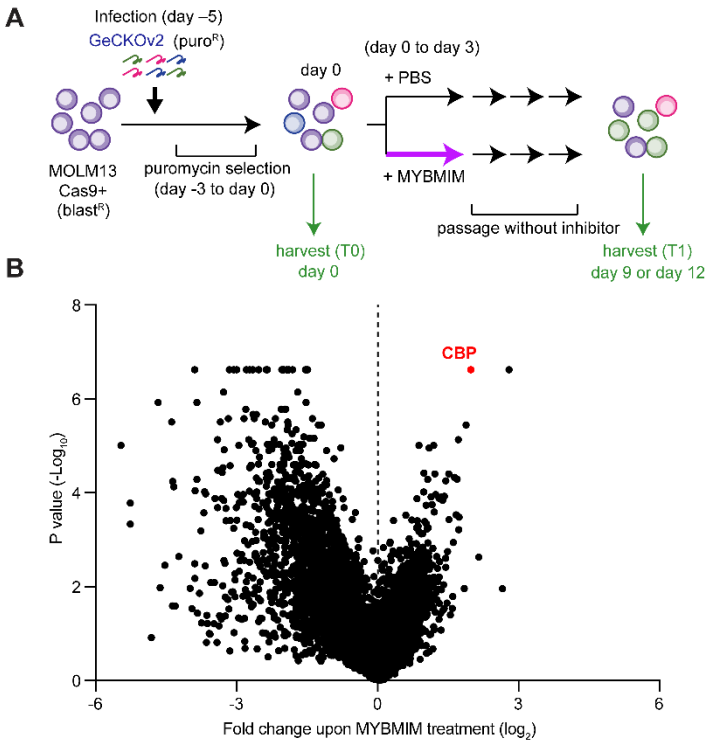

Figure 1. CBP depletion is required to confer resistance to MYBMIM in AML cells. (A) Schematic of the genome-wide CRISPR screen to identify genes whose loss modifies MYBMIM effects in MOLM13 cells expressing Cas9. Cells were transduced with the GeCKOv2 library expressing single sgRNAs at low multiplicity of infection, followed by 3-day treatment with 10 μM MYBMIM versus PBS control, with the sgRNA representation assessed by DNA sequencing. **(B)** Volcano plot showing the relative abundance of cell clones expressing sgRNAs targeting specific genes (fold change of MYBMIM-treated cells at T1 versus T0) and their statistical significance from biological replicates. Dashed line represents no enrichment, with positive values representing genes whose depletion confers relative resistance to MYBMIM. CBP is marked in red.

and susceptibility to MYBMIM treatment, consistent with the presence of diverse cellular pathways that regulate oncogenic gene expression (Supplementary File 2a). The most significantly affected gene whose depletion was required to confer resistance to MYBMIM was *CBP* (Figure 1B). In contrast, CBP depletion exhibited no enrichment upon PBS treatment (Figure 1-figure supplement 1). Thus, MYBMIM is a specific inhibitor of MYB:CBP, and emphasizes the exquisite specificity of peptidomimetic inhibitors as pharmacologic modulators of protein interactions.

CRYBMIM is a peptidomimetic chimera that specifically binds CBP/P300 KIX domain

Of all the functional genetic dependencies examined to date, the transcription factor *MYB* demonstrates the broadest dependency across diverse AML subtypes, as compared to other non-hematopoietic cancers (Tarumoto et al., 2018). To generalize this analysis, we queried 688 human cancer cell lines tested as part of the DepMap Cancer Dependency Map to identify genes that are selectively required for the growth and survival of leukemia as compared to other cancer types. We found that *MYB* is the most significantly required human gene in 37 leukemia cell lines, including 20 AML cell lines, of diverse molecular subtypes (p = 1.1e-15; Figure 2A).

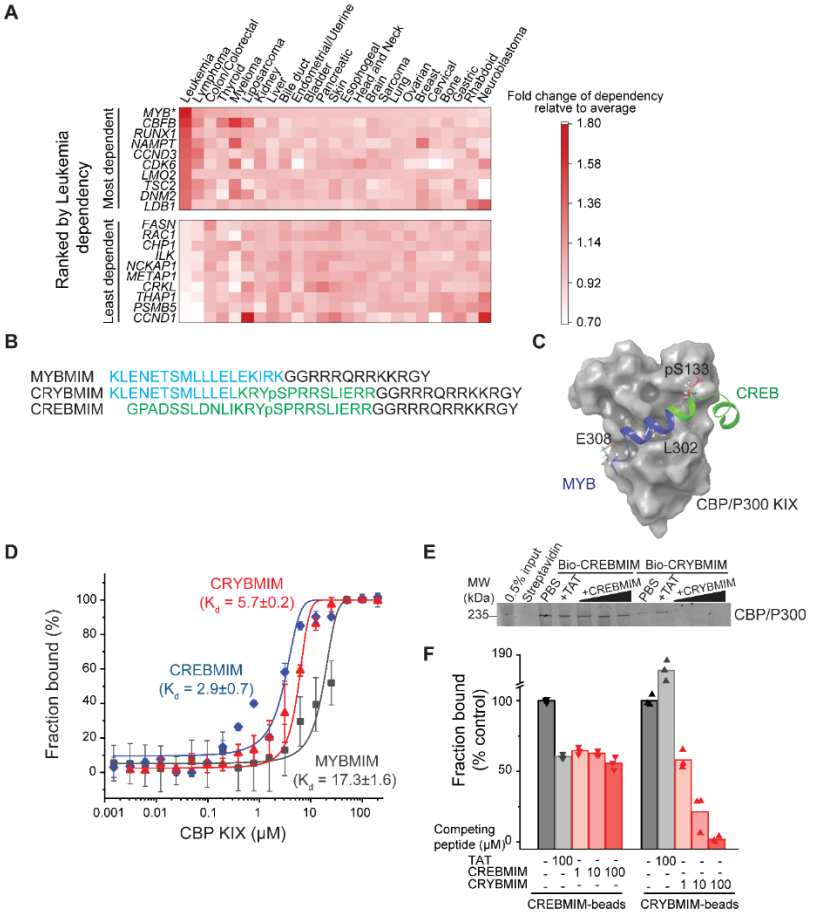

Figure 2. CRYBMIM is an improved peptidomimetic chimera that specifically binds the KIX domain of CBP/P300 in vitro and in cells. (A) Heatmap of the top 10 and bottom 10 gene dependencies for survival and proliferation of 652 cancer cell lines in the DepMap Cancer Dependency Map Project, ranked by the greatest dependency for 37 leukemia lines, 20 of which are AML cell lines, as indicated by the red color gradient; * p = 1.1e-15, t-test of leukemia versus other tumor types. **(B)** Retro-inverso amino acid sequences of MYBMIM, CREBMIM and CRYBMIM, with amino acids derived from MYB, CREB, and TAT marked in blue, green, and black, respectively. **(C)** Molecular model of the CRYBMIM:KIX complex. Residues making contact with KIX are labeled, with portions derived from MYB and CREB marked in blue and green, respectively. **(D)** Binding of FITC-conjugated CREBMIM (blue), CRYBMIM (red), and MYBMIM (black), as measured using microscale thermophoresis; Kd = 2.9 ± 0.7, 5.7 ± 0.2, and 17.3 ± 1.6, respectively. Error bars represent standard deviations of three biological replicates; p < 1e-15, ANOVA, for CRYBMIM versus MYBMIM. **(E)** Western blot showing binding of nuclear CBP/P300 isolated from AML cells to biotinylated CRYBMIM or CREBMIM, specifically competed by the excess free peptides as indicated. **(F)** Quantification of CBP/P300 binding to CRYBMIM and CREBMIM by fluorescence densitometry, with black, gray and red denoting PBS control, TAT control, and peptide competition, respectively.

MYB target gene activation requires its specific interaction with CREB-binding protein (CBP)/P300 for co-activation (Dai et al., 1996). The helical MYB transactivation domain comprising residues 293-310 binds to the KIX domain of CBP/P300 (Zor et al., 2004). Using molecular mechanics simulations, we previously developed a peptidomimetic inhibitor of this interaction, termed MYBMIM (Ramaswamy et al., 2018). MYBMIM uses stereoselective substitution of D-amino acids to confer proteolytic stability, and the cationic TAT domain for cell penetration. As a result, MYBMIM can specifically inhibit MYB:CBP/P300 binding in cells, but its activity is less pronounced in non-MLL-rearranged AML cells (Ramaswamy et al., 2018). Given that MYBMIM bound to recombinant CBP KIX domain with the dissociation constant of 21.3 ± 2.9 μM, as compared to the native MYB peptide of 4.2 ± 0.5 μM (Ramaswamy et al., 2018), we reasoned that a peptidomimetic inhibitor with higher affinity to CBP/P300 would be more effective.

Consequently, we used molecular modeling to extend MYBMIM into the adjoining binding site that binds CREB (Radhakrishnan et al., 1997; Cheng et al., 2008). We appended CREB residues 124-147 to MYBMIM, while replacing the EKIRK motif to maintain favorable backbone geometry, as confirmed by molecular energy minimization calculations in implicit solvent (Figures 2B, 2C and Figure 2-figure supplement 1). Termed CRYBMIM, this design preserves key MYB residues implicated in leukemic transformation, including E308 which forms a salt bridge with CBP, while including the pS133-containing portion of CREB that is responsible for its high affinity binding to CBP (Zor et al., 2004)(J. C. Cheng et al., 2008; Radhakrishnan et al., 1997). Similarly, we also designed two additional peptidomimetic inhibitors targeting the distinct CREB and MLL1 binding sites that are proximal to but non-overlapping with the MYB binding site, termed CREBMIM and MLLMIM, respectively (Figures 2B, 2C and Figure 2-figure supplement 1A-C).

As expected, both CRYBMIM and CREBMIM bind to the purified recombinant CBP KIX domain with significantly improved (3-6 fold) affinities as compared to MYBMIM and measured by microscale thermophoresis (K_d of 5.7 ± 0.2 μM, 2.9 ± 0.7 μM, and 17.3 ± 1.6 μM, p = 1e-15; Figure 2D). To confirm these peptides can bind the CBP/P300 complex from cells, we immobilized biotinylated CRYBMIM and CREBMIM peptides on streptavidin beads and used them to affinity purify CBP/P300 from non-denatured nuclear extracts of MV411 AML cells. Consistently, we observed efficient binding of nuclear CBP/P300 to peptide-conjugated but not control streptavidin beads (Figure 2E). We found that increasing concentrations of free CRYBMIM could compete with the binding of CBP/P300 to immobilized CRYBMIM, with the apparent K_i of approximately 4.7 μM based on quantitative fluorescence densitometry measurements (Figure 2F). We confirmed the specificity of this binding by incubating bound complexes with 100-fold excess of TAT control peptides, which demonstrated no measurable displacement as compared to PBS control (Figure 2E-F). In contrast, excess CREBMIM was significantly less effective at displacing CBP/P300 from immobilized CREBMIM (apparent K_i > 100 μM, Figure 2E-F), consistent with the much higher nM affinity and allosteric effects that characterize the CREB:CBP/P300 interaction (Goto et al., 2002; Radhakrishnan et al., 1997). This is also consistent with the presence of distinct CBP transcription factor complexes in AML cells, some of which (MYB) are susceptible to peptidomimetic blockade, and others (CREB) exhibiting more stable interactions. Importantly, CRYBMIM binds CBP/P300 specifically, as exposure of AML cell extracts to streptavidin-immobilized biotinylated CRYBMIM leads to efficient binding to CBP/P300, but not MED15 which is highly expressed in MV411 AML cells and contains a known KIX domain with the closest sequence similarity to CBP/P300 (38 % identity; Figure 2-figure supplement 1D-E). Thus, CRYBMIM is a specific high-affinity inhibitor of MYB:CBP/P300 binding.

Potent and broad-spectrum activity of CRYBMIM against diverse subtypes of AML

To confirm that CRYBMIM maintains effective cell penetration and nuclear accumulation in AML cells, we studied its fluorescein isothiocyanate (FITC)-conjugated derivative using live cell confocal fluorescence microscopy (Figure 3A). Consistently, we observed that both FITC-CRYBMIM and FITC-CREBMIM efficiently localized to the nuclei of MV411 AML cells within one hour of peptide treatment (Figure 3A). We confirmed specific nuclear accumulation of CRYBMIM as opposed to non-specific membrane binding that can affect TAT-containing peptides by confocal sub-cellular imaging of cells co-stained with specific mitochondrial and nuclear dyes (Figure 3A).

Previously, we observed that MYBMIM blocks the binding of MYB to CBP/P300 in AML cells, requiring relatively high 20 μM concentrations for three hours to achieve this effect (Ramaswamy et al., 2018). To ascertain whether CRYBMIM can achieve more potent interference with the binding of MYB to the CBP/P300 complex in cells due to its improved affinity as compared

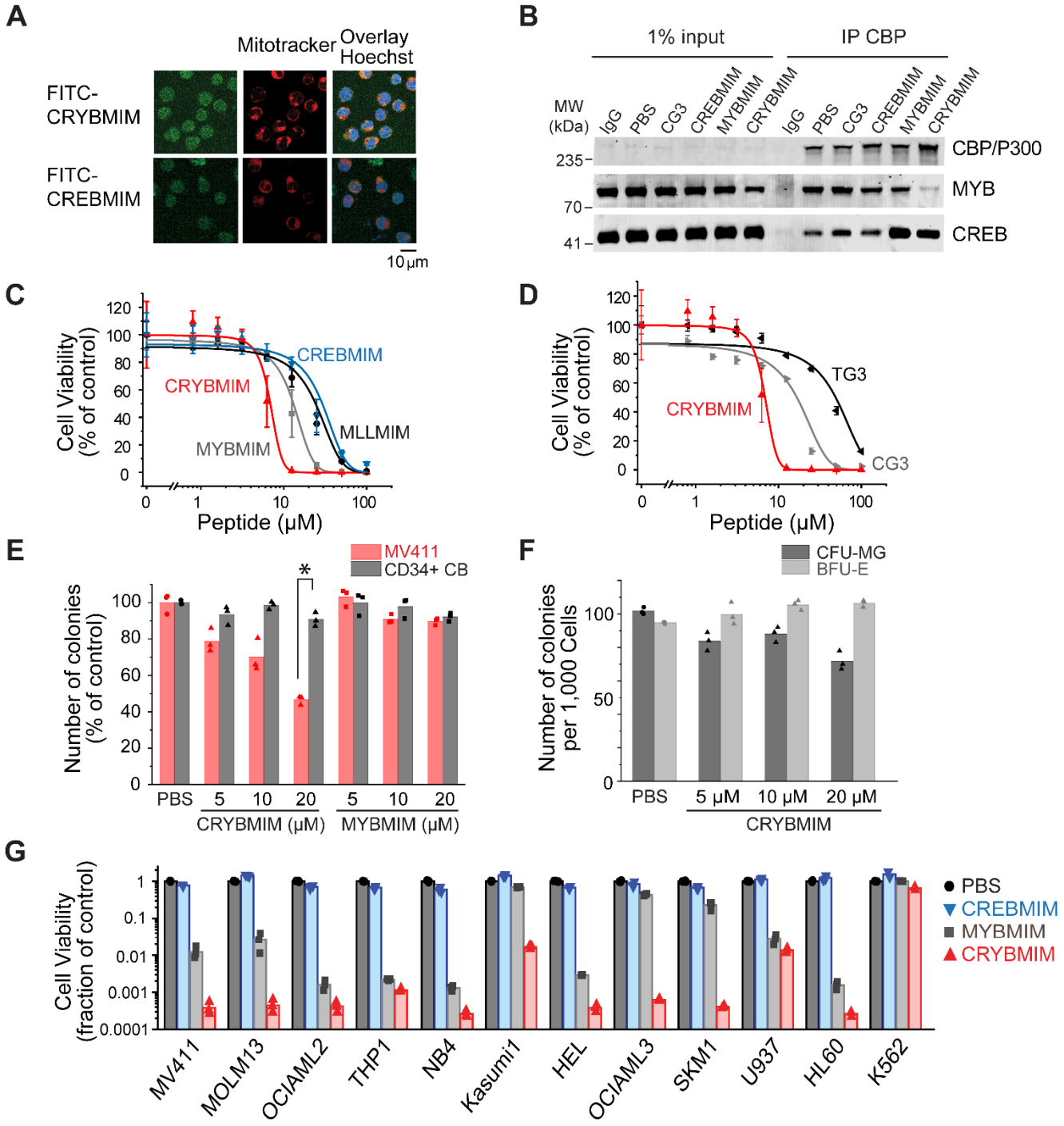

Figure 3. Potent and broad-spectrum activity of CRYBMIM against diverse AML cell lines but relatively sparing of normal hematopoietic progenitor cells. (A) Representative live cell confocal microscopy images of MV411 cells treated with 100 nM FITC-conjugated peptides as indicated for 1 hour, counterstained with Mitotracker (red) and Hoechst 33342 (blue). Scale bar indicates 20 µm, with z-stack of 1.5 µm. **(B)** Western blots showing immunoprecipitated nuclear CBP/P300 co-purified with MYB and CREB from MV411 cells treated with 10 µM peptides as indicated for 1 hour. **(C-D)** Cell viability of MV411 cells as a function of increasing concentrations of 48-hour peptide treatment, comparing (C) CRYBMIM to MYBMIM, CREBMIM and MLLMIM (IC50 = 6.88 ± 3.39, 13.1 ± 3.3 29.15 ± 3.79, and 24.22 ± 2.00, $p < 1e-15$, ANOVA); (D) TG3 and CG3 (IC50 = 16.65 ± 1.00 and 48.91 ± 2.55, $p < 1e-15$, ANOVA). Error bars represent standard deviation of three biological replicates. **(E)** Colony forming ability of CD34+ cells isolated from human umbilical cord blood (CD34+ CB, gray) and MV411 AML (red) cells following CRYBMIM or MYBMIM treatment. Data represent three biological replicates; *$p = 7.4e-5$, t-test of normal CD34+ CB versus MV411 AML cells. **(F)** Preservation of clonogenic capacity of CD34+ CB cells in differentiating into erythroid blast forming units (BFU-E, light gray) and granulocyte macrophage colony forming units (CFU-GM, gray) as a function of CRYBMIM treatment. **(G)** Cell viability of AML cell lines treated with control PBS (black), 20 µM CREBMIM (blue), MYBMIM (gray), or CRYBMIM (red) as indicated for 6 days with media replacement every 48 hours in three biological replicates ($p = 8.6e-3$, t-test for CRYBMIM versus control).

immunoprecipitated CBP/P300 using specific antibodies (Figure 3B). Under these more stringent conditions, we found that CRYBMIM is indeed more potent compared to MYBMIM, as evidenced by the substantial depletion of MYB from the immunoprecipitated CBP/P300 complex by CRYBMIM but not MYBMIM under these conditions (Figure 3B).

This effect was specific because the inactive analogue of CRYBMIM, termed CG3, in which 3 key residues have been replaced with glycines (Supplementary File 1a), was unable to compete with MYB:CBP/P300 binding in cells, an effect observed with CBP/P300-specific but not control isotype non-specific antibodies (Figure 3B). Neither CREBMIM nor CRYBMIM treatment interfered with the binding of CREB to the cellular CBP/P300 complex (Figure 3B), in agreement with the affinities of their direct binding to the recombinant CBP KIX domain (Figures 2D-F), the nM affinity of CREB:CBP/P300 interaction (Radhakrishnan et al., 1997), and the specific molecular features required for MYB but not CREB or MLL1 binding (Figure 2C and Figure 2-figure supplement 1).

To test the prediction that higher affinity binding of CRYBMIM to CBP/P300 would translate into improved anti-leukemia potency, we assessed its effects on the viability of cultured human leukemia and normal hematopoietic cells. Consistent with this prediction, we observed that CRYBMIM exhibited significantly higher potency against MV411 AML cells, as compared to MYBMIM as well as CREBMIM and MLLMIM (IC_{50} = 6.9 ± 3.4 μM, 13 ± 3.3, 29 ± 3.8 μM, and 24 ± 2.0 μM, p = 1e-15; Figure 3C). We confirmed CRYBMIM's specificity by analyzing its inactive analogue CG3 and MYBMIM's inactive analogue TG3, in which 3 residues forming key electrostatic and hydrophobic interactions with the KIX domain were replaced by glycines; both exhibited significantly reduced activity (IC_{50} of 17 ± 1.0 μM and 49 ± 2.6 μM, p = 2.75e-4 and <1e-15, respectively; Figure 3D). To assess the effects of CRYBMIM on normal hematopoietic progenitor cells, we used primary human CD34+ umbilical cord progenitor cells, cultured in serum-free medium in methylcellulose, as well as in liquid culture (Figure 3-figure supplement 1D). We observed minimal effects on the clonogenic growth of normal progenitor cells, as compared to that of MV411 AML cells which was significantly suppressed (91 ± 3.8 % versus 47 ± 2.4 % colonies, p = 1e-4; Figure 3E and Figure 3-figure supplement 1A). Extending the duration of treatment led to small reduction of myeloid/granulocyte progenitors, and an increase in erythroid progenitor colony-forming units (70.5 ± 5.6 % and 112.3 ± 2.2%, respectively; Figure 3F). In contrast, doxorubicin, which is commonly used to treat AML, caused significant and substantial impairments in the clonogenic capacity of all hematopoietic progenitor cells (Figure 3-figure supplement 1B-C). Thus, CRYBMIM exhibits improved anti-leukemia activity, while relatively sparing normal blood cells.

Importantly, CRYBMIM achieved significantly improved, logarithmic suppression of growth and survival of most AML cell lines tested, as compared to MYBMIM and CREBMIM (Figure 3G). For example, whereas MYBMIM induced nearly 100-fold suppression of growth of MV411 cells after six days of treatment in agreement with prior studies (Ramaswamy et al., 2018), CRYBMIM achieved more than 1,000-fold suppression compared to control (p = 8.6e-3; Figure 3G), consistent with its improved biochemical affinity (Figure 2D). This improved activity of CRYBMIM spanned diverse AML subtypes, including *MLL*-rearranged, *AML1-ETO* translocated, *PML-RARA*-translocated, *DNMT3A*-mutant, *NPM1c*-mutant, *TP53*-mutant, *MYC*-amplified, and *WT1*-mutant cell lines, with the exception of erythroblastic *BCR-ABL1*-translocated K562 cells (10 of 11 cell lines tested; Figure 3G and Supplementary File 1b). In contrast, under these conditions, CRYBMIM had no significant effects on the growth and differentiation of normal human umbilical cord blood progenitor cells *in vitro* (Figure 3E, 3F and Figure 3-figure supplement 1A). Interestingly, CRYBMIM also exhibited anti-tumor effects on various solid tumor cell lines, including some medulloblastoma, neuroblastoma, and breast carcinoma cells, at least some of which also exhibit high levels of *MYB* expression and genetic dependence (Figures 3-figure supplement 2A-B). In all, CRYBMIM has broad spectrum activity against diverse subtypes of AML, while relatively sparing normal hematopoietic cells.

CBP is specifically required for susceptibility of AML cells to peptidomimetic MYB blockade

CBP and EP300 are closely related transcriptional coactivators with distinct activities in cells. To precisely define their contributions, we used CRISPR interference to elucidate their requirements for susceptibility to CRYBMIM (Figure 4A). We used MV411, MOLM13, OCIAML3, and K562 AML cells that stably express Cas9 and transduced them with mCherry or GFP-expressing lentiviruses encoding specific and independent sgRNAs targeting *CBP* and *EP300*, as compared to the *AAVS1* safe harbor locus and *CDK1* that is required for cell survival, as negative and positive controls, respectively. We confirmed specific depletion of the majority of CBP protein by Western immunoblotting in cells expressing sgCBP-1 and sgCBP-2 with intact EP300 expression, but not those not transduced with sgRNA lentiviruses or those expressing sgNEG-1 and sgNEG-2 (Figure 4B). We found that depletion of *EP300* caused gradual decrease in cell proliferation over 3-6 days (Figure 4-figure supplement 1A-C), whereas depletion of *CDK1* caused acute cell cycle arrest and apoptosis (Figure 4-figure supplement 1A-C). In contrast, depletion of *CBP* had no significant effects on steady-state cell fitness, but caused significant resistance to CRYBMIM, where CBP-deficient cells outcompeted their non-transduced counterparts when treated with CRYBMIM (p = 6.0e-10 and 4.0e-8 for sgCBP-1 and sgCBP-2 in MOLM13 cells, respectively, and 1.1e-6 and 3.7e-6 for MV411 cells; Figure 4C-D). In contrast, K562 cells that are mostly resistant to CRYBMIM exhibited selective fitness upon depletion of EP300 (Figure 4-figure supplement 1D). This suggests that CBP and EP300 contribute to distinct gene expression programs, presumably as part of specific transcription

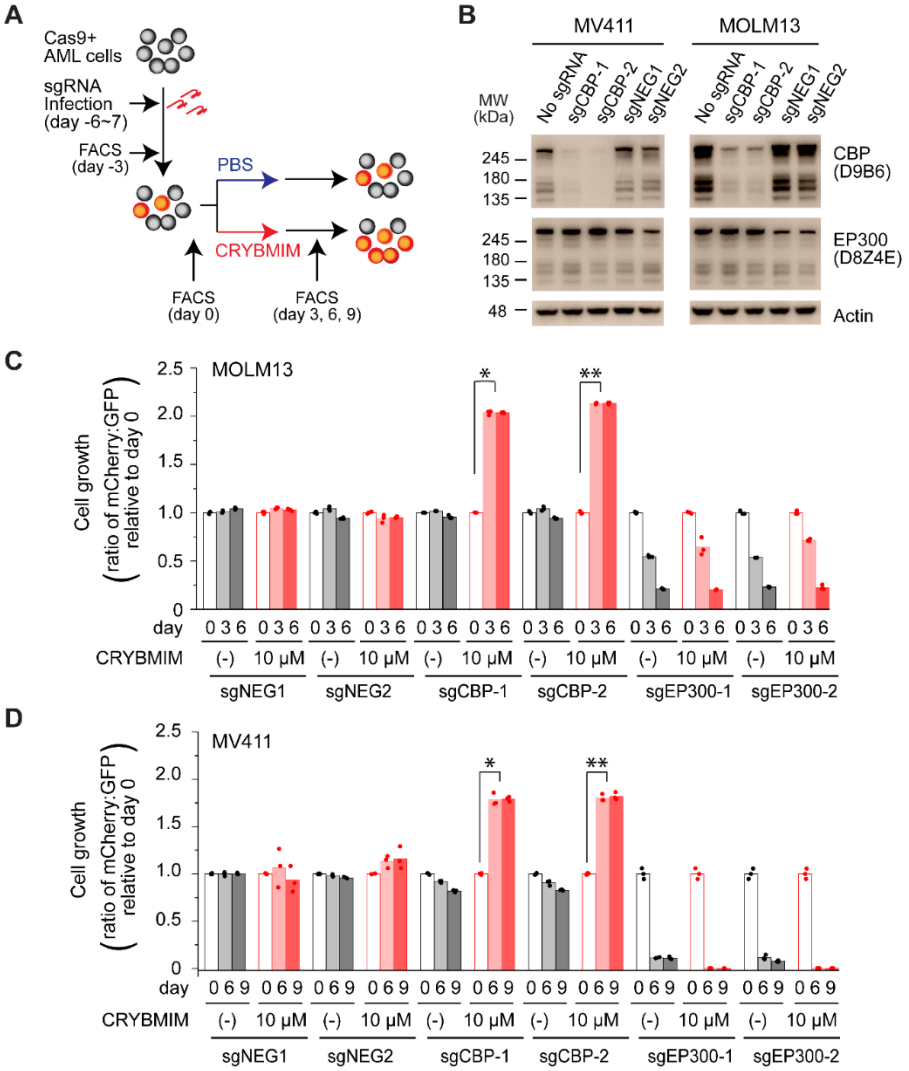

Figure 4. CBP but not P300 is dispensable for the growth and survival of AML cells, and is required for the susceptibility to peptidomimetic MYB blockade by CRYBMIM. (A) Schematic of the competitive assays to define specific genetic dependencies. AML cells expressing Cas9 and GFP are transduced with sgRNAs targeting specific genes and expressing mCherry, followed by quantitation of cell abundance by fluorescence activated cell scanning (FACS) of GFP and mCherry-expressing cells. **(B)** Western blots demonstrating specific depletion of CBP in MV411 (left) and MOLM13 (right) cells expressing sgCBP-1 and sgCBP-2, as compared to control sgNEG1 and sgNEG2 targeting the AAVS1 safe harbor locus. EP300 is shown for specificity, and Actin serves as the loading control. **(C)** Relative growth of GFP-expressing MOLM13 cells expressing mCherry and unique sgRNAs targeting AAVS1 control (sgNEG1 and sgNEG2), CBP (sgCBP-1 and sgCBP-2), and P300 (sgEP300-1 and sgEP300-2) and quantified by FACS on day 0, 3, and 6 after two-day treatment with 10 μM CRYBMIM or PBS. Data represent biological triplicates of at least 10,000 cells per condition; *p = 6.0e-10, **p = 4.1e-8, t-test for day 6 versus day 0 of CRYBMIM treatment of CBP-depleted cells. **(D)** Analogous experiment as (C) using MV411 cells; *p = 1.1e-6, **p = 3.7e-6, t-test for day 6 versus day 0 of CRYBMIM treatment of CBP-depleted cells.

factor complexes, as required for their susceptibility to peptidomimetic blockade.

CRYBMIM blocks oncogenic MYB gene expression and restores normal myeloid cell differentiation

The assembly of MYB with CBP/P300 controls gene expression in part due to its transcriptional co-activation at specific enhancers and promoters (Kasper et al., 2010; Zhao et al., 2011). Previously, we found that MYBMIM can suppress MYB:CBP/P300-dependent gene expression, leading to AML cell apoptosis that required MYB-mediated suppression of *BCL2* (Ramaswamy et al., 2018). However, because MYBMIM's suppression of gene expression was accompanied mostly by apoptosis, we were unable to discern the molecular mechanisms that directly dysregulate the activity of the CBP/P300 transcription factor complex in AML cells.

Given that CRYBMIM has increased affinity for CBP/P300 similar to that of native MYB (5.7 ± 0.2 μM and 4.2 ± 0.5 μM, respectively), we reasoned that its improved activity would now permit detailed kinetic studies to define the specific gene expression programs that are aberrantly activated in AML cells. Consistent with this prediction, comparison of the effects of CRYBMIM on gene expression and consequent apoptosis of MV411 cells revealed that one and four hour exposures led to significant changes in gene expression with minimal induction of apoptosis (Figure 5-figure supplement 1). Thus, we used RNA-sequencing (RNA-seq) to define the changes on gene expression genome-wide upon one and four hour exposures to CRYBMIM as compared to PBS control (Figures 5A-B). We found that after four-hour duration of treatment, CRYBMIM causes significant downregulation of 2,869 genes, including known MYB target genes *MYC, IKZF1, GATA2,* and *KIT* (Figures 5A-5C, Supplementary File 2b-e). Similar to MYBMIM, CRYBMIM also caused significant upregulation of distinct genes, an effect that was substantially more pronounced upon four hours of treatment (4,099 genes; 5A-B, Supplementary File 2b-e). Interestingly, in addition to the expected suppression of MYB target genes (Figure 5C), gene set enrichment analysis also revealed significant induction of myeloid and monocyte differentiation programs (Figures 5D-5E and Supplementary File 2f). These

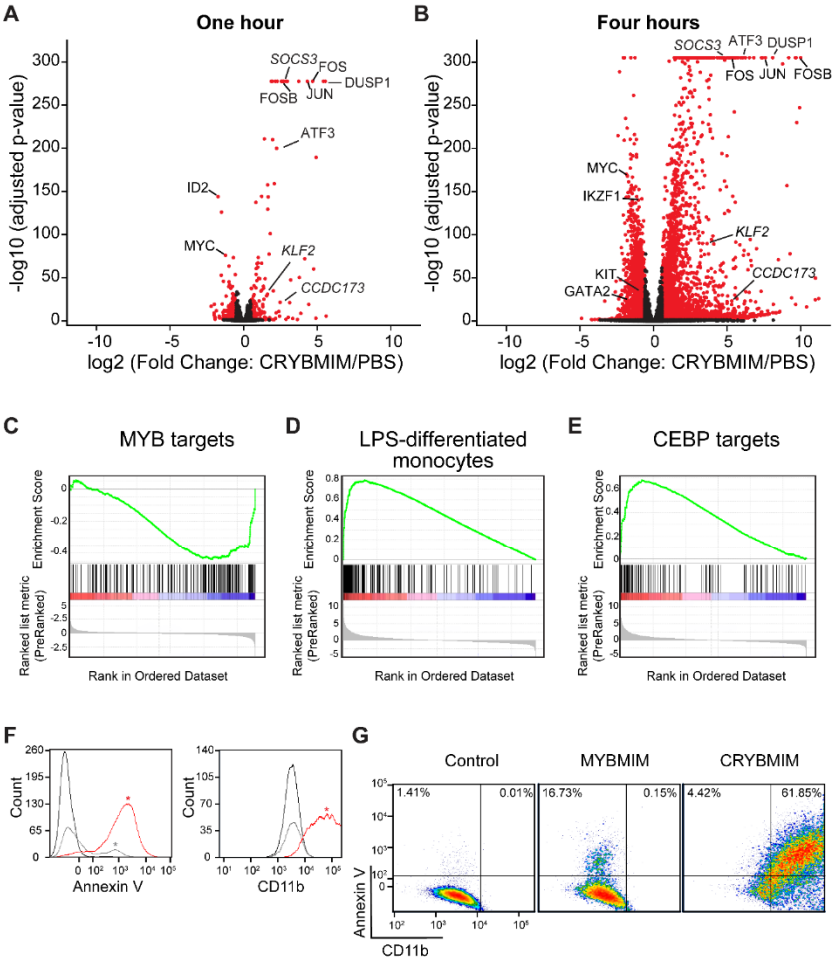

Figure 5. CRYBMIM blocks oncogenic MYB gene expression and restores normal myeloid cell differentiation. (A-B) Volcano plots of normalized gene expression of MV411 cells upon one (A) and four hour (B) treatment with CRYBMIM, as compared to PBS control, with select genes labeled; p-values denote statistical significance of 3 biological replicates. **(C-E)** Gene set enrichment analysis of up- and down-regulated gene sets: (C) MYB_Q6, (D) GSE9988_LPS_VS_VEHICLE_TREATED_MONOCYTES_UP, and (E) GERY_CEBP_TARGETS_377. **(F)** Histogram of Annexin V- or CD11b-stained MV411 cell fluorescence, treated with CRYBMIM (red), MYBMIM (gray), or control PBS (black); * p < 1e-15, Kruskal-Wallis test. **(G)** Scatter plots comparing Annexin V- versus CD11b-stained MV411 cell fluorescence, treated with control PBS, MYBMIM or CRYBMIM; blue to red color indicates increasing cell density.

effects were specific because in contrast to CRYBMIM, CREBMIM treatment exhibited minimal changes in gene expression (Figure 5-figure supplement 1C), consistent with its inability to disrupt the cellular CBP/P300 complex (Figure 3B). For example, CRYBMIM induced significant increases in the AP-1 family transcription factors *FOS* and *JUN*, as well as *IL6* and *CSF1* that control myeloid differentiation (Figure 5B) (Gonda et al., 1993; Selvakumaran et al., 1992). Nearly 40% of the genes induced by deletion of RUVBL2 were also found to be induced by CRYBMIM treatment, including *JUN*, *FOS* and *FOSB* (Armenteros-Monterroso et al., 2019). In agreement with these findings, CRYBMIM treatment induced significant phenotypic differentiation of MV411 cells, as evidenced by the induction of monocytic CD11b expression, as measured by flow cytometry (Figure 5F-G). While MYBMIM primarily induces apoptosis of MV411 cells, CRYBMIM effects include both apoptosis and differentiation, as evident from flow cytometry analyses (Figure 5G). This suggests that differentiation blockade is directly linked to oncogenic MYB-dependent gene expression in AML.

Sequestration of CBP/P300 contributes to MYB-dependent leukemogenic gene expression

The direct link between leukemogenic gene expression and differentiation blockade suggests that CRYBMIM not only blocks the assembly of the MYB:CBP/P300 complex, but also induces its remodeling to promote AML differentiation. To test this hypothesis, we analyzed the occupancy of MYB and CBP/P300 genome-wide using chromatin immunoprecipitation followed by sequencing (ChIP-seq). Consistently, we found that CRYBMIM treatment leads to significant redistribution of both MYB and CBP/P300 on chromatin (Figures 6A-D). For example, after one hour of CRYBMIM treatment, both MYB and CBP/P300 are evicted from loci enriched in the MYB-associated DNA-binding motifs (Figures 6A and 6C, lost peaks). By four hours of CRYBMIM treatment, MYB was significantly depleted from 2,587 promoters and enhancers, primarily at sites associated with the MYB DNA-binding motifs, as well as motifs corresponding to

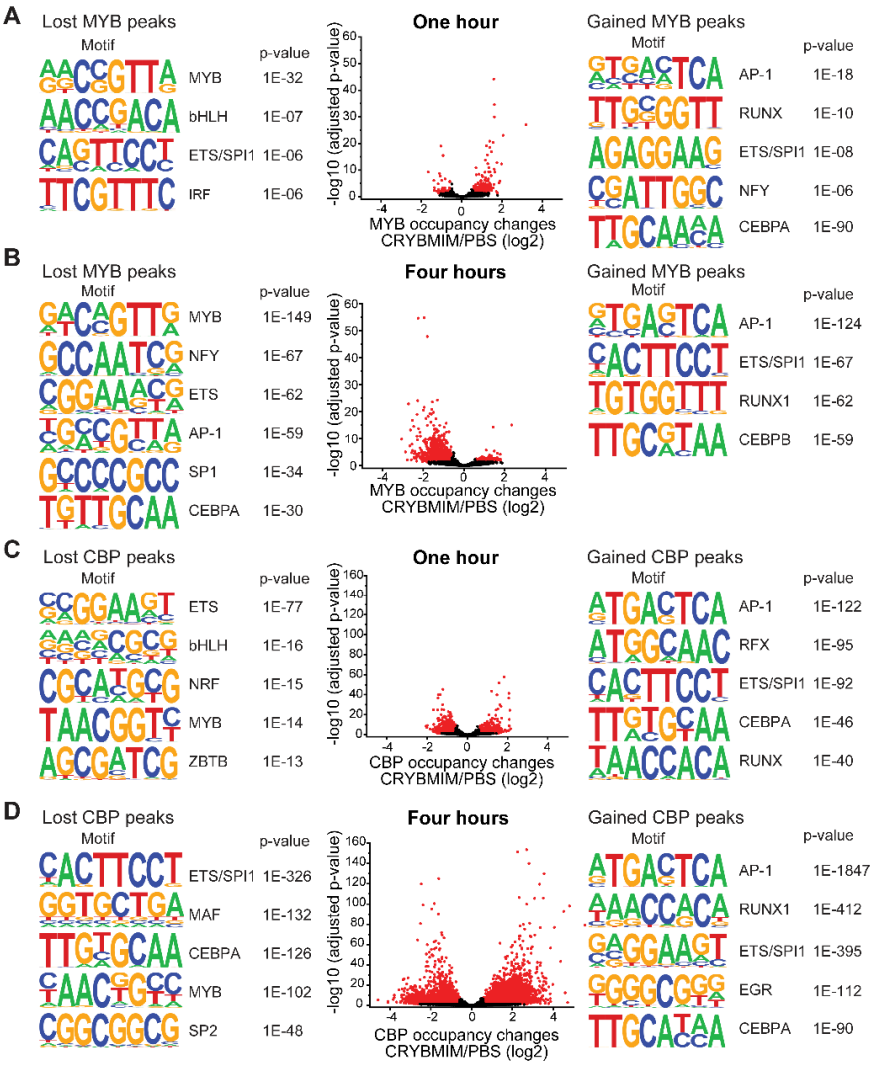

Figure 6. CRYBMIM remodels MYB and CBP/P300 chromatin complexes in AML cells. (A-B) Volcano plots of relative MYB chromatin occupancy in MV411 cells changes after one hour (A) and four hours (B) of 20 μM CRYBMIM treatment compared to PBS control, as analyzed by ChIP-seq. Sequence motifs found in CRYBMIM-induced MYB-depleted (left) and MYB-enriched loci (right) are shown. p-values denote statistical significance of 3 technical replicates. **(C-D)** Volcano plots of CBP/P300 chromatin occupancy changes after one hour (C) and four hours (D) of 20 μM CRYBMIM treatment as compared to control, as analyzed by ChIP-seq. Sequence motifs found in CRYBMIM-induced CBP/P300-depleted (left) and CBP/P300-enriched loci (right) are shown. p-values denote statistical significance of 3 technical replicates.

NFY, ETS family, AP-1 family, SP1, and C/EBP family member transcription factors (Figures 6B and 6D). Noticeably, CBP/P300 was not only depleted from 7,579 genes, but also significantly redistributed to 11,324 new loci (Figure 6D), consistent with the remodeling of its complex upon CRYBMIM treatment. Loci depleted of CBP/P300 were significantly enriched in MYB-associated DNA-binding motifs, as well as those corresponding to the SPI1/ETS, MAF, C/EBP family member, and SP2 transcription factors (Figure 6D). Likewise, loci that gained CBP/P300 upon CRYBMIM treatment were enriched in DNA-binding motifs for the AP-1, RUNX1, EGR, and C/EBP family member transcription factors (Figure 6D). In all, peptidomimetic blockade of MYB:CBP/P300 assembly causes remodeling of transcription factor complexes at loci controlling leukemic gene expression, associated with genome-wide redistribution of CBP/P300 transcriptional co-activation complexes. Thus, sequestration of CBP/P300 from genes controlling hematopoietic differentiation contributes to the leukemogenic MYB-dependent gene expression.

MYB assembles aberrant transcription factor complexes in AML cells

Dynamic redistribution of CBP/P300 transcription factor complexes associated with distinct transcription factor activities upon blockade of MYB:CBP/P300 binding suggests that MYB organizes an aberrant transcriptional co-activator complex in AML cells. To define this complex, we used specific antibodies to immunoprecipitate MYB from non-denatured nuclear extracts of MV411 AML cells, and identify co-purifying proteins using high-accuracy quantitative mass spectrometry. To control for abundant proteins and other contaminants that may co-purify non-specifically, we used non-specific isotype control antibodies and precursor ion quantitation to establish stringent statistical parameters that led to the identification of 724 unique proteins that are specifically associated with MYB in MV411 AML cells (Figure 7A). This included CBP itself, as confirmed by the high-confidence identification of unique peptide spectra that distinguish CBP from P300, with four additional peptides

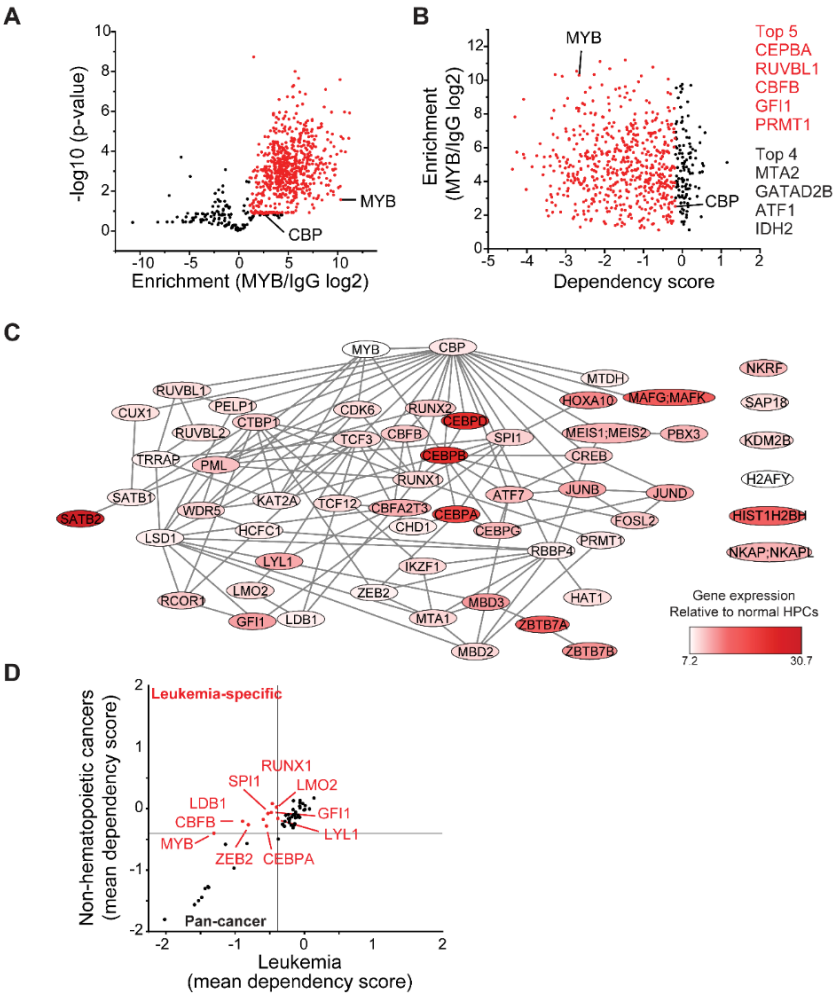

Figure 7. MYB assembles aberrant nuclear transcription factor complexes in AML cells. (A) Volcano plot of nuclear MYB-associated proteins compared to IgG control, as analyzed by affinity purification-mass spectrometry of MV411 cells. Red symbols denote specifically MYB-associated proteins, as defined by association with CBP (MYB/IgG log2>1). p-values denote statistical significance of 3 biological replicates. **(B)** Enrichment of MYB-associated proteins (red) as a function of their corresponding CRISPR DepMap dependency scores in MV411 cells. Red symbols denote functionally required proteins, as defined by the genetic dependency of CBP (score<-0.18). **(C)** Network of BioGRID protein interactions for MYB-associated nuclear AML proteins as a function of their respective hematopoietic expression aberrancy scores, based on their relative gene expression in AML cells as compared to normal bone human bone marrow progenitor cells (white to red color gradient indicates increasingly aberrant gene expression). **(D)** Comparison of the genetic dependency scores in leukemia cell lines as compared to all other non-hematopoietic cancer cell lines for MYB-associated nuclear AML proteins, with red symbols denoting proteins that are required in leukemia as compared to non-hematopoietic cancers.

shared by both CBP and P300 (Figure 7-figure supplement 1), as well as other known MYB interactors such as CEBPB (Supplementary File 3a).

Because MYB is required for the growth and survival of diverse AML subtypes, we reasoned that its essential non-redundant co-factors can be identified from the analysis of their functional dependencies, as assessed by genetic CRISPR interference (Tsherniak et al., 2017). We assigned the CRISPR dependency score of CBP itself in MV411 cells as the threshold to identify functionally non-redundant MYB:CBP co-factors (Figure 7B). We found that these genes encode factors with diverse molecular functions, including a group of 59 chromatin-associated proteins (Supplementary File 3b). By using currently annotated protein-protein interactions (Oughtred et al., 2019), we constructed their interaction network, based on interactions detected by affinity purifications coupled with either Western immunoblotting or mass spectrometry (Figure 7C). Analysis of their expression in normal human hematopoietic progenitor as compared to AML cells (Cancer Genome Atlas Research Network et al., 2013), led to the identification of candidate co-factors with apparently aberrant expression in AML cells (Figure 7C, dark red). Indeed, 10 such factors were selectively required for 37 leukemia but not 615 other non-hematopoietic cancer cells lines (Figure 7D). The physical association of MYB, CBFB, ZEB2, C/EBP family members, LYL1, SPI1, RUNX1, LMO2, and GFI1 and their non-redundant functional dependencies in AML cells (Figures 7A-D) are in agreement with the chromatin dynamics involving distinct MYB, C/EBP family members, LYL1, SPI1, and RUNX1 DNA-binding motifs observed in CRYBMIM-treated cells (Figure 6A-B), associated with the apparent redistribution and remodeling of their CBP/P300 co-activator complexes (Figure 6C-D). Indeed, these factors directly associate with the MYB regulatory complex, and their DNA binding motifs are enriched at loci affected by CRYBMIM treatment (Figure 6).

To define the composition of the MYB transcription factor complex across biologically and genetically distinct subtypes of AML, we used co-immunoprecipitation to measure the physical association of MYB and its cofactors in a panel of AML cell lines, spanning representative cell types with relatively high (MV411, HL60, OCIAML2, OCIAML3) and low (U937, Kasumi-1, K562) susceptibility to CRYBMIM (Figure 8). We found that in all seven cell lines tested, MYB was physically associated with LYL1 and E2A transcription factors (Figure 8A). In contrast, LMO2 was physically associated with MYB in all cell lines except OCIAML2, CEBPA was co-assembled with MYB in OCIAML2 and U937 cells, and SATB1 was co-assembled with MYB in MV411 and HL60 cells (Figure 8A). These findings are all in complete agreement with the chromatin dynamics of MYB, as observed using ChIP-seq (Figure 6). In addition, we corroborated these findings by examining the association of specific transcription factors with CBP/P300 (Figure 8B). The only exception is SPI1/PU.1, which does not appear to be physically associated with MYB or CBP/P300 in examined cell lines, suggesting that the apparent SPI1/PU.1 sequence motifs observed in MYB-associated loci are due to other ETS family factors (Figure 6). In all, MYB assembles a convergently organized transcription factor complex in genetically diverse AML cells.

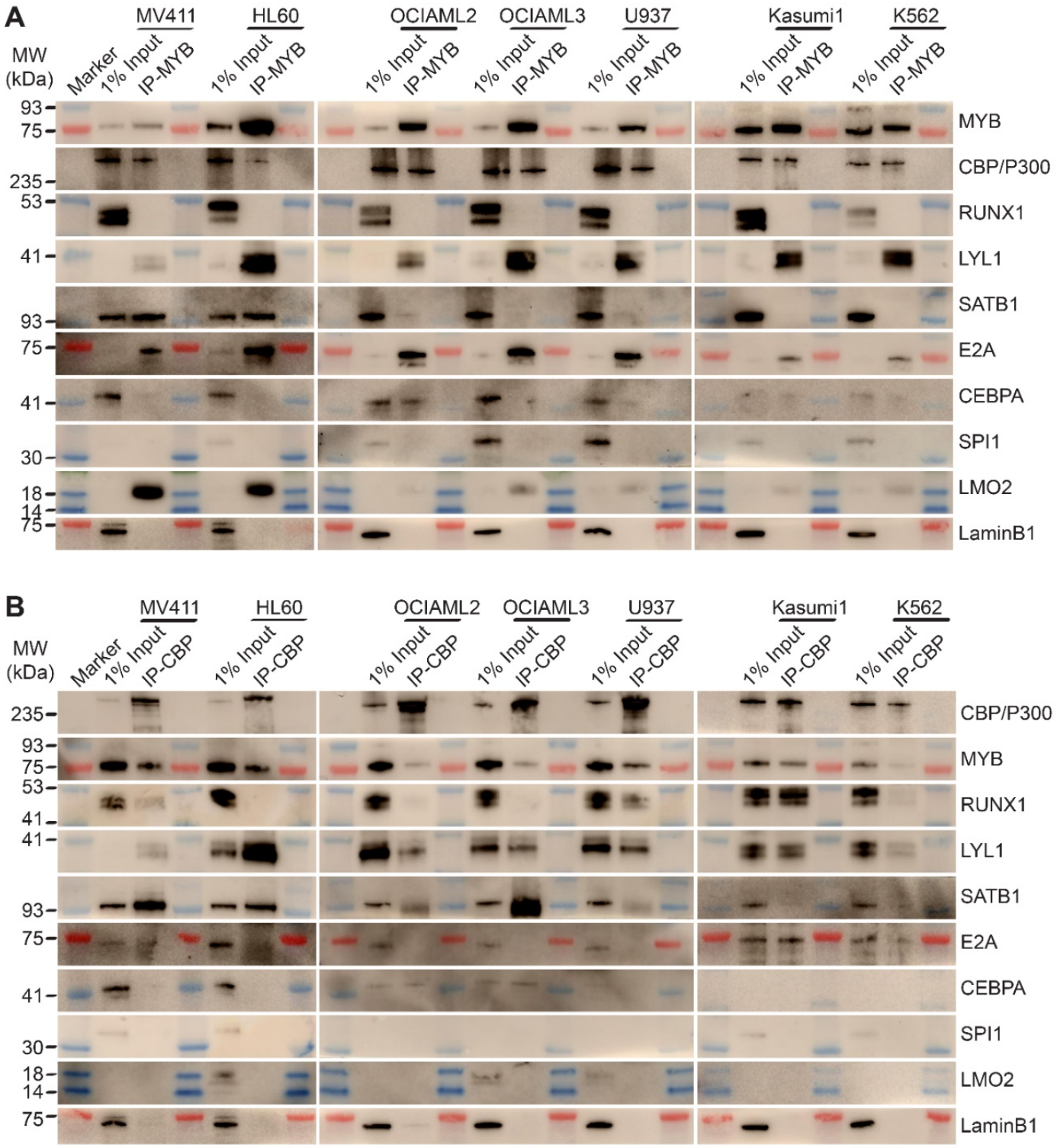

Figure 8. MYB and CBP/P300 assemble convergently organized nuclear transcription factor complexes in genetically diverse AML cells. (A-B) Western blots of specific transcription factors in immunoprecipitated MYB (A) and CBP/P300 (B) nuclear complexes in seven genetically diverse AML cell lines, as indicated. Blue and red bands indicate molecular weight markers. LaminB1 serves as the loading control.

MYB transcription complexes are associated with aberrant cofactor expression and assembly in AML cells

Insofar as various forms of AML exhibit blockade of normal hematopoietic differentiation induced by distinct leukemia oncogenes, and at least some of the MYB-assembled cofactors have reduced gene expression in normal CD34+ hematopoietic progenitor cells (Figure 7C), we reasoned that their assembly in leukemia cells may be due to their aberrant co-expression. To test this, we measured their protein expression in human AML cells using quantitative fluorescent immunoblotting, as compared to normal human CD34+ umbilical cord blood progenitor, adult peripheral blood B- and T-lymphocytes, and monocytes (Figure 9A). We found that most transcription factors that are assembled with MYB in diverse AML cell lines could be detected in one or more normal human blood cells, albeit with variable abundance, with the exception of CEBPA and SATB1 that were measurably expressed exclusively in AML cells (Figure 9A).

To determine whether specific combinations of MYB-assembled transcription factors are associated with the leukemic activity of the MYB complex, we clustered the protein abundance values of distinct groups of transcription factors using principal component analysis (Figure 9B-D). We found that this approach exhibited excellent separation between CRYBMIM-sensitive (MV411, OCIAML2, OCIAML3, HL60) and less sensitive (Kasumi1, K562) cell lines, with the first (PC1, 62%) and second (PC2, 19%) eigenvectors explaining more than 80% of the variability in CRYBMIM susceptibility (Figure 9B). In particular, the protein abundance levels of CEBPA and LYL1 exhibited the greatest contribution to the observed clustering (Figure 9C), consistent with their observed activity in MYB-assembled chromatin dynamics (Figure 6).

In addition to aberrant co-expression of various MYB-assembled cofactors, their aberrant assembly in leukemia cells may also contribute to their oncogenic functions. To test this hypothesis, we purified MYB complexes from normal human cord blood progenitor cells using immunoprecipitation, and determined the abundance of specific cofactors as compared to human AML cells using Western immunoblotting (Figure 9E). While MYB, CBP/P300 and LYL1 were physically associated in normal umbilical cord blood mononuclear cells, we did not observe their physical association with E2A, SATB1 and LMO2. In contrast, MYB and CBP/P300 complexes were highly enriched in LYL1, SATB1, E2A, and LMO2 in MV411 and HL60 AML cells (Figure 9E). Thus, oncogenic MYB transcription factor complexes are aberrantly organized in AML cells, associated at least in part with inappropriate transcription factor expression.

If convergent assembly of MYB with common transcription factors in biologically diverse subtypes of AML is responsible for the induction of oncogenic gene expression and blockade of normal hematopoietic differentiation, then pharmacologic blockade of this process would suppress shared gene expression programs associated with AML growth and survival, and promote gene expression programs associated with hematopoietic differentiation. To test this prediction, we carried out comparative gene expression analyses using RNA-sequencing of CRYBMIM effects in *AML1-ETO*-translocated Kasumi1, *DNMTA3A;NPM1*-mutant OCIAML3, *MLL*-rearranged MV411, *NRAS*-mutant;*MYC*-amplified HL60, and *CALM10*-rearranged U937 AML cell lines (Figure 5A-B and Figure 9-figure supplement 1). Unsupervised clustering of differentially expressed genes exhibited excellent separation between CRYBMIM- and PBS-treated cells. In agreement with the prediction, we observed a shared set of genes that was suppressed in expression upon CRYBMIM treatment of all AML cell lines, such as *MYC* for example (Figure 5A and Figure 9-figure supplement 1A-B). Similarly, we observed a shared set of genes that was induced by CRYBMIM treatment, including numerous genes associated with hematopoietic differentiation such as *FOS*, *JUN*, and *ATF3,* as well as *SERPINE, KLF6*, *DDIT3* and *NFKBIZ* (Figure 5A-B and Figure 9-figure supplement 1B). Thus, oncogenic gene expression in biologically diverse subtypes of AML involves convergent and aberrant assembly of MYB transcription factor complexes that induce genes that promote leukemogenesis and repress genes that control cellular differentiation.

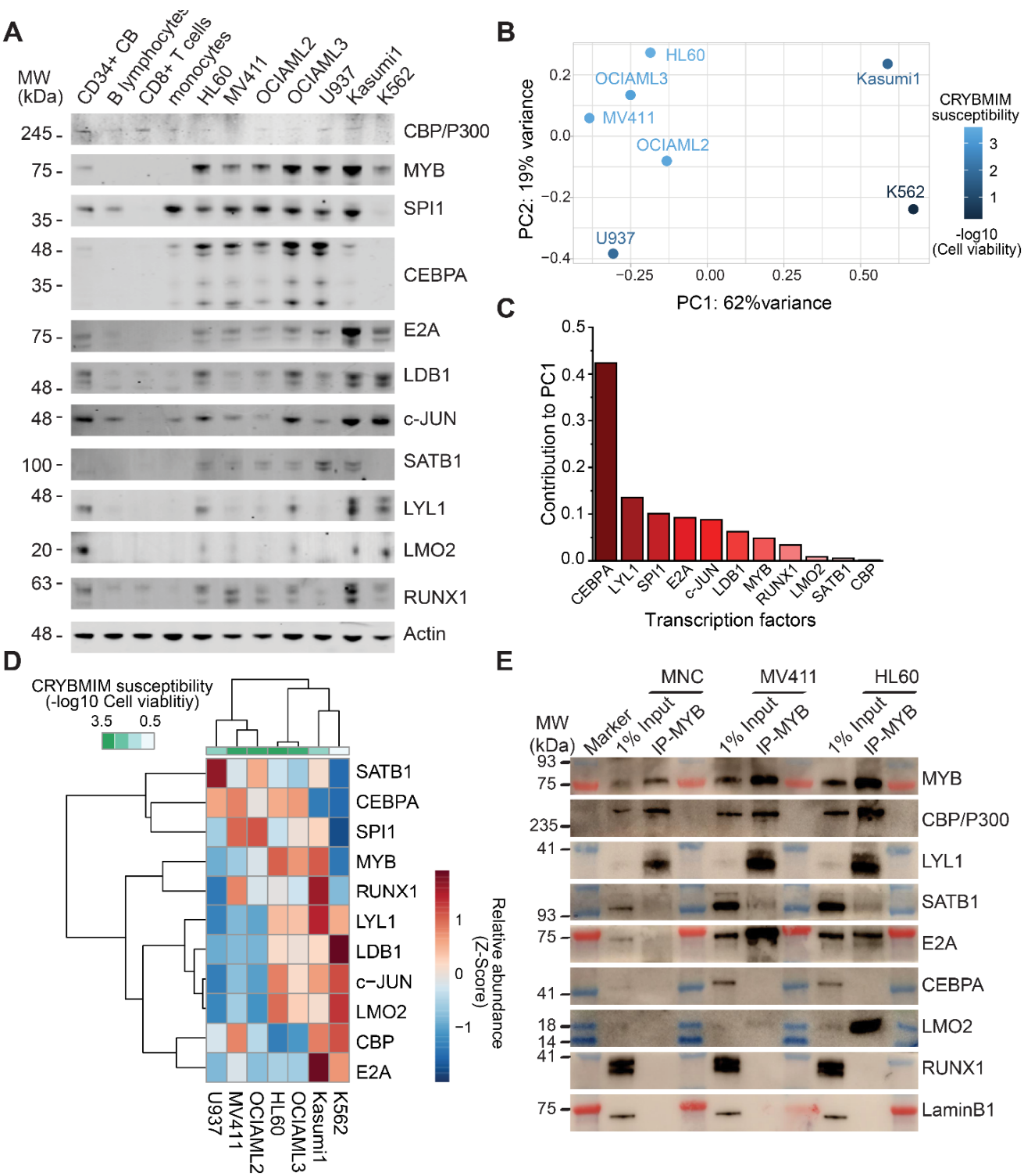

Figure 9. Specific MYB complex factors are aberrantly expressed and assembled in AML as compared to normal human blood cells. (A) Western blots of specific MYB complex transcription factors in normal human blood cells and genetically diverse leukemia cells, as indicated. Actin serves as the loading control. **(B)** Principal component analysis of MYB complex transcription factor abundance, as quantified by image densitometry, as a function of susceptibility of various AML cell lines to CRYBMIM (blue color index). **(C)** Contribution of individual MYB complex transcription factor abundance to the top PCA eigenvector. **(D)** Heatmap of hierarchical clustering of MYB complex individual transcription factor abundance and CRYBMIM susceptibility. **(E)** Western blots of specific transcription factors in specific MYB nuclear complexes immunoprecipitated from normal human umbilical cord mononuclear cells (MNC), as compared to MV411 and HL60 AML cells. Blue and red bands indicate molecular weight markers. LaminB1 serves as loading control.

Aberrant organization of the MYB transcription factor complex is regulated by proteolysis

We noted that MYB:CBP/P300 binding in AML cells was reduced by several orders of magnitude upon CRYBMIM treatment (Figure 6). This contrasts to the nearly equal binding affinities of CRYBMIM and native MYB to CBP/P300 KIX domain (Figure 2D), suggesting that cellular processes must contribute to the biologic effects of CRYBMIM. Thus, we examined cellular MYB protein levels using quantitative immunoblotting (Figures 10A, Figure 10-figure supplement 1). We found that CRYBMIM treatment induced nearly 10-fold reductions in cellular MYB protein levels with exponential kinetics on the time-scale of 1-4 hours in CRYBMIM-sensitive MV411, HL60, OCIAML2, and OCIAML3 cells. In contrast, CRYBMIM treatment induced less pronounced depletion of MYB in U937, Kasumi1 and K562 cells that are less sensitive to CRYBMIM. Susceptibility of diverse AML cell lines to CRYBMIM, as measured by cell viability (Figure 3G), was significantly correlated with the apparent kinetics of MYB protein decay (Pearson r = 0.94; Figure 10B).

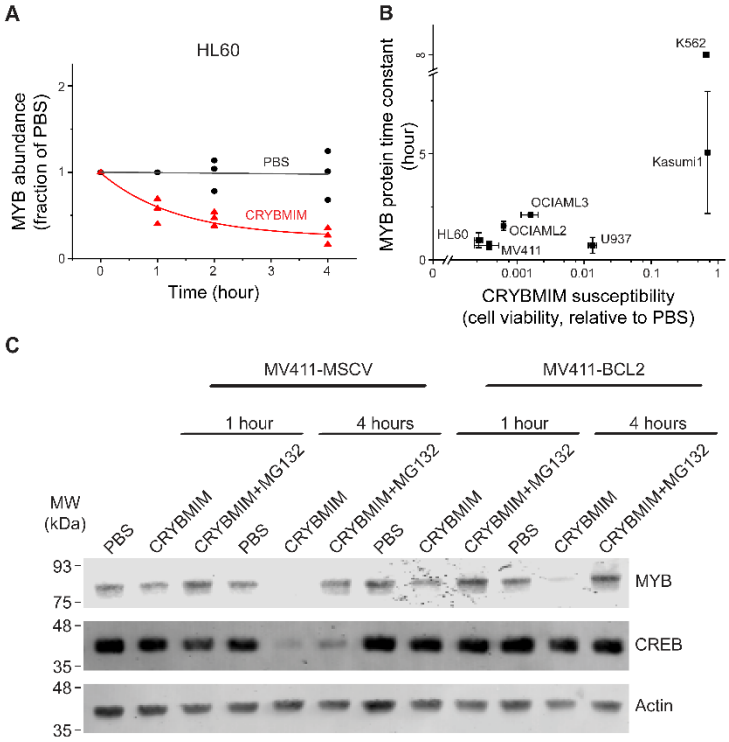

Figure 10. Peptidomimetic remodeling of MYB transcriptional complexes leads to rapid MYB proteolysis. (A) Quantification of MYB abundance in HL60 cells as a function of duration of 20 μM CRYBMIM treatment (red) as compared to PBS control (black) using Western blot image densitometry. Lines represent single exponential decay fits. Western blots and fits for all cell lines studied are shown in Supplementary Figure 8. Symbols represent biological triplicates. **(B)** MYB protein half-life, as estimated by exponential decay kinetics, in genetically diverse AML cell lines as a function of CRYBMIM susceptibility (Pearson r = 0.94, excluding resistant K562). Horizontal bars represent standard deviation of CRYBMIM susceptibility. Vertical bars represent standard deviation of time constants. **(C)** Western blots of MYB and CREB in MV411 AML cells transduced with MSCV retroviruses encoding GFP control (MV411-MSCV) or BCL2 (MV411-BCL2), treated with 20 μM CRYBMIM or PBS control with or without 10 μM of MG132 for one or four hours, as indicated. Actin serves as loading control.

Rapid reduction of MYB protein levels by CRYBMIM is consistent with proteolysis. To investigate this directly, we quantified CRYBMIM-induced reduction of MYB protein levels in MV411 cells upon co-treatment with the proteosomal/protease inhibitor MG132 (Figure 10C). Consistent with the proteolytic depletion of MYB upon CRYBMIM treatment, MG132 co-treatment led to near complete rescue of this effect (Figure 10C). This effect was specific because overexpression of *BCL2*, which blocks MYBMIM-induced apoptosis (Ramaswamy et al., 2018), and rescued the depletion of cellular CREB, presumably due to non-specific proteolysis that accompanies apoptosis, was unable to rescue CRYBMIM-induced proteolysis of MYB (Figure 10C). Since CBP is required for the anti-leukemic effects of CRYBMIM, we queried whether MYB protein levels are affected by CBP depletion. We observed no measurable differences in MYB protein levels between wild-type, CBP-deficient or control *AAVS1*-CRISPR targeted MV-411 cells (Figure 10-figure supplement 1C). This suggests that either P300 can compensate for CBP-mediated functions, and/or MYB proteolysis is not regulated solely by its interaction with CBP/P300, but requires specific activities of CBP/P300 induced by CRYBMIM. In all, MYB transcription complexes are regulated by specific factor proteolysis in AML cells, and can be induced by its peptidomimetic blockade.

Release and redistribution of MYB-sequestered transcription factors restores normal myeloid differentiation

We reasoned that the remodeling of MYB regulatory complexes and their associated chromatin factors such as CBP/P300 are responsible for the anti-leukemia effects of CRYBMIM, at least in part via reactivation of cellular differentiation of MV411 AML cells (Figure 5). To test this, we prioritized CEBPA, LYL1, SPI1, and RUNX1 as MYB-associated co-factors based on their physical interactions and functional dependencies in AML cells (Figure 7), and analyzed their chromatin dynamics in response to CRYBMIM treatment using ChIP-seq analysis. Consistent with the release and redistribution mechanism, we observed both coherent and factor-specific dynamics of MYB co-factors on chromatin upon CRYBMIM treatment (Figure 11A). Clustering of observed dynamics revealed nine classes of apparent chromatin responses (Figure 11B). Approximately one third of the affected genes lost both MYB and CBP/P300 in response to CRYBMIM, as well as RUNX1, LYL1, and/or CEBPA (Figure 11B; yellow clusters 1, 3, and 6). Genes in the MYB and CBP/P300-depleted clusters 1, 3, and 6 were enriched in those associated with the development of hematopoietic progenitor cells, as well as MYC and HOXA9/MEIS1 targets (Supplementary File 3c), consistent with current and past gene expression profiling studies (Figure 5 and Figure 9-figure supplement 1). In addition, these genes were enriched in pathways involving chromatin repression,
consistent with the enrichment of DNA-binding sequence motifs of transcriptional repressors YY1 and REST/NRSF (Figure 11B). This suggests a potential mechanism for the long-hypothesized repressive functions of MYB. While we found no apparent changes in JUN occupancy, motif analysis at loci that both lost and gained MYB and CBP/P300 revealed enrichment of AP-1 sequence elements, consistent with the presence of other AP-1 family member(s) in MYB regulatory complexes. Minor apparent contribution of MYB:CBP/P300-independent chromatin dynamics involved genes enriched in MLL targets (Figure 11B, Supplementary File 3c; blue clusters 5, 8), consistent with the activity of MLL fusion proteins in MV411 cells.

Notably, the two chromatin dynamics clusters 4 and 9 that gained both MYB and CBP/P300 in response to CRYBMIM, associated with the accumulation of CEBPA, RUNX1, and/or CREB, were enriched in genes controlling myeloid differentiation programs (Figure 11B; orange, and Supplementary File 3c). This is consistent with the CRYBMIM-induced gene expression differentiation programs and accompanying morphologic features of myeloid differentiation (Figure 5). While CRYBMIM induces MYB proteolysis, residual MYB can remain bound to chromatin, as evident by its accumulation in specific loci upon CRYBMIM treatment. MYB-binding loci lost upon CRYBMIM treatment showed significant enrichment for known MYB binding motifs, while CRYBMIM-induced MYB peaks did not (p = 1e-149 vs 1e-3, 56 % vs 5.7 % of target sites, respectively). This raises the possibility that DNA binding affinity of MYB could be regulated by CBP/P300, either by direct effects such as MYB deacetylation upon CRYBMIM treatment, or indirectly via binding with other transcription factors. It is possible that other transcription factors may contribute to oncogenic gene expression in AML cells, such as CREB for example, as evident from their contribution to MYB-independent chromatin dynamics (Figure 11B; pink cluster 2). However, this is likely a minor effect, given the relatively modest reprogramming of gene expression by CREBMIM that targets the CREB:CBP/P300 complexes in AML cells (Figure 5 and Figure 5-figure supplement 1).

Globally, the most pronounced feature of MYB complex remodeling is the release of CBP/P300 from genes that are associated with AML cell growth and survival to those that are associated with hematopoietic differentiation. To examine this, we compared relative gene expression as a function of the relative occupancy of CBP/P300 and MYB upon 4 hours of CRYBMIM treatment (Figure 11-figure supplement 1A-B). In contrast to the model in which blockade of MYB:CBP/P300 induces loss of gene expression and loss of transcription factor and CBP/P300 chromatin occupancy, we also observed a large number of genes with increased expression and gain of CBP/P300 occupancy (Figure 11-figure supplement 1A-B). This includes numerous genes that control hematopoietic differentiation, such as *FOS*, *JUN*, and *ATF3*. In the case of *FOS*, we observed that CRYBMIM-induced accumulation of CBP/P300 was associated

with increased binding of RUNX1, and eviction of CEBPA and LYL1 (Figure 11-figure supplement 1C).

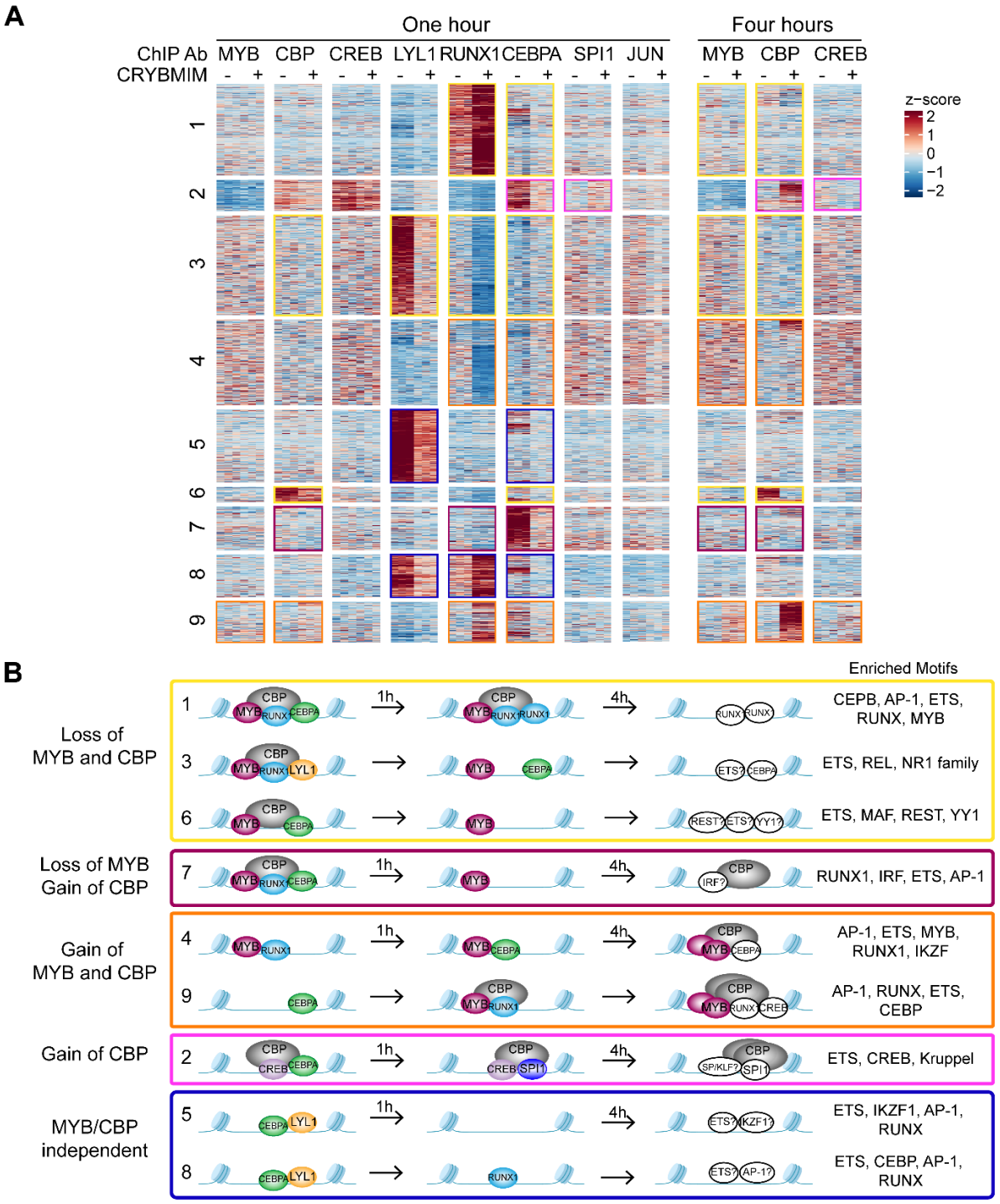

Figure 11. Chromatin dynamics of CRYBMIM remodeled MYB transcription factor complexes in AML cells. (A) Heatmap of transcription factor chromatin occupancy in MV411 cells as a function of time of control PBS or CRYBMIM treatment. Nine clusters identified using k-means clustering are marked by yellow (loss of MYB and CBP), purple (loss of CBP and gain of MYB), orange (gain of MYB and CBP), pink (gain of CBP), and blue (no apparent changes of MYB and CBP) boxes, based on the similarity of their z-scores, with red and blue representing enrichment or depletion of factors, respectively. **(B)** Groups of clusters comprising similar responses to CRYBMIM treatment based on MYB and CBP/P300 dynamics. Sequence motifs enriched at specific loci for each cluster are listed. Factors in white denote factors presumed to be enriched based on sequence motif enrichment.

To confirm directly that peptidomimetic blockade of MYB:CBP/P300 releases CBP/P300 and promotes its association with alternative transcription factors, we specifically immunoprecipitated MYB and CBP/P300 from MV411 AML cells using respective antibodies, and determined their composition by Western immunoblotting (Figure 12A-B). In agreement with biochemical studies, we observed substantial depletion of CBP/P300 from immunoprecipitated MYB complexes upon CRYBMIM treatment (Figure 12A), and of MYB from immunoprecipitated CBP/300 complexes (Figure 12B). Similarly, we observed reduced binding of LYL1, SATB1, E2A, LMO2, and CEBPA. In contrast, whereas no detectable RUNX1 was found co-associated with MYB either at baseline or upon CRYBMIM treatment (Figure 12A), assembly of RUNX1 with CBP/P300 was increased by more than 4-fold upon CRYBMIM treatment, as measured by image densitometry (p = 3.4e-4; Figure 12B-C).

In all, these results support the model in which the core regulatory circuitry of AML cells is organized aberrantly by MYB and its associated co-factors including LYL1, C/EBP family members, E2A, SATB1 and LMO2, which co-operate in the induction and maintenance of oncogenic gene expression, as presumably co-opted by distinct oncogenes in biologically diverse subtypes of AML (Figure 13). This involves apparent sequestration of CBP/P300 from genes controlling myeloid cell differentiation. Thus, oncogenic gene expression is associated with the assembly of aberrantly organized MYB transcriptional co-activator complexes, and their dynamic remodeling by selective blockade of protein interactions can be leveraged therapeutically to induce AML cell differentiation and apoptosis.

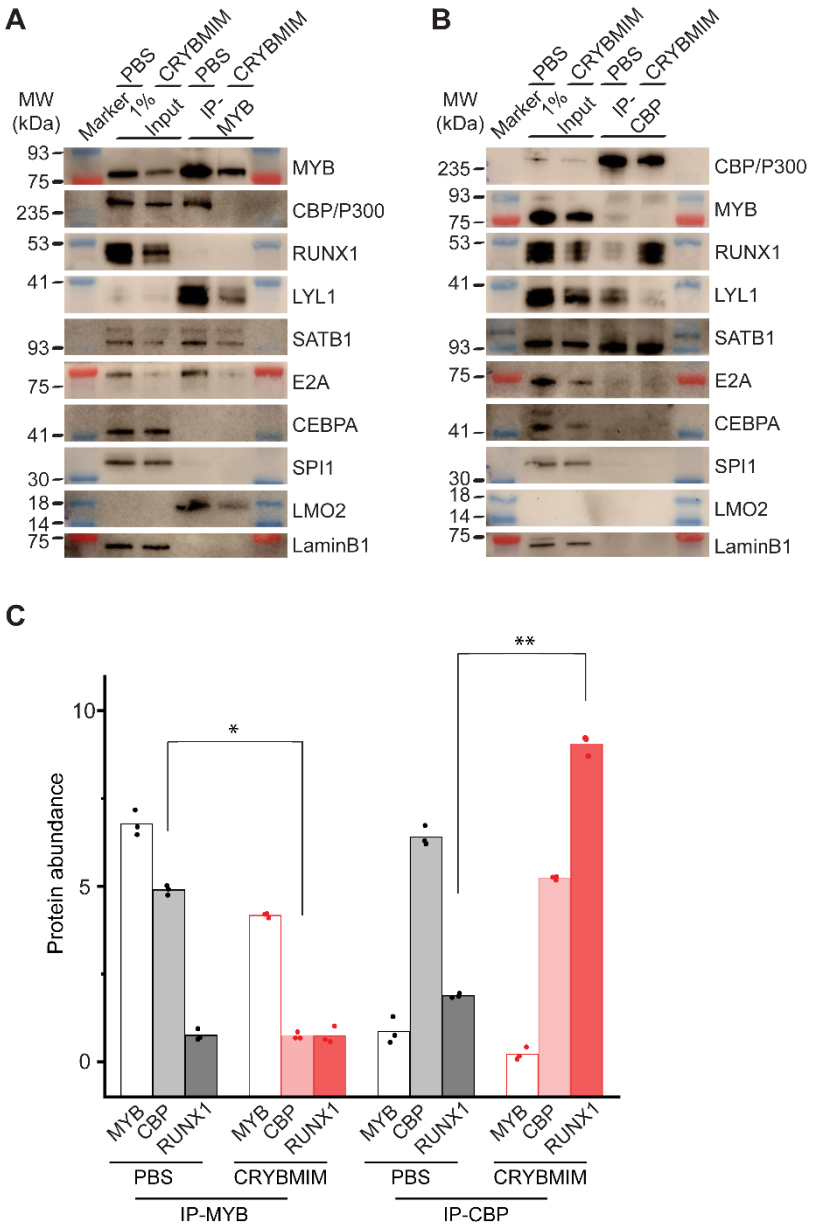

Figure 12. Peptidomimetic blockade of MYB:CBP/P300 by CRYBMIM releases CBP/P300 that recruits RUNX1 to chromatin. (A-B) Western blots of specific transcription factors in nuclear complexes with immunoprecipitated MYB (A) and CBP/P300 (B) in MV411 cells upon treatment with 10 μM CRYBMIM or PBS control for one hour. Blue and red bands indicate molecular weight markers. LaminB1 serves as loading control. **(C)** Abundance of MYB, CBP/P300 and RUNX1, as measured by Western blot image densitometry, in immunoprecipitated MYB and CBP/300 nuclear complexes in MV411 cells treated with CRYBMIM or PBS control. Symbols represent biological triplicates; *p = 4.7e-6, t-test for CBP in MYB complex upon CRYBMIM treatment, **p = 3.4e-6, t-test for RUNX1 in CBP/P300 complex CRYBMIM treatment.

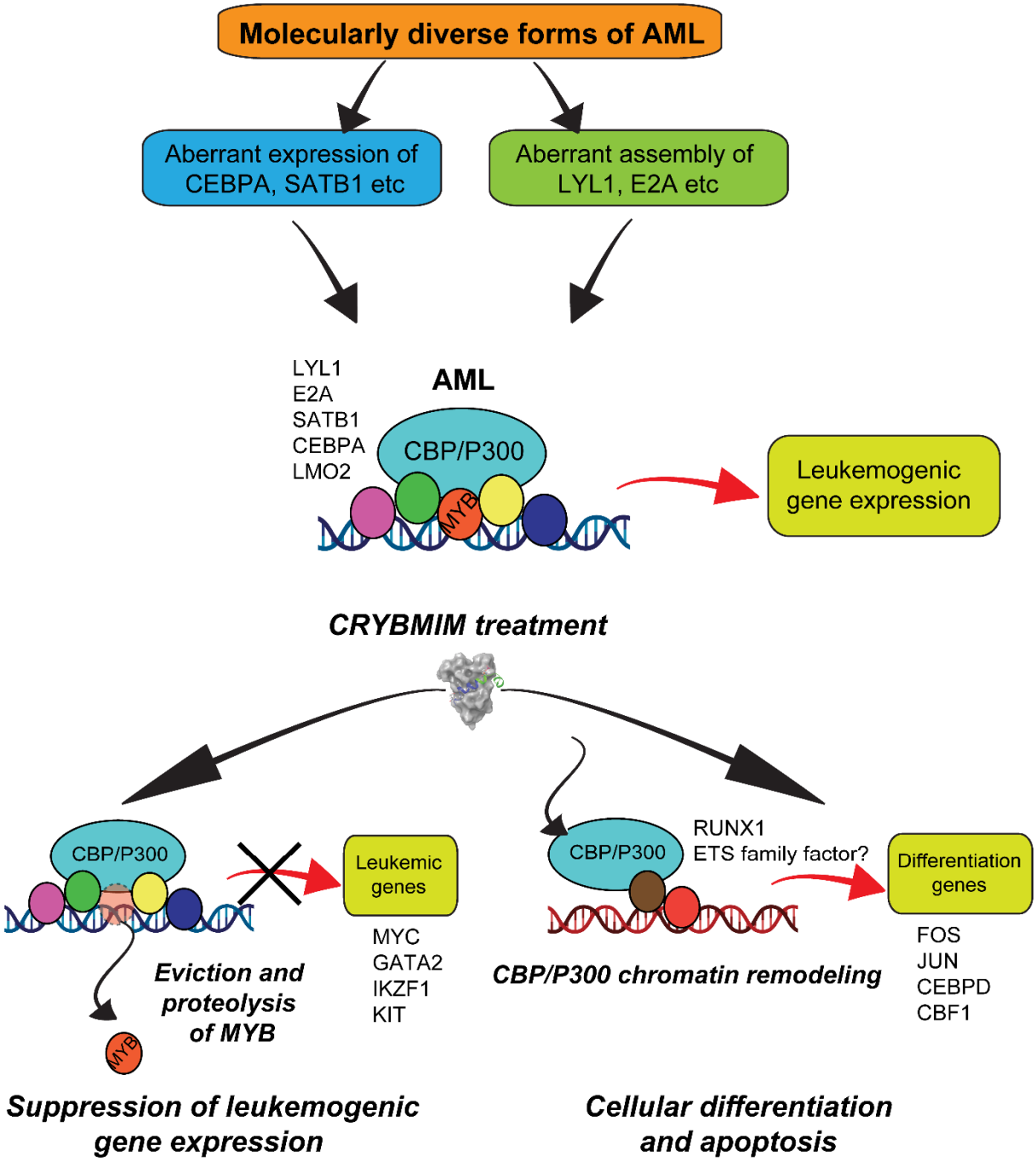

Figure 13. Convergent organization of aberrant MYB complexes controls oncogenic gene expression in acute myeloid leukemia. Schematic of the molecular organization of MYB transcription factor complexes, induced convergently in genetically diverse subtypes of AML, leading to oncogenic gene expression that requires MYB:CBP/P300 interaction and causes susceptibility to its peptidomimetic remodeling, leading to MYB chromatin eviction and proteolysis, and CBP/P300 release to induce cellular differentiation and apoptosis.

DISCUSSION

Dysregulated gene expression is a near universal feature of all human cancers. This is particularly relevant for leukemias which are frequently caused by mutations of genes encoding transcription and chromatin remodeling factors. Among all types of leukemias examined to date, the transcription factor MYB ranks as the most selectively required functional genetic dependency. This nominates MYB both as a compelling therapeutic target, and a focus of mechanistic studies to define fundamental mechanisms of dysregulated gene expression in leukemias.

By rapid and selective peptidomimetic interference with the binding of CBP/P300 to MYB, but not CREB or MLL, we find that the leukemic functions of MYB are mediated by CBP/P300-mediated co-activation of a distinct set of transcriptional factor complexes that are aberrantly assembled with MYB in AML cells. The second-generation, cell-penetrant peptidomimetic MYB inhibitor, termed CRYBMIM, has potent and broad-spectrum activity against diverse subtypes of AML, while relatively sparing normal hematopoietic progenitor cells. Consequently, its improved activity enables high-resolution, genome-wide studies of chromatin and gene expression dynamics that control MYB-dependent leukemic expression in AML cells. We find that CRYBMIM blocks oncogenic MYB gene expression and restores myeloid cell differentiation. This effect involves aberrantly organized MYB regulatory complexes, stably composed of additional transcription factors including LYL1, C/EBP family members, E2A, LMO2 and SATB1, that are reminiscent of core regulatory circuits observed in MYB-dependent T-cell lymphoblastic leukemias and other cancers (Mansour et al., 2014; Sanda et al., 2012). Unexpectedly, we find that MYB-dependent leukemogenic gene expression also involves apparent sequestration of CBP/P300. In turn, peptidomimetic MYB:CBP/P300 blockade releases and redistributes CBP/P300 and other sequestered transcription factors to induce cell differentiation. In all, these findings establish a compelling strategy for pharmacologic reprogramming of oncogenic gene expression that supports its targeting for leukemias and other human cancers caused by dysregulated gene control.

What is the origin of aberrant MYB transcriptional complexes and functions in leukemia cells? MYB is not known to be mutated in most cases of AML, and this study points to its aberrant assembly as the convergent mechanism by which it is pathogenically dysregulated. Indeed, previous studies have found cell type-specific features of MYB gene activation, suggesting the presence of other factors that influence MYB activity (Lei et al., 2004). Furthermore, MYB alone is not sufficient for leukemic cell transformation, indicating the need for specific co-factors in its leukemogenic activity (Gonda et al., 1989; Hu et al., 1991).

By integrating functional genomics and proteomics, combined with gene expression and chromatin dynamics analyses, we identified a set of factors in complex with MYB that appear to be aberrantly and stably co-assembled, including C/EBP family members, LYL1, E2A, LMO2, and SATB1. Their physical interactions and chromatin co-localization with MYB are associated with oncogenic gene expression and blockade of cell differentiation in AML cells. Interestingly, we found no CRYBMIM-induced remodeling of MYB regulatory complexes independent of CBP/P300, indicating that KIX-dependent interaction between MYB and CBP/P300 is required for most of MYB transcriptional activity in AML cells.

It is possible that somatic mutations of regulatory DNA elements, such as those physically associated with MYB regulatory complexes, contribute to the aberrant assembly of these complexes on chromatin, as observed for the oncogenic *TAL1* enhancer mutations in cases of T-ALL (Mansour et al., 2014), and recently suggested for other leukemias (He et al., 2019). It is also possible that leukemic gene expression by MYB involves additional transcriptional co-activators, such as TAF12, as part of the recently described TFIID-SAGA complex interaction (Yali Xu et al., 2018), or other TAFs which have also been implicated in transcriptional co-regulation in leukemias (Jian et al., 2017; Ye Xu et al., 2019). Lastly, it is also possible that distinct subtypes of AML

diverge from the aberrant regulatory complex assembly model presented here. For example, LYL1, an oncogene that is aberrantly expressed in diverse subtypes of AML (Meng et al., 2005), assembles with MYB in leukemia cells examined in our study, similar to its functional homologue TAL1 in cases of T-ALL (Mansour et al., 2014; Sanda et al., 2012). Alternative bHLH transcription factors may cooperate with MYB in some leukemia subtypes, including potential differences in their cells of origin (Jones, 2004). It will be important to determine how aberrant co-expression of such oncogenic regulatory complex co-factors is induced in leukemia cells by diverse oncogenes, such as for example by kinase-dependent dysregulation of transcription factor assembly recently described for MEF2C and LYL1 (Brown et al., 2018; Tarumoto et al., 2018; Vakoc & Kentsis, 2018).

The switch-like response of AML cells to peptidomimetic disassembly of the MYB:CBP/P300 chromatin complex suggests that cellular CBP/P300 exists in a dynamic equilibrium under limiting conditions. Such a model is supported by the Rubinstein-Taybi syndrome due to heterozygous deletion mutations that reduce *CBP* gene dosage, leading to human developmental defects. This model also explains the distinct requirements of CBP and P300 in normal hematopoiesis and leukemia cell development (G. Cheng et al., 2017; Wang et al., 2011), as also observed in our studies in genetically diverse AML cell types, as well as the functional requirement for P300 in CBP-deficient cancers (Ogiwara et al., 2016). Definition of the mechanisms of this molecular switch regulating discrete gene expression programs is expected to reveal distinct mechanisms of dysregulated gene control in AML and other transcription-dysregulated cancers.

Current small molecule inhibitors of MYB lack sufficient selectivity (D R Pattabiraman & Gonda, 2013; Uttarkar et al., 2015, 2016). Our peptidomimetic strategy suggests that structure-based design of effective pharmacologic MYB inhibitors is not only possible, but also desirable given its favorable therapeutic index. First, the functional requirement for peptidomimetic blockade of MYB but not CREB or MLL1 binding in supporting oncogenic gene expression and cell survival suggests that ligands to these permissive binding sites may be used to gain binding affinity of pharmacologic MYB inhibitors. Indeed, such a fragment-based design strategy was successfully used to develop effective BH3 mimetics, including venetoclax that has recently been approved for leukemia therapy.

Quantitative improvement in binding affinity from MYBMIM to CRYBMIM is associated with qualitative improvement in biological potency, due to the combination of enhanced MYB:CBP/P300 binding competition and proteolytic remodeling of its complex. Such event-driven pharmacology has recently been used to develop a variety of pharmacologic modulators of protein interactions, such as PROTACs. The dual mechanism of action observed for peptidomimetic MYB:CBP/P300 inhibitors, involving suppression of oncogenic MYB activity and remodeling of CBP/P300, provides a pharmacologic strategy for both precise chemical probes and improved therapeutics. Indeed, ligation of the KIX domain of CBP/P300 by CRYBMIM may allosterically modulate the activity of its complexes, similar to the allosteric regulation of its acetyltransferase activity by auto-acetylation and intramolecular bromodomain binding.

Functional proteomic maps of MYB regulatory complexes provided by our study should be useful in identifying key protein-protein interactions and post-translational enzymatic modifications that are aberrantly induced in AML cells, as targets for improved therapies. For example, this may involve transcription factor acetylation by CBP/P300 (Roe et al., 2015; Wang et al., 2011), warranting the investigation of recently developed selective CBP/P300 acetyltransferase inhibitors, which have shown particular activity in hematopoietic cancers (Lasko et al., 2017).

Finally, recent studies have found that stable non-genetic resistance is a common feature of relapsed AML, and this resistance at least in part is due to the use of alternative enhancers to sustain aberrant gene expression (Bell et al., 2019). Therapeutic remodeling of complexes of master regulators such as MYB may constitute an effective strategy to reprogram oncogenic gene

expression that may prevent or overcome such resistance, providing a platform for therapy of regulatory complex-mediated gene dysregulation in human cancers. Development and investigation of clinical-grade MYB inhibitors, including improved derivatives of MYBMIM and CRYBMIM, are important directions of future work for patients with MYB-dependent acute myeloid and lymphoblastic leukemias, blastic plasmacytoid dendritic cell neoplasms, gliomas, breast, colon and adenoid cystic carcinomas.

METHODS

Reagents

Synthetic peptides were produced by solid phase synthesis, purified by liquid chromatography, and confirmed by mass spectrometry (Tufts University Core Facility). Peptides were dissolved in phosphate buffered saline (PBS) at a concentration of 1 mM, as measured using optical absorbance measurements at 280 nm. Cell culture media was obtained from Corning. All cell lysis buffers were supplemented with protease inhibitors comprised of AEBSF (0.5 mM, Santa Cruz, SC-202041B), bestatin (0.01 mM, Fisher/Alfa Aesar, J61106-MD), leupeptin (0.1 mM, Santa Cruz, SC-295358B), and pepstatin (0.001 mM, Santa Cruz, SC-45036A), and cOmplete, EDTA-free Protease Inhibitor Cocktail (Roche) as required. MG132 was obtained from Cell Signaling Technologies.

Plasmids

MSCV-IRES-GFP retroviral vector encoding human *BCL2* was a gift from Takaomi Sanda (Sanda et al., 2013; Ramaswamy et al., 2018). Plasmids used for genome-wide CRISPR screen and CRISPR competitive assays are described below.

Cell culture

The cell lines MV411, MOLM13, OCIAML2, THP1, NB4, Kasumil1, HEL, OCIAML3, SKM1, U937, HL60, and K562 were obtained from the American Type Culture Collection (ATCC, Manassas, Virginia, USA) or DSMZ (Leibniz Institute, Braunschweig, Germany). The identity of all cell lines was verified by STR analysis (Integrated Genomics Operation Core Facility, MSKCC) and absence of Mycoplasma contamination was determined using Lonza MycoAlert (Lonza Walkersville, Inc., Walkersville, MD, USA). Cell lines were cultured in 5% CO_2 in a humidified atmosphere at 37˚ C and were maintained in RPMI 1640 medium (Corning) supplemented with 10% fetal bovine serum (FBS) (VWR), antibiotics (100 U/ml penicillin and 100 μg/mL streptomycin), and L-glutamine (1%), referred to as complete media. Human umbilical cord blood was obtained from the New York Blood Center. Human B lymphocytes, CD8+ T cells, and monocytes were obtained from Cellero.

Genome-wide CRISPR screen

Cas9-expressing MOLM13 cells were established by transduction with LentiV_Cas9_Blast (Tarumoto et al., 2020), and then the cells were infected with lentivirus of human CRISPR Knockout GeCKOv2 library (Sanjana et al., 2014) with MOI of approximately 0.3 for transduction of single guide RNA per cell. After selection of guide RNA-positive cells by 3 days of puromycin (1 μg/ml) treatment, the cells were divided into three populations, in which guide RNA representation was approximately 500 cells/guide. One of the populations was harvested as T0 sample. The other populations were treated with 10 μM MYBMIM or PBS for 3 days, followed by culture without MYBMIM or PBS for about a week to allow the survived cells to grow, and harvested as T1 sample. Genomic DNA was isolated using phenol/chloroform extraction. Illumina sequencing library was generated by two-step PCR where guide RNA regions were first amplified, followed by the amplification with primers containing sequencing adaptor/barcodes. Barcoded libraries were pooled and analyzed by single-end sequencing using NextSeq 500 (Illumina). MAGeCK tools (W. Li et al., 2014) were used to count guide RNA reads in each sample and to

calculate log fold-change and p-value between T0 and T1 samples to identify the guide RNAs enriched in T1 population. Screens were performed in biologic duplicates.

Molecular modeling

All structures were built using Maestro (Schrodinger). Structures of KIX with MYB, CREB, and MLL peptides were modeled based on PDB IDs 1SBO, 1KDX, and 2LSX, respectively. For CRYBMIM, PDB 1KDX was used as a starting model, replacing CREB amino acids 137-146 with MYB amino acids 298-310. Resulting models were energy minimized using MacroModel (Schrodinger) using the OPLS_2005 force field with implicit water at a dielectric constant of 80.

Protein expression and purification

CBP KIX was purified as described previously (Ramaswamy *et al.*, 2018). Briefly, BL21(DE3) cells (Invitrogen) transformed with pGEX-KIX plasmid were induced at 37° C with isopropyl beta-D-1-thiogalactopyranoside (IPTG) for 3 hours. Cells were harvested by centrifugation at 3000 x g for 15 min. Pellets were resuspended in lysis buffer of 50 mM Tris-HCl pH 7.3, 150 mM NaCl, 0.1% Tween-20, 1 mM DTT, 5 mM EDTA, supplemented with protease inhibitors at a ratio of 50 mL lysis buffer per 1 L of bacterial culture. Cells were lysed for ten minutes on ice (15 sec on, 15 sec off, 40% amplitude) using the Misonix probe sonicator (Qsonica, Newtown, CT). Lysates were cleared by centrifugation for 1 h at 21,800 x g at 4° C. Cleared lysates were incubated with 4 mL glutathione agarose resin slurry (GoldBio) for 1 h at 4° C to capture GST-KIX. Resin was washed four times with 50 mM Tris-HCl pH 7.4, 150 mM NaCl. KIX domain was cleaved from GST by incubation of resin-bound GST-KIX with 160 U thrombin (GE Healthcare) overnight at room temperature. Resin was centrifuged at 500 x g for 5 min. Supernatant containing cleaved KIX was collected and dialyzed at 4° C against 1 L of 50 mM MOPS pH 6.5, 50 mM NaCl, 10% glycerol, 1 μM tris-2-carboxyethylphosphine (TCEP) overnight at 4˚ C with mixing. Cleaved KIX was purified using a linear gradient of 50 mM to 1 M NaCl over ten column volumes by cation exchange chromatography using MonoS 5/50 GL column at a flow rate of 1 mL per minute (GE Healthcare). Fractions containing purified KIX were confirmed by SDS-PAGE and dialyzed against 1 L of 50 mM potassium phosphate pH 5.5, 150 mM NaCl, 10 μM TCEP, 30% glycerol overnight at 4˚ C with mixing. Purified protein was aliquoted and stored at -80° C.

Microscale thermophoresis

Binding of purified recombinant KIX with fluorescein isothiocyanate (FITC)-conjugated peptides was measured by microscale thermophoresis using the Monolith NT.115 (NanoTemper Technologies). Assays were conducted in 50 mM sodium phosphate, 150 mM NaCl, 0.01% NP-40, pH 5.5. FITC-conjugated peptides (FITC-CREBMIM at 300 nM, FITC-CRYBMIM at 250 nM, and FITC-MYBMIM at 2000 nM, as based on the optical absorbance measurements of FITC at 495 nm) were mixed with increasing concentrations of purified KIX (0.0015 to 50 μM, 1:1 serial dilutions) and loaded into MST Premium Coated capillaries. MST measurements were recorded at room temperature for 10 sec per capillary using fixed IR-laser power of 80% and LED excitation power of 40-50%.

Streptavidin affinity chromatography

Streptavidin magnetic beads (Pierce) were washed with 30 mM Tris-HCl pH 7.4, 150 mM NaCl, 0.1% Tween-20 (TBST) twice prior to use. For each purification, 100 μL of streptavidin beads were used (1 mg beads, binding capacity 3500 pmol biotinylated fluorescein per mg). Biotinylated peptides were bound to streptavidin bead slurry by incubation at room temperature for 1 h in TBST. Peptide-bound beads were washed twice in TBST and immediately used for purifications. Nuclear lysates were extracted as described below for co-immunoprecipitation. Twenty million cells were used per purification. Nuclear lysates were incubated with Bio-CRYBMIM or Bio-CREBMIM as indicated for 1 h at room temperature with rotation. Beads were washed twice in lysis buffer and separated for subsequent competition. Per competition, beads were incubated in a total of 1 mL of lysis buffer supplemented with competing peptide for 1 h at room temperature with rotation. Beads were washed twice in lysis buffer. Bound proteins were eluted by adding 40 μL of Western blot sample buffer described below and incubated for 20 min at 95° C, with vortexing half-way through.

Sequence analysis

Sequence alignment was performed and identity/similarity of each set of sequences were calculated by EMBOSS Needle using the Needleman-Wunsch algorithm from EMBL-EBI (https://www.ebi.ac.uk/Tools/psa/).

Confocal fluorescence microscopy

Confocal imaging was performed using the Zeiss LSM880 confocal microscope and 63X objective with 1.5 micron z-stack images. Nunc Lab-tek II 8-chamber coverslips were prepared for cell adhesion by the addition of poly-L-Lysine and incubation at room temperature for 1 h. Poly-L-lysine solution was removed from each chamber and chambers were allowed to air dry. 2 x 10^5 cells in 200 μL of fresh media were added to each chamber and incubated for 1 hour at 37° C for attachment. FITC-conjugated peptides were added to cell suspensions at a concentration of 100 nM, mixed, and incubated for 1 hour at 37° C. Cells were counter-stained using Hoechst 33342 and Mitotracker Red CMX ROS (MProbes) for 10 minutes at a final dilution of 1:10,000 prior to imaging.

Colony formation assays

Mononuclear cells were isolated from blood using Ficoll-Paque PLUS density centrifugation and enriched for $CD34^+$ cells using the CD34 MicroBead Kit UltraPure, according to the manufacturer's instructions (MACS Miltenyi Biotech, Bergisch Gladbach, German). Methocult H4034 Optimum (StemCell Technologies) semi-solid media, which contains recombinant human SCF, GM-CSF, G-CSF, IL-3, and erythropoietin, was used for the growth of hematopoietic progenitor cells in colony-forming units. $CD34^+$ cells or MV411 cells were resuspended in Iscove's Modified Dulbecco's Medium (IMDM, Corning) media supplemented with 2% FBS at a concentration of 2 x10^5 cells/mL. The cell suspension, the indicated peptide solution at the appropriate concentration, and Methocult H4034 were mixed in a ratio of 0.5/0.5/10 (cell suspension/peptide solution/Methocult) for a final cell concentration of 1000 cells/well of 6-well plates. Mixture was vortexed for 30 seconds and incubated at room temperature for 5 minutes. Using a blunt-end 16 G needle (StemCell Technologies), 1.1 mL of the solution was added to each well of 6-well plates. Peptide treatment conditions were analyzed in biological triplicates. Plates were incubated at 37° C with 5% CO2 for 14 days. The plates were imaged using a Zeiss AxioObserver.Z1 (Zeiss, Oberkochen, Germany) with a 10x/0.45NA objective. Entire well was

scanned using transmitted light and the resulting images were stitched using ZEN Blue 2.3 Desk (Zeiss, Oberkochen, Germany) and then exported at half resolution to tif files.

Cell viability studies

Cells were resuspended in fresh media and plated at a concentration of $2x10^5$ cells in 200 μL per well in a 96-well plate. Peptides or PBS control were added at indicated concentrations. Cells were incubated at 37° C with 5% CO_2 for 6 days with media and peptide replacement every 48 hours. On day 6, cell viability was assessed using the CellTiter-Glo Luminescent Viability assay, according to the manufacturer's instructions (Promega). Luminescence was recorded using the Infinite M1000Pro plate reader with an integration time of 250 milliseconds (Tecan). For dose-response assays, cells were resuspended and plated at a concentration of 2000 cells in 200 μL per well of a 96-well plate. MV411 cells were plated in complete RPMI media described above. CD34+ cells isolated from umbilical cord blood were plated IMDM media supplemented with 15% FBS, 100 U/mL penicillin and 100 μg/mL streptomycin, 1% L-glutamine, recombinant human cytokines (PeproTech: 100 ng/mL SCF, 100 ng/mL TPO, 100 ng/mL FLT3, 20 ng/mL IL-6, 20 ng/mL IL-3), and 50 μM β-mercaptoethanol. Increasing concentrations of peptides (0.78 to 100 μM; 1:1 serial dilution) were added as indicated. Cells were incubated for 48 hours at 37° C with 5% CO_2. Cell viability was assessed using Cell Titer Glo as described above.

CRISPR competitive assays

Cas9-expressing AML cell lines, MOLM13, MV411, OCIAML3, Kasumi1 and K562, were established by lentiviral transduction with a Cas9 expression vector EFS-Cas9-P2A-Puro, as described (Lu et al., 2018; Tarumoto et al., 2018). Indicated gene-targeting sgRNAs were cloned into LRG2.1 (U6-sgRNA-GFP) or LRC2.1 (U6-sgRNA-mCherry), as described (Lu et al., 2018; Tarumoto et al., 2018). Specific sgRNA sequences are listed in Supplementary File 1c. Lentivirus for each sgRNA was produced by transfecting HEK293T cells with sgRNA-expression vector and helper plasmids, pMD2.G and psPAX2, using TransIT-LT1 Transfection Reagent (Mirus Bio LLC, Madison, WI, USA) according to the manufacture's instruction. Virus supernatant was collected at 48 and 72 hours post-transfection, pooled, filtered, concentrated by centrifugation using the Amicon Ultra-15 Centrifugal Filter Units (EMD Millipore, Darmstadt, Germany) and stored at -80 °C. Cas9-expressing AML cells were transduced with sgRNA virus particles by spin infection (3500 rpm, 35 °C, 90 minutes) and the subsequent overnight incubation (37 °C with 5% CO_2) in the presence of 8 μg/ml polybrene. Fresh complete media was supplied to the cells on the next day and every 3 days subsequently. One week after infection, cells were treated with 10 μM or 20 μM of CRYBMIM or PBS for two days. After treatment completion, live cells were purified using EasySep Dead Cell Removal (Annexin V) Kit (StemCell Technologies). The remaining viable cells were further incubated in complete media without CRYBMIM for 6-9 days with media replacement every 3 days. mCherry- and GFP-expressing cells were quantified using flow cytometry (BD Fortessa, Becton Dickinson, San Jose, CA).

Western blot analysis

Cells were lysed in 30 mM Tris-HCl pH 6.8, 1% SDS, 2% beta-mercaptoethanol, 7% glycerol, 0.0002% Bromophenol Blue buffer or Laemmli sample buffer (BioRad) supplemented with protease inhibitors at a ratio of 100 or 200 μL sample buffer per 1 million cells. Cell

suspensions were incubated at 95° C for 15 min, with vortexing every 5 min. Lysates were clarified by centrifugation for 5 min at 18,000 x g. Twenty μL of clarified lysates were resolved by sodium dodecyl sulfate-polyacrylamide gel electrophoresis (SDS-PAGE) using 4-12% or 10% polyacrylamide Bis-Tris gels (Invitrogen) and transferred onto Immobilon FL PVDF or P PVDF membranes (Millipore, Billerica, MA, USA) at 30V for 30-120 min, for fluorescent or chemiluminescent blotting, respectively. For fluorescent Western blotting, membranes were blocked using Odyssey Blocking buffer (Li-Cor, Lincoln, Nebraska, USA). Blots were incubated in primary antibodies as indicated. Blotted membranes were visualized using secondary antibodies conjugated to IRDye 800CW or IRDye 680RD (goat anti-rabbit, 1:15,000, and goat anti-mouse, 1:15,000) and the Odyssey CLx fluorescence scanner, according to manufacturer's instructions (Li-Cor, Lincoln, Nebraska, USA). After visualization, bands of interest were selected and signal intensity was quantified using the Image Studio Lite. For some whole cell lysate analysis and all co-IP experiments, chemiluminescent Western blotting was used. Blotted membranes were blocked using 5% non-fat milk in TBS, incubated in primary antibodies as indicated, and visualized using HRP-conjugated secondary antibodies (donkey anti-rabbit, 1:15,000, and sheep anti-mouse, 1:15,000, GE Healthcare) and ECL substrate (SuperSignal West Femto Maximum Sensitivity Substrate and Atto Ultimate Sensitivity Substrate, ThermoFisher) with Amersham ImageQuant 800 OD, according to manufacturer's instructions (Cytiva, Marlborough, MA, USA). After imaging, protein signal intensity was quantified using ImageJ. All antibodies are listed in Key Resource Table.

Nuclear isolation from AML cells

Nuclear purifications were carried out per 100 million cells. Cells were collected by centrifugation at 400 x g for 5 min and washed in cold PBS. Washed cell pellets were resuspended in 15 mL hypotonic buffer (10 mM HEPES pH 7.9, 10 mM NaCl, 1 mM $MgCl_2$, 0.5 mM DTT, protease inhibitors) and incubated on ice for 1 hour. Cells were lysed using 40 strokes by Dounce homogenization. Suspensions were then centrifuged for 15 min at 3300 x g to pellet nuclei. Nuclear pellets were further purified by sucrose density gradient centrifugation. Pellets were resuspended in 2.5 mL of 0.025 M Sucrose, 10 mM $MgCl_2$ and layered on top of 2.5 mL 0.88 M sucrose, 0.05 mM $MgCl_2$ and centrifuged for 10 min at 1200 x g. The final nuclear pellet was resuspended in 4 mL lysis buffer (50 mM Tris-HCl pH 7.4, 150 mM NaCl, 0.25 mM EDTA, 1 mM DTT, 0.5% Triton X-100, 10% glycerol, protease inhibitors) and incubated on ice for 20 min. Nuclear suspensions were homogenized by 15 strokes in a Dounce homogenizer without frothing, and clarified by centrifugation for 15 min at 18,000 x g. Clarified lysates were immediately used for immunoprecipitations.

Co-immunoprecipitation

For MYB immunoprecipitations, 7.5 μg of anti-MYB antibodies (EP769Y, Abcam) were conjugated to 1 mg of M-270 Epoxy-coated magnetic beads (Invitrogen) according to manufacturer's instructions. For CBP immunoprecipitations, 50 μL of each of Protein A and Protein G Dynabeads (Invitrogen) were combined and washed in 1 mL of PBS with 0.5% BSA. Fifteen μg of anti-CBP antibodies were added to Protein A/G beads in 1 mL PBS with 0.5% BSA and incubated for 1 h at room temperature with rotation. Beads were then washed with 1 mL PBS with 0.5% BSA and beads were resuspended in a final volume of 100 μL of PBS with 0.5% BSA. One hundred million cells were used per immunoprecipitation. For displacement assays, cells

were treated with 10 μM peptides as indicated for 1 hour at 37° C in complete RPMI media prior to nuclear isolation. Immunoprecipitations were carried out using 100 μL of respective antibody-bead slurry per immunoprecipitation overnight at 4° C with rotation. Beads were washed 3 times with 1 mL of cold lysis buffer. Proteins were eluted in 40 μL of 0.2 M glycine pH 3 for 30 min on a ThermoMixer (Eppendorf) at 900 rpm at room temperature. Eluates were neutralized with 8 μL of 1 M Tris, pH 11. Samples were prepared for Western blot by addition of Western blot sample buffer described above together with 2.5 uL of 1M DTT and incubated at 95° C for 5 min.

Quantitative RT-PCR

Cells were treated as described above for cell viability assays for indicated times points. RNA was isolated using RNeasy kit according to the manufacturer's instructions (Qiagen). Complementary DNA was synthesized using the SuperScript III First-Strand Synthesis system according to the manufacturer's instructions (Invitrogen). Quantitative real-time PCR was performed using the KAPA SYBR FAST PCR polymerase with 200 ng template and 200 nM primers, according to the manufacturer's instructions (Kapa Biosystems, Wilmington, MA, USA). Ct values were calculated by ROX normalization using the ViiA 7 software (Applied Biosystems).

Chromatin immunoprecipitation and sequencing

To prepare antibody-coupled beads, 30 μg of antibodies as indicated per ChIP were incubated with 1 mg of 1:1 Protein A/Protein G slurry in PBS with 0.5% BSA overnight at 4° C with rotation. Beads were washed twice in PBS with 0.5%. Fifty million cells were used per ChIP assay. Cells were fixed in 1% formaldehyde for 10 minutes at room temperature. Crosslinking was quenched by adding glycine to a final concentration of 125 mM and incubating at room temperature for 5 min. Cells were pelleted by centrifugation at 500 x g at 4° C for 5 min. Cells were washed twice by resuspending 5 mL of PBS with 1 mM PMSF and centrifuging at 500 x g at 4° C for 5 min. Wash step was repeated twice. Crosslinked pellets were resuspended in 2 mL of 50 mM Tris-HCl pH 8.1, 100 mM NaCl, 5 mM EDTA, 0.2% NaN_3, 0.5% SDS, and protease inhibitors. Nuclei were pelleted by centrifugation at 15,000 x g for 10 min at 4° C. Pellets were resuspended in 50 mM Tris-HCl, 100 mM NaCl, 5 mM EDTA, 0.2% NaN_3, 0.3% SDS, 1.5% Triton X-100, and protease inhibitors and sonicated using the Covaris S220 adaptive focused sonicator at 5% duty Factor, 140W peak incident power, 200 cycles per burst for 30 min at 4° C to obtain 100-500 base pair chromatin fragments (Covaris, Woburn, CA). Nuclear sheared lysates were clarified by centrifugation at 15,000 x g for 10 min at 4° C. Supernatants were incubated with antibody-coupled Protein A/G beads as indicated overnight at 4° C with rotation. Beads were washed 3 times in 1 mL of 50 mM HEPES-KOH pH 7.6, 500 mM LiCl, 1 mM EDTA, 1% NP-40, 0.7% Na deoxycholate. For the final wash, 1 mL of 50 mM Tris-HCl pH 8, 10 mM EDTA, 50 mM NaCl was added to the beads. Beads were centrifuged for 3 min at 960 x g at 4° C and supernatant was removed. To elute, 210 μL of 50 mM Tris-HCl pH 8, 10 mM EDTA, 1% SDS was added to the beads and incubated for 30 min at 65° C. Beads were centrifuged for 1 min at 16,000 x g at room temperature. Supernatant contains eluted samples. Crosslinks were reversed by incubation overnight at 65° C. Samples were diluted to 400 μL with 50 mM Tris-HCl pH 8, 10 mM EDTA, 50 mM NaCl, and 4 μL of 500 ug/ml RNase (Roche, Cat. No 11119915001) was added and incubated for 1 h at 37° C to digest RNA. Proteins were then digested by addition of 2 μL 20 mg/mL Proteinase K (Roche) and incubation for 2 h at 55° C. Samples were purified using PureLink PCR Purification Kit. Libraries were prepared using the KAPA HTP Library preparation kit (Roche),

according to the manufacturer's instructions, and sequenced on the Illumina HiSeq 2500 instruments, with 20-30 millions of 50-bp paired-end reads for each sample.

For ChIP-seq analysis, reads were quality and adapter trimmed using 'trim_galore' before aligning to human genome assembly hg19 with bowtie2 using the default parameters. Aligned reads with the same start position and orientation were collapsed to a single read before subsequent analysis. Density profiles were created by extending each read to the average library fragment size and then computing density using the BEDTools suite. Enriched regions were identified using MACS 2.0 and scored against matched input libraries. Genomic 'blacklisted' regions were filtered (http://www.broadinstitute.org/~anshul/projects/encode/rawdata/blacklists/hg19-blacklist-README.pdf) and remaining peaks within 500 bp were merged. Read density normalized by sequencing depth was then calculated for the union of peaks, and peak dynamics were assessed in DESeq2 using a fold change of 1.5 and an FDR-adjusted p-value of 0.05.

RNA sequencing

Cells were treated with peptide or control in triplicate as described above for cell viability assays at 20 μM for 1 hour and 4 hours. Cells were collected and RNA was isolated using RNeasy kit (Qiagen) according to manufacturer's instructions. After RiboGreen quantification and quality control by Agilent BioAnalyzer, 500 ng of total RNA underwent polyA selection and TruSeq library preparation according to instructions provided by Illumina (TruSeq Stranded mRNA LT Kit), with 8 cycles of PCR. Samples were barcoded and run on a HiSeq 4000 as PE100, using the HiSeq 3000/4000 SBS Kit (Illumina). An average of 58 million paired reads was generated per sample. At most, ribosomal reads represented 2.9% of the total reads generated and the percent of mRNA bases averaged 74%. Reads were quality and adapter trimmed using 'trim_galore' before aligning to human assembly hg19 with STAR v2.5 using the default parameters. Coverage and post-alignment quality were assessed using the Picard tool CollectRNASeqMetrics (http://broadinstitute.github.io/picard/). Read count tables were created using HTSeq v0.6.1. Normalization and expression dynamics were evaluated with DESeq2 using the default parameters.

Genome annotations and gene expression estimation

The UCSC knownGene (Meyer et al., 2013), Ensembl 71 (Flicek et al., 2013), and MISO v.2.0 (Katz et al., 2010) annotations were combined into a single genome annotation. Gene expression was estimated as previously described (Dvinge et al., 2014). RSEM v.1.2.4 (B. Li & Dewey, 2011) was modified to invoke Bowtie v.1.0.0 (Langmead et al., 2009) through the '-v 2' option in order to map all reads to the merged genome annotation and obtain gene expression estimates. With TopHat v.2.1.1 (Trapnell et al., 2009), the remaining unaligned reads were mapped to the human genome (GRCh37/hg19) and a database of splice junctions. All expression estimates were normalized via the trimmed mean of M values (TMM) method (Robinson & Oshlack, 2010).

Gene expression analyses

A minimum absolute log2(expression fold-change) requirement was selected to identify differentially-expressed genes between CRYBMIM and PBS treatment, in the maximal number of AML cell lines tested. Feasible thresholds were restricted to expression differences of at least 1.5-fold and associated sample group comparison p-values < 0.05. Unsupervised clustering on AML cell lines was based on 41 genes which best separated the CRYBMIM- and PBS-treated samples (Figure 9-figure supplement 1A). These genes were differentially-expressed in at least 4 AML cell lines, with a minimum absolute log2(expression fold-change) = 0.794. Clustered gene expression heatmaps were created with the pheatmap package (Kolde, 2012/2020), using Ward's minimum variance method and a Euclidean distance for hierarchical clustering. For sample group comparisons of differential gene expression, a two-sided t-test was used to determine statistical significance. Statistical analyses were performed in the R programming environment with Bioconductor (Huber et al., 2015) and the dplyr (Wickham et al., 2020) package. The associated figures were created using the ggplot2 (Wickham, 2016) package.

Flow cytometry

MV411 cells were resuspended to a concentration of $1x10^6$ cells per mL and plated in 12-well tissue culture plates. To assess apoptosis, MYBMIM was used as a positive control and cells were treated as described (Ramaswamy *et al.*, 2018). Cells were treated with 20 μM CRYBMIM for one hour. Following peptide treatment, cells were washed with PBS and resuspended with PBS with the addition of Annexin V-FITC (1:50) and CD11b (1:50). Cells were incubated on ice for 40 minutes followed by two washes with cold PBS. DAPI was added prior to flow cytometric analysis (1:10,000).

Gene dependency analysis across cancer cell types

CRISPR knockout screen gene effect data from Project Achilles 19Q4 was downloaded from the DepMap Consortium (DepMap, Broad (2019): DepMap 19Q4 Public Dataset doi:10.6084/m9.figshare.11384241.v2). Dependency scores for each gene were averaged by tumor type. A differential dependency score was then calculated as the relative difference between the average gene dependency score for a tumor type and the average gene dependency score across all cell types. All genes were then ranked by leukemia gene differential dependency scores, and the top 10 and bottom 10 leukemia gene dependencies were plotted as a heat map. P-values were calculated comparing MYB dependency in leukemias versus all other tumor types using two-tailed t-test.

Mass spectrometry proteomics

Immunoprecipitations were carried out as described above in biological triplicates. Eluates were resolved by SDS-PAGE 10% polyacrylamide Bis-Tris gels (Invitrogen) at 100 V for 5 minutes. To visualize proteins, gels were stained using Silver Stain for Mass Spectrometry kit (Pierce) according to manufacturer's instructions. Relevant gel portions were excised and destained using 50 μL of 30 mM $K_3[Fe(CN)_6]$ in 100 mM aqueous $Na_2S_2O_3$ by incubation at room temperature for 30 minutes, with gentle mixing halfway through. Following destaining, 500 μL of 25 mM aqueous NH_4HCO_3 were added to each tube and incubated for 5 min at room temperature on a ThermoMixer (Eppendorf) at 700 rpm. Solution was removed and gel pieces were washed

by adding 500 μL of 50% acetonitrile in 25 mM aqueous NH_4HCO_3 and incubating for 10 min at room temperature on a ThermoMixer at 700 rpm. Wash step was repeated 2 more times. All solution was removed and 100 μL of acetonitrile was added to each tube and incubated for 5 min at room temperature on a ThermoMixer (Eppendorf) at 700 rpm. All solution was removed and destained gel fragments were vacuum centrifuged and stored at -20C. For reduction of disulfide bonds, gel fragments were re-hydrated in 25 μL of 10 mM dithiothreitol in 100 mM aqueous NH_4HCO_3 for 1 h at 56C. Tubes were cooled to room temperature. For alkylation of thiols, 25 μL of 55 mM iodoacetamide in 100 mM aqueous NH_4HCO_3 was added to each tube and incubated for 30 min at room temperature in the dark. To quench the alkylation reaction, 5 μL of 100 mM dithiothreitol in 100 mM aqueous NH_4HCO_3 was added and incubated for 5 min at room temperature. Gel fragments were washed by adding 50 μL of acetonitrile and incubation for 5 min at room temperature followed by addition of 500 μL of 100 mM aqueous NH_4HCO_3 and incubation for 10 min at room temperature. All solution was removed and wash step was repeated. All solution was removed and 100 μL of acetonitrile was added and tubes were incubated for 10 min at room temperature. All solution was removed and gel fragments were vacuum centrifuged and stored at -20C. For digestion of proteins into peptides, gel fragments were cooled on ice. Protease LysC was added at a ratio of 1:25 protease:protein, assuming 1 μg of protein per immunoprecipitation. Gel fragments were incubated for 5 min on ice. Samples were diluted to 50 μL, or to cover gel fragments using 50 mM aqueous NH_4HCO_3. Digestion was carried out for 4 hours at 37C. Following LysC digestion, trypsin was added to each tube at the 1:25 protease:protein ratio in 50 mM aqueous NH_4HCO_3. Trypsin digestion was carried out for 16 hours at 37C. To elute peptides from gel fragments, 50 μL of 1% formic acid in 70% acetonitrile was added to each tube and incubated for 30 min at room temperature on a ThermoMixer at 1400 rpm. Eluates were removed and saved, and elution step was repeated with fresh 1% formic acid in 70% acetonitrile. New eluates were pooled with the first elution for a total of 100 μL of eluate per sample. Samples were vacuum centrifuged to dryness. Prior to mass spectrometry analysis, samples were desalted and purified by solid phase extraction using C18 Micro SpinColumns (Nest Group) and eluted with 70% acetonitrile supplemented with 0.1% formic acid. Eluates were vacuum centrifuged to remove all solution. Samples were resuspended in 8 μL of 0.1% aqueous formic acid and sonicated for 5 minutes to ensure full resuspension. Three μL of each sample were used for mass spectrometry analysis.

The LC system used a vented trap-elute configuration (EasynLC1000, Thermo Fisher scientific) coupled to an Orbitrap Lumos mass spectrometer (Thermo Fisher Scientific, San Jose, CA) via a nano electro-spray DPV-565 PicoView ion source (New Objective). The trap column was fabricated with a 5 cm × 150 μm internal diameter silica capillary with a 2 mm silicate frit, and pressure loaded with Poros R2-C18 10 μm particles (Life Technologies). The analytical column consisted of a 25 cm × 75 μm internal diameter column with an integrated electrospray emitter (New Objective), packed with ReproSil-Pur C18-AQ 1.9 μm particles (Dr. Maisch). Peptides were resolved over 90 min using a 3%-45% gradient of acetonitrile with 0.1% aqueous formic acid at 250 nL/minute.

Precursor ions in the 375–3000 m/z range were isolated using the quadrupole and recorded every 3 s using the Orbitrap detector (60,000 resolution, with 445.1200 ions used as lockmass), with an automatic gain control target set at 10^6 ions and a maximum injection time of 50 ms. Data-dependent precursor ion selection was enforced, limiting fragmentation to monoisotopic ions with charge 2–5 and precursor ion intensity greater than $5x10^4$, and dynamically excluding already fragmented ions for 30 s (10 ppm tolerance). Selected ions were isolated (Q1 isolation window 0.7 Th) and fragmented using HCD (normalized collision energy 30)

using the top speed algorithm. Product ion spectra were recorded in the Orbitrap at 30,000 resolution (AGC of $8x10^4$ ions, maximum injection time 54 ms), in profile mode.

Mass spectra were analyzed using MaxQuant (version 1.6.0.16). For identification, spectra were matched against the human UniProt database (as of October 2017), supplemented with contaminant proteins from the cRAP database with FDR <0.01. After m/z recalibration, mass tolerance was set at 4.5 and 20 ppm for precursor and fragment ions, respectively. Cysteine carbamidomethylation was set as fixed chemical modification, while methionine oxidation and protein N-terminus acetylation were set as variable. Protease specificity was set to trypsin/P, with up to two missed cleavages allowed. The match between runs feature was enabled (0.7 min tolerance, 20 min alignment). Quantification was performed using the LFQ algorithm.

Contaminating peptides such as keratin and non-human proteins were excluded and label-free quantification (LFQ) intensity values for protein groups were used for analysis. IgG and MYB immunoprecipitation samples were analyzed together (3 replicates per condition; 6 samples total). Proteins in the following categories were excluded from analysis: (i) zero LFQ intensity across all replicates, (ii) zero LFQ intensity in 5 of 6 replicates, (iii) proteins with LFQ intensity recorded in only 1 replicate in both sets of samples. Enrichment scores were defined as the log2 ratio of MYB:IgG.

Statistical analysis, principal component analysis and hierarchical clustering

OriginPro 2018 (Origin Lab) was used for statistical analysis. Principal component analysis was performed using prcomp (R Studio). The hierarchical cluster analysis was carried out with R function pheatmap with Pearson's distance as the distance metrics and "average" as the clustering method.

SUPPLEMENTAL INFORMATION

All supplemental data are available openly via Zenodo (https://doi.org/10.5281/zenodo.4321824). Mass spectrometry proteomics data are available via PRIDE (PXD019708). Gene expression and chromatin dynamics data are available via Gene Expression Omnibus (GSE163470).

ACKNOWLEDGEMENTS

We thank all our laboratory members, especially Benjamin Herzberg, Shray Khanna and Isaac Krasnopolsky, as well as Henrik Molina, Caitlin Steckler, and the MSK Integrated Genomics Operation core for technical assistance. We thank Alejandro Gutierrez, Marc Mansour, Kristian Helin and Yaniv Kazansky for critical comments on the manuscript. This research was supported by the NIH R01 CA204396, R01 DK103854, R01 HL128239, R01 HL151651, R01 CA251138, T32 GM073546, P30 CA008748, St. Baldrick's Foundation, Hyundai Hope on Wheels, Burroughs Wellcome Fund, Damon Runyon-Richard Lumsden Foundation, Rita Allen Foundation, Leukemia & Lymphoma Society, Blood Cancer Discoveries Grant program (Leukemia & Lymphoma Society 8023-20), the Starr Cancer Consortium, Mr. William H. and Mrs. Alice Goodwin and the Commonwealth Foundation for Cancer Research the Center for Experimental Therapeutics at MSKCC, Edward P. Evans Foundation, Mark Foundation for Cancer Research, and the Paul G. Allen Frontiers Group.

DECLARATION OF INTERESTS

A patent application related to this work has been submitted to the U.S. Patent and Trademark Office entitled ''Agents and methods for treating CREB binding protein-dependent cancers'' (application PCT/US2017/059579). AK is a consultant for Novartis and Rgenta.

FIGURE LEGENDS

Figure 1. CBP depletion is required to confer resistance to MYBMIM in AML cells. (A) Schematic of the genome-wide CRISPR screen to identify genes whose loss modifies MYBMIM effects in MOLM13 cells expressing Cas9. Cells were transduced with the GeCKOv2 library expressing single sgRNAs at low multiplicity of infection, followed by 3-day treatment with 10 μM MYBMIM versus PBS control, with the sgRNA representation assessed by DNA sequencing. **(B)** Volcano plot showing the relative abundance of cell clones expressing sgRNAs targeting specific genes (fold change of MYBMIM-treated cells at T1 versus T0) and their statistical significance from biological replicates. Dashed line represents no enrichment, with positive values representing genes whose depletion confers relative resistance to MYBMIM. CBP is marked in red.

Figure 2. CRYBMIM is an improved peptidomimetic chimera that specifically binds the KIX domain of CBP/P300 in vitro and in cells. (A) Heatmap of the top 10 and bottom 10 gene dependencies for survival and proliferation of 652 cancer cell lines in the DepMap Cancer Dependency Map Project, ranked by the greatest dependency for 37 leukemia lines, 20 of which are AML cell lines, as indicated by the red color gradient; * p = 1.1e-15, t-test of leukemia versus other tumor types. **(B)** Retro-inverso amino acid sequences of MYBMIM, CREBMIM and CRYBMIM, with amino acids derived from MYB, CREB, and TAT marked in blue, green, and black, respectively. **(C)** Molecular model of the CRYBMIM:KIX complex. Residues making contact with KIX are labeled, with portions derived from MYB and CREB marked in blue and green, respectively. **(D)** Binding of FITC-conjugated CREBMIM (blue), CRYBMIM (red), and MYBMIM (black), as measured using microscale thermophoresis; K_d = 2.9 ± 0.7, 5.7 ± 0.2, and 17.3 ± 1.6, respectively. Error bars represent standard deviations of three biological replicates; p < 1e-15, ANOVA, for CRYBMIM versus MYBMIM. **(E)** Western blot showing binding of nuclear CBP/P300 isolated from AML cells to biotinylated CRYBMIM or CREBMIM, specifically competed by the excess free peptides as indicated. **(F)** Quantification of CBP/P300 binding to CRYBMIM and CREBMIM by fluorescence densitometry, with black, gray and red denoting PBS control, TAT control, and peptide competition, respectively.

Figure 3. Potent and broad-spectrum activity of CRYBMIM against diverse AML cell lines but relatively sparing of normal hematopoietic progenitor cells. (A) Representative live cell confocal microscopy images of MV411 cells treated with 100 nM FITC-conjugated peptides as indicated for 1 hour, counterstained with Mitotracker (red) and Hoechst 33342 (blue). Scale bar indicates 20 μm, with z-stack of 1.5 μm. **(B)** Western blots showing immunoprecipitated nuclear CBP/P300 co-purified with MYB and CREB from MV411 cells treated with 10 μM peptides as indicated for 1 hour. **(C-D)** Cell viability of MV411 cells as a function of increasing concentrations of 48-hour peptide treatment, comparing (C) CRYBMIM to MYBMIM, CREBMIM and MLLMIM (IC_{50} = 6.88 ± 3.39, 13.1 ± 3.3 29.15 ± 3.79, and 24.22 ± 2.00, p < 1e-15, ANOVA); (D) TG3 and CG3 (IC_{50} = 16.65 ± 1.00 and 48.91 ± 2.55, p <1e-15, ANOVA). Error bars represent standard deviation of three biological replicates. **(E)** Colony forming ability of CD34+ cells isolated from human umbilical cord blood (CD34+ CB, gray) and MV411 AML (red) cells following CRYBMIM or MYBMIM treatment. Data represent three biological replicates; *p = 7.4e-5, t-test of normal CD34+ CB versus MV411 AML cells. **(F)** Preservation of clonogenic capacity of CD34+ CB cells in differentiating into erythroid blast forming units (BFU-E, light gray) and granulocyte macrophage colony forming units (CFU-GM, gray) as a function of CRYBMIM treatment. **(G)** Cell viability of AML cell lines treated with control PBS (black), 20 μM CREBMIM (blue), MYBMIM (gray), or

CRYBMIM (red) as indicated for 6 days with media replacement every 48 hours in three biological replicates (p = 8.6e-3, t-test for CRYBMIM versus control).

Figure 4. CBP but not P300 is dispensable for the growth and survival of AML cells, and is required for the susceptibility to peptidomimetic MYB blockade by CRYBMIM. (A) Schematic of the competitive assays to define specific genetic dependencies. AML cells expressing Cas9 and GFP are transduced with sgRNAs targeting specific genes and expressing mCherry, followed by quantitation of cell abundance by fluorescence activated cell scanning (FACS) of GFP and mCherry-expressing cells. **(B)** Western blots demonstrating specific depletion of CBP in MV411 (left) and MOLM13 (right) cells expressing sgCBP-1 and sgCBP-2, as compared to control sgNEG1 and sgNEG2 targeting the *AAVS1* safe harbor locus. EP300 is shown for specificity, and Actin serves as the loading control. **(C)** Relative growth of GFP-expressing MOLM13 cells expressing mCherry and unique sgRNAs targeting *AAVS1* control (sgNEG1 and sgNEG2), *CBP* (sgCBP-1 and sgCBP-2), and *P300* (sgEP300-1 and sgEP300-2) and quantified by FACS on day 0, 3, and 6 after two-day treatment with 10 μM CRYBMIM or PBS. Data represent biological triplicates of at least 10,000 cells per condition; *p = 6.0e-10, **p = 4.1e-8, t-test for day 6 versus day 0 of CRYBMIM treatment of CBP-depleted cells. **(D)** Analogous experiment as (C) using MV411 cells; *p = 1.1e-6, **p = 3.7e-6, t-test for day 6 versus day 0 of CRYBMIM treatment of CBP-depleted cells.

Figure 5. CRYBMIM blocks oncogenic MYB gene expression and restores normal myeloid cell differentiation. (A-B) Volcano plots of normalized gene expression of MV411 cells upon one (A) and four hour (B) treatment with CRYBMIM, as compared to PBS control, with select genes labeled; p-values denote statistical significance of 3 biological replicates. **(C-E)** Gene set enrichment analysis of up- and down-regulated gene sets: (C) MYB_Q6, (D) GSE9988_LPS_VS_VEHICLE_TREATED_MONOCYTES_UP, and (E) GERY_CEBP_TARGETS_377. **(F)** Histogram of Annexin V- or CD11b-stained MV411 cell fluorescence, treated with CRYBMIM (red), MYBMIM (gray), or control PBS (black); * p < 1e-15, Kruskal-Wallis test. **(G)** Scatter plots comparing Annexin V- versus CD11b-stained MV411 cell fluorescence, treated with control PBS, MYBMIM or CRYBMIM; blue to red color indicates increasing cell density.

Figure 6. CRYBMIM remodels MYB and CBP/P300 chromatin complexes in AML cells. (A-B) Volcano plots of relative MYB chromatin occupancy in MV411 cells changes after one hour (A) and four hours (B) of 20 μM CRYBMIM treatment compared to PBS control, as analyzed by ChIP-seq. Sequence motifs found in CRYBMIM-induced MYB-depleted (left) and MYB-enriched loci (right) are shown. p-values denote statistical significance of 3 technical replicates. **(C-D)** Volcano plots of CBP/P300 chromatin occupancy changes after one hour (C) and four hours (D) of 20 μM CRYBMIM treatment as compared to control, as analyzed by ChIP-seq. Sequence motifs found in CRYBMIM-induced CBP/P300-depleted (left) and CBP/P300-enriched loci (right) are shown. p-values denote statistical significance of 3 technical replicates.

Figure 7. MYB assembles aberrant nuclear transcription factor complexes in AML cells. (A) Volcano plot of nuclear MYB-associated proteins compared to IgG control, as analyzed by affinity purification-mass spectrometry of MV411 cells. Red symbols denote specifically MYB-associated proteins, as defined by association with CBP (MYB/IgG $\log_2$>1). p-values denote statistical significance of 3 biological replicates. **(B)** Enrichment of MYB-associated proteins (red) as a function of their corresponding CRISPR DepMap dependency scores in MV411 cells. Red

symbols denote functionally required proteins, as defined by the genetic dependency of CBP (score<-0.18). **(C)** Network of BioGRID protein interactions for MYB-associated nuclear AML proteins as a function of their respective hematopoietic expression aberrancy scores, based on their relative gene expression in AML cells as compared to normal bone human bone marrow progenitor cells (white to red color gradient indicates increasingly aberrant gene expression). **(D)** Comparison of the genetic dependency scores in leukemia cell lines as compared to all other non-hematopoietic cancer cell lines for MYB-associated nuclear AML proteins, with red symbols denoting proteins that are required in leukemia as compared to non-hematopoietic cancers.

Figure 8. MYB and CBP/P300 assemble convergently organized nuclear transcription factor complexes in genetically diverse AML cells. (A-B) Western blots of specific transcription factors in immunoprecipitated MYB (A) and CBP/P300 (B) nuclear complexes in seven genetically diverse AML cell lines, as indicated. Blue and red bands indicate molecular weight markers. LaminB1 serves as the loading control.

Figure 9. Specific MYB complex factors are aberrantly expressed and assembled in AML as compared to normal human blood cells. (A) Western blots of specific MYB complex transcription factors in normal human blood cells and genetically diverse leukemia cells, as indicated. Actin serves as the loading control. **(B)** Principal component analysis of MYB complex transcription factor abundance, as quantified by image densitometry, as a function of susceptibility of various AML cell lines to CRYBMIM (blue color index). **(C)** Contribution of individual MYB complex transcription factor abundance to the top PCA eigenvector. **(D)** Heatmap of hierarchical clustering of MYB complex individual transcription factor abundance and CRYBMIM susceptibility. **(E)** Western blots of specific transcription factors in specific MYB nuclear complexes immunoprecipitated from normal human umbilical cord mononuclear cells (MNC), as compared to MV411 and HL60 AML cells. Blue and red bands indicate molecular weight markers. LaminB1 serves as loading control.

Figure 10. Peptidomimetic remodeling of MYB transcriptional complexes leads to rapid MYB proteolysis. (A) Quantification of MYB abundance in HL60 cells as a function of duration of 20 μM CRYBMIM treatment (red) as compared to PBS control (black) using Western blot image densitometry. Lines represent single exponential decay fits. Western blots and fits for all cell lines studied are shown in Supplementary Figure 8. Symbols represent biological triplicates. **(B)** MYB protein half-life, as estimated by exponential decay kinetics, in genetically diverse AML cell lines as a function of CRYBMIM susceptibility (Pearson $r = 0.94$, excluding resistant K562). Horizontal bars represent standard deviation of CRYBMIM susceptibility. Vertical bars represent standard deviation of time constants. **(C)** Western blots of MYB and CREB in MV411 AML cells transduced with MSCV retroviruses encoding *GFP* control (MV411-MSCV) or *BCL2* (MV411-BCL2), treated with 20 μM CRYBMIM or PBS control with or without 10 μM of MG132 for one or four hours, as indicated. Actin serves as loading control.

Figure 11. Chromatin dynamics of CRYBMIM remodeled MYB transcription factor complexes in AML cells. (A) Heatmap of transcription factor chromatin occupancy in MV411 cells as a function of time of control PBS or CRYBMIM treatment. Nine clusters identified using k-means clustering are marked by yellow (loss of MYB and CBP), purple (loss of CBP and gain of MYB), orange (gain of MYB and CBP), pink (gain of CBP), and blue (no apparent changes of MYB and CBP) boxes, based on the similarity of their *z*-scores, with red and blue representing

enrichment or depletion of factors, respectively. **(B)** Groups of clusters comprising similar responses to CRYBMIM treatment based on MYB and CBP/P300 dynamics. Sequence motifs enriched at specific loci for each cluster are listed. Factors in white denote factors presumed to be enriched based on sequence motif enrichment.

Figure 12. Peptidomimetic blockade of MYB:CBP/P300 by CRYBMIM releases CBP/P300 that recruits RUNX1 to chromatin. (A-B) Western blots of specific transcription factors in nuclear complexes with immunoprecipitated MYB (A) and CBP/P300 (B) in MV411 cells upon treatment with 10 μM CRYBMIM or PBS control for one hour. Blue and red bands indicate molecular weight markers. LaminB1 serves as loading control. **(C)** Abundance of MYB, CBP/P300 and RUNX1, as measured by Western blot image densitometry, in immunoprecipitated MYB and CBP/300 nuclear complexes in MV411 cells treated with CRYBMIM or PBS control. Symbols represent biological triplicates; $*p$ = 4.7e-6, t-test for CBP in MYB complex upon CRYBMIM treatment, $**p$ = 3.4e-6, t-test for RUNX1 in CBP/P300 complex CRYBMIM treatment.

Figure 13. Convergent organization of aberrant MYB complexes controls oncogenic gene expression in acute myeloid leukemia. Schematic of the molecular organization of MYB transcription factor complexes, induced convergently in genetically diverse subtypes of AML, leading to oncogenic gene expression that requires MYB:CBP/P300 interaction and causes susceptibility to its peptidomimetic remodeling, leading to MYB chromatin eviction and proteolysis, and CBP/P300 release to induce cellular differentiation and apoptosis.

REFERENCES

Armenteros-Monterroso, E., Zhao, L., Gasparoli, L., Brooks, T., Pearce, K., Mansour, M. R., Martens, J. H. A., de Boer, J., & Williams, O. (2019). The AAA+ATPase RUVBL2 is essential for the oncogenic function of c-MYB in acute myeloid leukemia. *Leukemia*, *33*(12), 2817–2829. https://doi.org/10.1038/s41375-019-0495-8

Bell, C. C., Fennell, K. A., Chan, Y.-C., Rambow, F., Yeung, M. M., Vassiliadis, D., Lara, L., Yeh, P., Martelotto, L. G., Rogiers, A., Kremer, B. E., Barbash, O., Mohammad, H. P., Johanson, T. M., Burr, M. L., Dhar, A., Karpinich, N., Tian, L., Tyler, D. S., … Dawson, M. A. (2019). Targeting enhancer switching overcomes non-genetic drug resistance in acute myeloid leukaemia. *Nature Communications*, *10*(1), 2723. https://doi.org/10.1038/s41467-019-10652-9

Bradner, J. E., Hnisz, D., & Young, R. A. (2017). Transcriptional Addiction in Cancer. *Cell*, *168*(4), 629–643. https://doi.org/10.1016/j.cell.2016.12.013

Brown, F. C., Still, E., Koche, R. P., Yim, C. Y., Takao, S., Cifani, P., Reed, C., Gunasekera, S., Ficarro, S. B., Romanienko, P., Mark, W., McCarthy, C., de Stanchina, E., Gonen, M., Seshan, V., Bhola, P., O'Donnell, C., Spitzer, B., Stutzke, C., … Kentsis, A. (2018). MEF2C Phosphorylation Is Required for Chemotherapy Resistance in Acute Myeloid Leukemia. *Cancer Discovery*, *8*(4), 478–497. https://doi.org/10.1158/2159-8290.CD-17-1271

Cancer Genome Atlas Research Network, Ley, T. J., Miller, C., Ding, L., Raphael, B. J., Mungall, A. J., Robertson, A. G., Hoadley, K., Triche, T. J., Laird, P. W., Baty, J. D., Fulton, L. L., Fulton, R., Heath, S. E., Kalicki-Veizer, J., Kandoth, C., Klco, J. M., Koboldt, D. C., Kanchi, K.-L., … Eley, G. (2013). Genomic and epigenomic landscapes of adult de novo acute myeloid leukemia. *The New England Journal of Medicine*, *368*(22), 2059–2074. https://doi.org/10.1056/NEJMoa1301689

Cheng, G., Liu, F., Asai, T., Lai, F., Man, N., Xu, H., Chen, S., Greenblatt, S., Hamard, P.-J., Ando, K., Chen, X., Wang, L., Martinez, C., Tadi, M., Wang, L., Xu, M., Yang, F.-C., Shiekhattar, R., & Nimer, S. D. (2017). Loss of p300 accelerates MDS-associated leukemogenesis. *Leukemia*, *31*(6), 1382–1390. https://doi.org/10.1038/leu.2016.347

Cheng, J. C., Kinjo, K., Judelson, D. R., Chang, J., Wu, W. S., Schmid, I., Shankar, D. B., Kasahara, N., Stripecke, R., Bhatia, R., Landaw, E. M., & Sakamoto, K. M. (2008). CREB is a critical regulator of normal hematopoiesis and leukemogenesis. *Blood*, *111*(3), 1182–1192. https://doi.org/10.1182/blood-2007-04-083600

Dai, P., Akimaru, H., Tanaka, Y., Hou, D. X., Yasukawa, T., Kanei-Ishii, C., Takahashi, T., & Ishii, S. (1996). CBP as a transcriptional coactivator of c-Myb. *Genes and Development*, *10*(5), 528–540. https://doi.org/10.1101/gad.10.5.528

Dvinge, H., Ries, R. E., Ilagan, J. O., Stirewalt, D. L., Meshinchi, S., & Bradley, R. K. (2014). Sample processing obscures cancer-specific alterations in leukemic transcriptomes. *Proceedings of the National Academy of Sciences*, *111*(47), 16802–16807. https://doi.org/10.1073/pnas.1413374111

Flicek, P., Ahmed, I., Amode, M. R., Barrell, D., Beal, K., Brent, S., Carvalho-Silva, D., Clapham, P., Coates, G., Fairley, S., Fitzgerald, S., Gil, L., García-Girón, C., Gordon, L., Hourlier, T., Hunt,

S., Juettemann, T., Kähäri, A. K., Keenan, S., … Searle, S. M. J. (2013). Ensembl 2013. *Nucleic Acids Research*, *41*(D1), D48–D55. https://doi.org/10.1093/nar/gks1236

Gonda, T. J., Buckmaster, C., & Ramsay, R. G. (1989). Activation of c-myb by carboxy-terminal truncation: Relationship to transformation of murine haemopoietic cells in vitro. *The EMBO Journal*, *8*(6), 1777–1783.

Gonda, T. J., Macmillan, E. M., Townsend, P. V, & Hapel, A. J. (1993). Differentiation state and responses to hematopoietic growth factors of murine myeloid cells transformed by myb. *Blood*, *82*(9), 2813–2822.

Goto, N. K., Zor, T., Martinez-Yamout, M., Dyson, H. J., & Wright, P. E. (2002). Cooperativity in transcription factor binding to the coactivator CREB-binding protein (CBP): The mixed lineage leukemia protein (MLL) activation domain binds to an allosteric site on the KIX domain. *Journal of Biological Chemistry*, *277*(45), 43168–43174. https://doi.org/10.1074/jbc.M207660200

Greenblatt, S. M., Man, N., Hamard, P.-J., Asai, T., Karl, D., Martinez, C., Bilbao, D., Stathias, V., Jermakowicz, A. M., Duffort, S., Tadi, M., Blumenthal, E., Newman, S., Vu, L., Xu, Y., Liu, F., Schurer, S. C., McCabe, M. T., Kruger, R. G., … Nimer, S. D. (2019). CARM1 Is Essential for Myeloid Leukemogenesis but Dispensable for Normal Hematopoiesis. *Cancer Cell*, *35*(1), 156. https://doi.org/10.1016/j.ccell.2018.12.008

He, B., Gao, P., Ding, Y.-Y., Chen, C.-H., Chen, G., Chen, C., Kim, H., Tasian, S. K., Hunger, S. P., & Tan, K. (2019). Diverse noncoding mutations contribute to deregulation of cis-regulatory landscape in pediatric cancers. *BioRxiv*, 843102. https://doi.org/10.1101/843102

Hu, Y. L., Ramsay, R. G., Kanei-Ishii, C., Ishii, S., & Gonda, T. J. (1991). Transformation by carboxyl-deleted Myb reflects increased transactivating capacity and disruption of a negative regulatory domain. *Oncogene*, *6*(9), 1549–1553.

Huber, W., Carey, V. J., Gentleman, R., Anders, S., Carlson, M., Carvalho, B. S., Bravo, H. C., Davis, S., Gatto, L., Girke, T., Gottardo, R., Hahne, F., Hansen, K. D., Irizarry, R. A., Lawrence, M., Love, M. I., MacDonald, J., Obenchain, V., Oleś, A. K., … Morgan, M. (2015). Orchestrating high-throughput genomic analysis with Bioconductor. *Nature Methods*, *12*(2), 115–121. https://doi.org/10.1038/nmeth.3252

Jian, W., Yan, B., Huang, S., & Qiu, Y. (2017). Histone deacetylase 1 activates PU.1 gene transcription through regulating TAF9 deacetylation and transcription factor IID assembly. *The FASEB Journal*, *31*(9), 4104–4116. https://doi.org/10.1096/fj.201700022R

Jones, S. (2004). An overview of the basic helix-loop-helix proteins. *Genome Biology*, *5*(6), 226. https://doi.org/10.1186/gb-2004-5-6-226

Kasper, L. H., Lerach, S., Wang, J., Wu, S., Jeevan, T., & Brindle, P. K. (2010). CBP/p300 double null cells reveal effect of coactivator level and diversity on CREB transactivation. *The EMBO Journal*, *29*(21), 3660–3672. https://doi.org/10.1038/emboj.2010.235

Katz, Y., Wang, E. T., Airoldi, E. M., & Burge, C. B. (2010). Analysis and design of RNA sequencing experiments for identifying isoform regulation. *Nature Methods*, *7*(12), 1009–1015. https://doi.org/10.1038/nmeth.1528

Kentsis, A., Reed, C., Rice, K. L., Sanda, T., Rodig, S. J., Tholouli, E., Christie, A., Valk, P. J. M., Delwel, R., Ngo, V., Kutok, J. L., Dahlberg, S. E., Moreau, L. A., Byers, R. J., Christensen, J. G., Woude, G. Vande, Licht, J. D., Kung, A. L., Staudt, L. M., & Look, A. T. (2012). Autocrine activation of the MET receptor tyrosine kinase in acute myeloid leukemia. *Nature Medicine*, *18*(7), 1118–1122. https://doi.org/10.1038/nm.2819

Klempnauer, K. H., & Bishop, J. M. (1984). Neoplastic transformation by E26 leukemia virus is mediated by a single protein containing domains of gag and myb genes. *Journal of Virology*, *50*(1), 280–283. https://doi.org/10.1128/jvi.50.1.280-283.1984

Kolde, R. (2020). *Raivokolde/pheatmap* [R]. https://github.com/raivokolde/pheatmap (Original work published 2012)

Krivtsov, A. V., Evans, K., Gadrey, J. Y., Eschle, B. K., Hatton, C., Uckelmann, H. J., Ross, K. N., Perner, F., Olsen, S. N., Pritchard, T., McDermott, L., Jones, C. D., Jing, D., Braytee, A., Chacon, D., Earley, E., McKeever, B. M., Claremon, D., Gifford, A. J., … Armstrong, S. A. (2019). A Menin-MLL Inhibitor Induces Specific Chromatin Changes and Eradicates Disease in Models of MLL-Rearranged Leukemia. *Cancer Cell*, *36*(6), 660-673.e11. https://doi.org/10.1016/j.ccell.2019.11.001

Langmead, B., Trapnell, C., Pop, M., & Salzberg, S. L. (2009). Ultrafast and memory-efficient alignment of short DNA sequences to the human genome. *Genome Biology*, *10*(3), R25. https://doi.org/10.1186/gb-2009-10-3-r25

Lasko, L. M., Jakob, C. G., Edalji, R. P., Qiu, W., Montgomery, D., Digiammarino, E. L., Hansen, T. M., Risi, R. M., Frey, R., Manaves, V., Shaw, B., Algire, M., Hessler, P., Lam, L. T., Uziel, T., Faivre, E., Ferguson, D., Buchanan, F. G., Martin, R. L., … Bromberg, K. D. (2017). Discovery of a selective catalytic p300/CBP inhibitor that targets lineage-specific tumours. *Nature*, *550*(7674), 128–132. https://doi.org/10.1038/nature24028

Lei, W., Rushton, J. J., Davis, L. M., Liu, F., & Ness, S. A. (2004). Positive and negative determinants of target gene specificity Myb transcription factors. *Journal of Biological Chemistry*, *279*(28), 29519–29527. https://doi.org/10.1074/jbc.M403133200

Li, B., & Dewey, C. N. (2011). RSEM: Accurate transcript quantification from RNA-Seq data with or without a reference genome. *BMC Bioinformatics*, *12*(1), 323. https://doi.org/10.1186/1471-2105-12-323

Li, W., Xu, H., Xiao, T., Cong, L., Love, M. I., Zhang, F., Irizarry, R. A., Liu, J. S., Brown, M., & Liu, X. S. (2014). MAGeCK enables robust identification of essential genes from genome-scale CRISPR/Cas9 knockout screens. *Genome Biology*, *15*(12), 554. https://doi.org/10.1186/s13059-014-0554-4

Look, A. T. (1997). Oncogenic Transcription Factors in the Human Acute Leukemias. *Science*, *278*(5340), 1059–1064. https://doi.org/10.1126/science.278.5340.1059

Lu, B., Klingbeil, O., Tarumoto, Y., Somerville, T. D. D., Huang, Y.-H., Wei, Y., Wai, D. C., Low, J. K. K., Milazzo, J. P., Wu, X. S., Cao, Z., Yan, X., Demerdash, O. E., Huang, G., Mackay, J. P., Kinney, J. B., Shi, J., & Vakoc, C. R. (2018). A Transcription Factor Addiction in Leukemia

Imposed by the MLL Promoter Sequence. *Cancer Cell*, *34*(6), 970-981.e8. https://doi.org/10.1016/j.ccell.2018.10.015

Luger, S. M., O'Brien, S. G., Ratajczak, J., Ratajczak, M. Z., Mick, R., Stadtmauer, E. A., Nowell, P. C., Goldman, J. M., & Gewirtz, A. M. (2002). Oligodeoxynucleotide-mediated inhibition of c-myb gene expression in autografted bone marrow: A pilot study. *Blood*, *99*(4), 1150–1158. https://doi.org/10.1182/blood.v99.4.1150

Mansour, M. R., Abraham, B. J., Anders, L., Gutierrez, A., Durbin, A. D., Lawton, L., Sallan, S. E., Silverman, L. B., Loh, M. L., Hunger, S. P., Sanda, T., Richard, A., Berezovskaya, A., Gutierrez, A., Durbin, A. D., Etchin, J., Lawton, L., Sallan, S. E., Silverman, L. B., … Look, A. T. (2014). An oncogenic super-enhancer formed through somatic mutation of a noncoding intergenic element. In *Science* (Vol. 346, Issue 6215). https://doi.org/10.1126/science.1259037

Meng, Y.-S., Khoury, H., Dick, J. E., & Minden, M. D. (2005). Oncogenic potential of the transcription factor LYL1 in acute myeloblastic leukemia. *Leukemia*, *19*(11), 1941–1947. https://doi.org/10.1038/sj.leu.2403836

Meyer, L. R., Zweig, A. S., Hinrichs, A. S., Karolchik, D., Kuhn, R. M., Wong, M., Sloan, C. A., Rosenbloom, K. R., Roe, G., Rhead, B., Raney, B. J., Pohl, A., Malladi, V. S., Li, C. H., Lee, B. T., Learned, K., Kirkup, V., Hsu, F., Heitner, S., … Kent, W. J. (2013). The UCSC Genome Browser database: Extensions and updates 2013. *Nucleic Acids Research*, *41*(D1), D64–D69. https://doi.org/10.1093/nar/gks1048

Ogiwara, H., Sasaki, M., Mitachi, T., Oike, T., Higuchi, S., Tominaga, Y., & Kohno, T. (2016). Targeting p300 Addiction in CBP-Deficient Cancers Causes Synthetic Lethality by Apoptotic Cell Death due to Abrogation of MYC Expression. *Cancer Discovery*, *6*(4), 430–445. https://doi.org/10.1158/2159-8290.CD-15-0754

Oughtred, R., Stark, C., Breitkreutz, B.-J., Rust, J., Boucher, L., Chang, C., Kolas, N., O'Donnell, L., Leung, G., McAdam, R., Zhang, F., Dolma, S., Willems, A., Coulombe-Huntington, J., Chatr-aryamontri, A., Dolinski, K., & Tyers, M. (2019). The BioGRID interaction database: 2019 update. *Nucleic Acids Research*, *47*(D1), D529–D541. https://doi.org/10.1093/nar/gky1079

Pattabiraman, D R, & Gonda, T. J. (2013). Role and potential for therapeutic targeting of MYB in leukemia. *Leukemia*, *27*(2), 269–277. https://doi.org/10.1038/leu.2012.225

Pattabiraman, Diwakar R., McGirr, C., Shakhbazov, K., Barbier, V., Krishnan, K., Mukhopadhyay, P., Hawthorne, P., Trezise, A., Ding, J., Grimmond, S. M., Papathanasiou, P., Alexander, W. S., Perkins, A. C., Levesque, J. P., Winkler, I. G., & Gonda, T. J. (2014). Interaction of c-Myb with p300 is required for the induction of acute myeloid leukemia (AML) by human AML oncogenes. *Blood*, *123*(17), 2682–2690. https://doi.org/10.1182/blood-2012-02-413187

Radhakrishnan, I., Radhakrishnan, I., Perez-alvarado, G. C., Perez-alvarado, G. C., Parker, D., Parker, D., Dyson, H. J., Dyson, H. J., Montminy, M. R., Montminy, M. R., Wright, P. E., & Wright, P. E. (1997). Solution structure of the KIX domain of CBP bound to the transactivation domain of CREB: a model for activator:coactivator interactions. *Cell*, *91*, 741–752.

Ramaswamy, K., Forbes, L., Minuesa, G., Gindin, T., Brown, F., Kharas, M. G., Krivtsov, A. V., Armstrong, S. A., Still, E., de Stanchina, E., Knoechel, B., Koche, R., & Kentsis, A. (2018).

Peptidomimetic blockade of MYB in acute myeloid leukemia. *Nature Communications*, *9*(1), 110–110. https://doi.org/10.1038/s41467-017-02618-6

Robinson, M. D., & Oshlack, A. (2010). A scaling normalization method for differential expression analysis of RNA-seq data. *Genome Biology*, *11*(3), R25. https://doi.org/10.1186/gb-2010-11-3-r25

Roe, J.-S., Mercan, F., Rivera, K., Pappin, D. J., & Vakoc, C. R. (2015). BET Bromodomain Inhibition Suppresses the Function of Hematopoietic Transcription Factors in Acute Myeloid Leukemia. *Molecular Cell*, *58*(6), 1028–1039. https://doi.org/10.1016/j.molcel.2015.04.011

Sanda, T., Lawton, L. N., Barrasa, M. I., Fan, Z. P., Kohlhammer, H., Gutierrez, A., Ma, W., Tatarek, J., Ahn, Y., Kelliher, M. A., Jamieson, C. H. M., Staudt, L. M., Young, R. A., & Look, A. T. (2012). Core Transcriptional Regulatory Circuit Controlled by the TAL1 Complex in Human T Cell Acute Lymphoblastic Leukemia. *Cancer Cell*, *22*(2), 209–221. https://doi.org/10.1016/j.ccr.2012.06.007

Sanda, T., Tyner, J. W., Gutierrez, A., Ngo, V. N., Glover, J., Chang, B. H., Yost, A., Ma, W., Fleischman, A. G., Zhou, W., Yang, Y., Kleppe, M., Ahn, Y., Tatarek, J., Kelliher, M. A., Neuberg, D. S., Levine, R. L., Moriggl, R., Müller, M., … Look, A. T. (2013). TYK2–STAT1–BCL2 Pathway Dependence in T-cell Acute Lymphoblastic Leukemia. *Cancer Discovery*, *3*(5), 564–577. https://doi.org/10.1158/2159-8290.CD-12-0504

Sanjana, N. E., Shalem, O., & Zhang, F. (2014). Improved vectors and genome-wide libraries for CRISPR screening. *Nature Methods*, *11*(8), 783–784. https://doi.org/10.1038/nmeth.3047

Selvakumaran, M., Liebermann, D. A., & Hoffman-Liebermann, B. (1992). Deregulated c-myb disrupts interleukin-6- or leukemia inhibitory factor-induced myeloid differentiation prior to c-myc: Role in leukemogenesis. *Molecular and Cellular Biology*, *12*(6), 2493–2500. https://doi.org/10.1128/MCB.12.6.2493

Suzuki, K., Suzuki, Y., Hama, A., Muramatsu, H., Nakatochi, M., Gunji, M., Ichikawa, D., Hamada, M., Taniguchi, R., Kataoka, S., Murakami, N., Kojima, D., Sekiya, Y., Nishikawa, E., Kawashima, N., Narita, A., Nishio, N., Nakazawa, Y., Iwafuchi, H., … Okuno, Y. (2017). Recurrent MYB rearrangement in blastic plasmacytoid dendritic cell neoplasm. *Leukemia*, *31*(7), 1629–1633. https://doi.org/10.1038/leu.2017.101

Tarumoto, Y., Lin, S., Wang, J., Milazzo, J. P., Xu, Y., Lu, B., Yang, Z., Wei, Y., Polyanskaya, S., Wunderlich, M., Gray, N. S., Stegmaier, K., & Vakoc, C. R. (2020). Salt-inducible kinase inhibition suppresses acute myeloid leukemia progression in vivo. *Blood*, *135*(1), 56–70. https://doi.org/10.1182/blood.2019001576

Tarumoto, Y., Lu, B., Somerville, T. D. D., Huang, Y.-H., Milazzo, J. P., Wu, X. S., Klingbeil, O., El Demerdash, O., Shi, J., & Vakoc, C. R. (2018). LKB1, Salt-Inducible Kinases, and MEF2C Are Linked Dependencies in Acute Myeloid Leukemia. *Molecular Cell*, *69*(6), 1017-1027.e6. https://doi.org/10.1016/j.molcel.2018.02.011

Trapnell, C., Pachter, L., & Salzberg, S. L. (2009). TopHat: Discovering splice junctions with RNA-Seq. *Bioinformatics*, *25*(9), 1105–1111. https://doi.org/10.1093/bioinformatics/btp120

Tsherniak, A., Vazquez, F., Montgomery, P. G., Weir, B. A., Kryukov, G., Cowley, G. S., Gill, S., Harrington, W. F., Pantel, S., Krill-Burger, J. M., Meyers, R. M., Ali, L., Goodale, A., Lee, Y., Jiang, G., Hsiao, J., Gerath, W. F. J., Howell, S., Merkel, E., … Hahn, W. C. (2017). Defining a Cancer Dependency Map. *Cell*, *170*(3), 564-576.e16. https://doi.org/10.1016/j.cell.2017.06.010

Tyner, J. W., Tognon, C. E., Bottomly, D., Wilmot, B., Kurtz, S. E., Savage, S. L., Long, N., Schultz, A. R., Traer, E., Abel, M., Agarwal, A., Blucher, A., Borate, U., Bryant, J., Burke, R., Carlos, A., Carpenter, R., Carroll, J., Chang, B. H., … Druker, B. J. (2018). Functional genomic landscape of acute myeloid leukaemia. *Nature*, *562*(7728), 526–531. https://doi.org/10.1038/s41586-018-0623-z

Uttarkar, S., Dassé, E., Coulibaly, A., Steinmann, S., Jakobs, A., Schomburg, C., Trentmann, A., Jose, J., Schlenke, P., Berdel, W. E., Schmidt, T. J., Müller-Tidow, C., Frampton, J., & Klempnauer, K. H. (2016). Targeting acute myeloid leukemia with a small molecule inhibitor of the Myb/p300 interaction. *Blood*. https://doi.org/10.1182/blood-2015-09-668632

Uttarkar, S., Dukare, S., Bopp, B., Goblirsch, M., Jose, J., & Klempnauer, K. H. (2015). Naphthol AS-E phosphate inhibits the activity of the transcription factor Myb by blocking the interaction with the KIX domain of the coactivator p300. *Molecular Cancer Therapeutics*. https://doi.org/10.1158/1535-7163.MCT-14-0662

Vakoc, C. R., & Kentsis, A. (2018). Disabling an oncogenic transcription factor by targeting of control kinases. *Oncotarget*, *9*(64). https://doi.org/10.18632/oncotarget.25971

Wang, L., Gural, A., Sun, X.-J., Zhao, X., Perna, F., Huang, G., Hatlen, M. A., Vu, L., Liu, F., Xu, H., Asai, T., Xu, H., Deblasio, T., Menendez, S., Voza, F., Jiang, Y., Cole, P. A., Zhang, J., Melnick, A., … Nimer, S. D. (2011). The Leukemogenicity of AML1-ETO Is Dependent on Site-Specific Lysine Acetylation. *Science*, *333*(6043), 765–769. https://doi.org/10.1126/science.1201662

Wickham, H. (2016). *ggplot2: Elegant Graphics for Data Analysis* (2nd ed.). Springer International Publishing. https://doi.org/10.1007/978-3-319-24277-4

Wickham, H., François, R., Henry, L., Müller, K., & RStudio. (2020). *dplyr: A Grammar of Data Manipulation* (1.0.2) [Computer software]. https://CRAN.R-project.org/package=dplyr

Xu, Yali, Milazzo, J. P., Somerville, T. D. D., Tarumoto, Y., Huang, Y.-H., Ostrander, E. L., Wilkinson, J. E., Challen, G. A., & Vakoc, C. R. (2018). A TFIID-SAGA Perturbation that Targets MYB and Suppresses Acute Myeloid Leukemia. *Cancer Cell*, *33*(1), 13-28.e8. https://doi.org/10.1016/j.ccell.2017.12.002

Xu, Ye, Man, N., Karl, D., Martinez, C., Liu, F., Sun, J., Martinez, C. J., Martin, G. M., Beckedorff, F., Lai, F., Yue, J., Roisman, A., Greenblatt, S., Duffort, S., Wang, L., Sun, X., Figueroa, M., Shiekhattar, R., & Nimer, S. (2019). TAF1 plays a critical role in AML1-ETO driven leukemogenesis. *Nature Communications*, *10*(1), 4925. https://doi.org/10.1038/s41467-019-12735-z

Zhao, L., Glazov, E. A., Pattabiraman, D. R., Al-Owaidi, F., Zhang, P., Brown, M. A., Leo, P. J., & Gonda, T. J. (2011). Integrated genome-wide chromatin occupancy and expression analyses

identify key myeloid pro-differentiation transcription factors repressed by Myb. *Nucleic Acids Research*, *39*(11), 4664–4679. https://doi.org/10.1093/nar/gkr024

Zor, T., De Guzman, R. N., Dyson, H. J., & Wright, P. E. (2004). Solution Structure of the KIX Domain of CBP Bound to the Transactivation Domain of c-Myb. *Journal of Molecular Biology*, *337*(3), 521–534. https://doi.org/10.1016/j.jmb.2004.01.038

SUPPLEMENTAL DATA

Supplemental Figures

Supplemental Figure Legends

Source Data File Legends

Supplementary File Legends

Lists of Supplemental Data deposited in Zenodo (https://doi.org/10.5281/zenodo.4321824)

Key Resource Table

SUPPLEMENTAL FIGURES

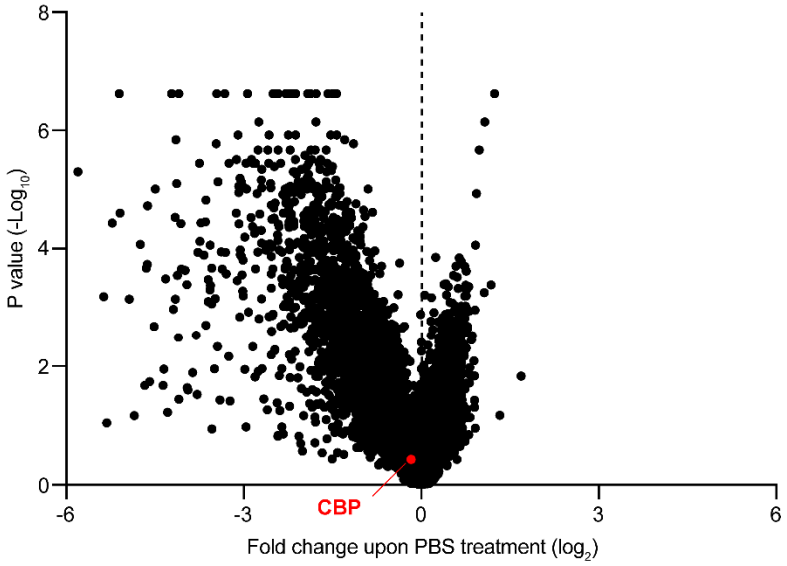

Figure 1-figure supplement 1. CBP depletion is dispensable in AML cells. Volcano plot showing the relative abundance of MOLM13-Cas9 cell clones expressing sgRNAs targeting specific genes (fold change of PBS-treated cells at T1 versus T0) and their statistical significance from biological replicates. Dashed line represents no enrichment, with positive values representing genes whose depletion confers relative resistance to MYBMIM.

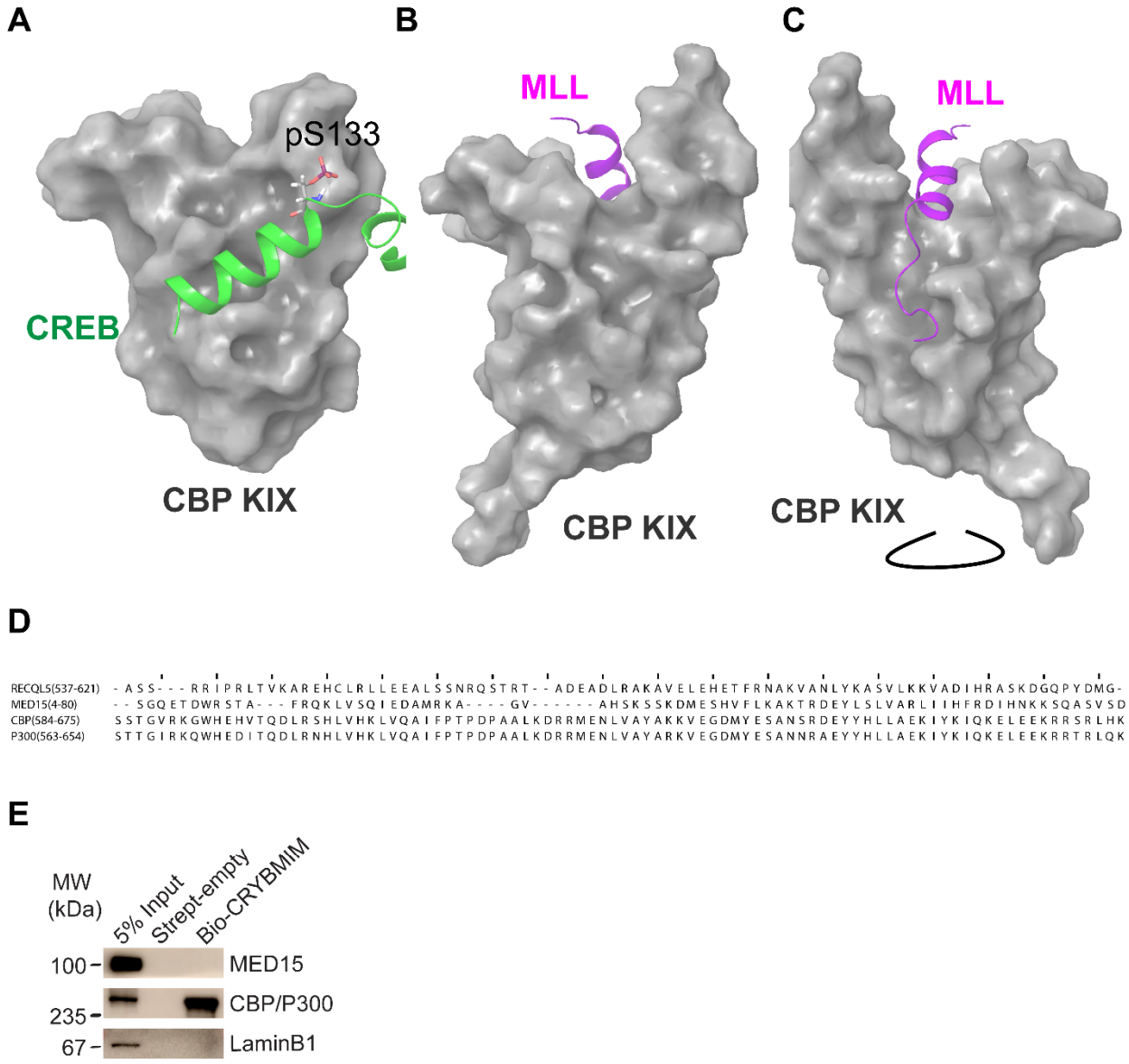

Figure 2-figure-supplement 1. Molecular models of CREB and MLL structures in complex with CBP KIX, and CRYBMIM selectively binds to KIX domain in CBP/P300. (A) Molecular model of the CREB:KIX complex assembled in Maestro (Schrödinger) using PDB 1KDX showing phosphor-Serine 133. **(B)** Molecular model of the MLL:KIX complex assembled in Maestro (Schrödinger) using PDB 2LXS shown from the MYB/CREB binding site on KIX. **(C)** Molecular model of the MLL:KIX complex assembled in Maestro (Schrödinger) using PDB 2LXS rotated to show the full MLL peptide. **(D)** Sequence alignment of KIX domains in different human proteins. Identity/similarity of each set of sequences were 88%/96% (CBP vs P300), 21%/38% (CBP vs MED15) and 17%/34% (CBP vs RECQL5). **(E)** Western blots following affinity purification of MV411 nuclear extracts, showing specific binding of CBP/P300 but not MED15 to biotinylated CRYBMIM (Bio-CRYBMIM), immobilized on streptavidin beads. Purification with beads alone (Strept-empty) and LaminB1 serve as specificity controls.

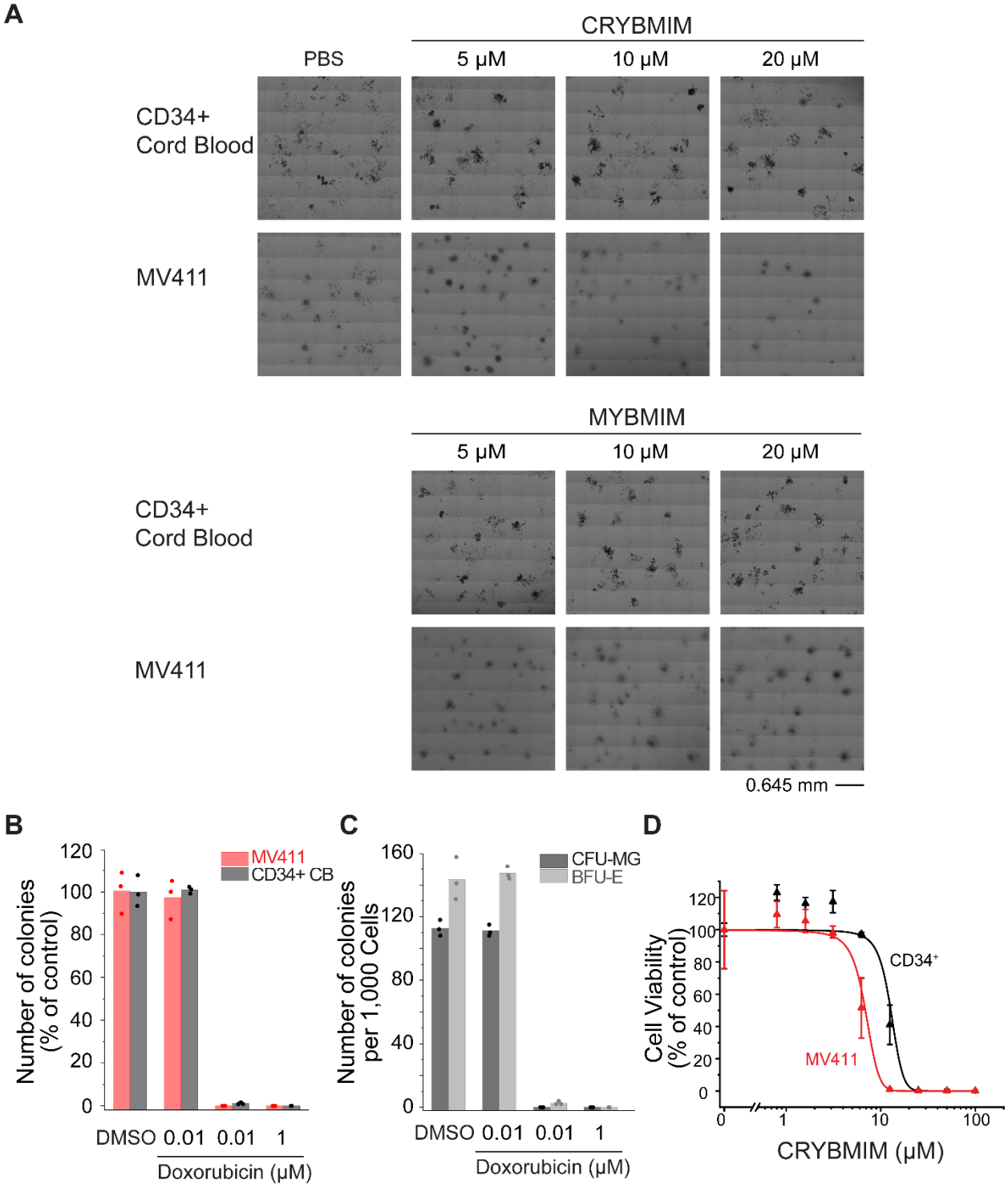

Figure 3-figure supplement 1. CRYBMIM relatively spares normal hematopoietic progenitor cells in vitro. (A) Phase contrast photographs of MV411 and CD34+ cells isolated from human umbilical cord blood (CD34+ CB) and cultured in MethoCult H3040 with drug treatment, as indicated. **(B)** Colony forming ability of MV411 and CD34+ CB cells cultured in MethoCult H3040 following doxorubicin treatment. **(C)** Formation of BFU-E (light gray) and CFU-GM (gray) colonies of CD34+ CB cells cultured in MethoCult H3040 upon doxorubicin treatment. **(D)** Growth of MV411 and CD34+ CB cells upon CRYBMIM treatment in serum-containing suspension culture (IC50 = 6.9 ± 3.4 vs 13 ± 3.6 mM, p = 1.1e-15, ANOVA).

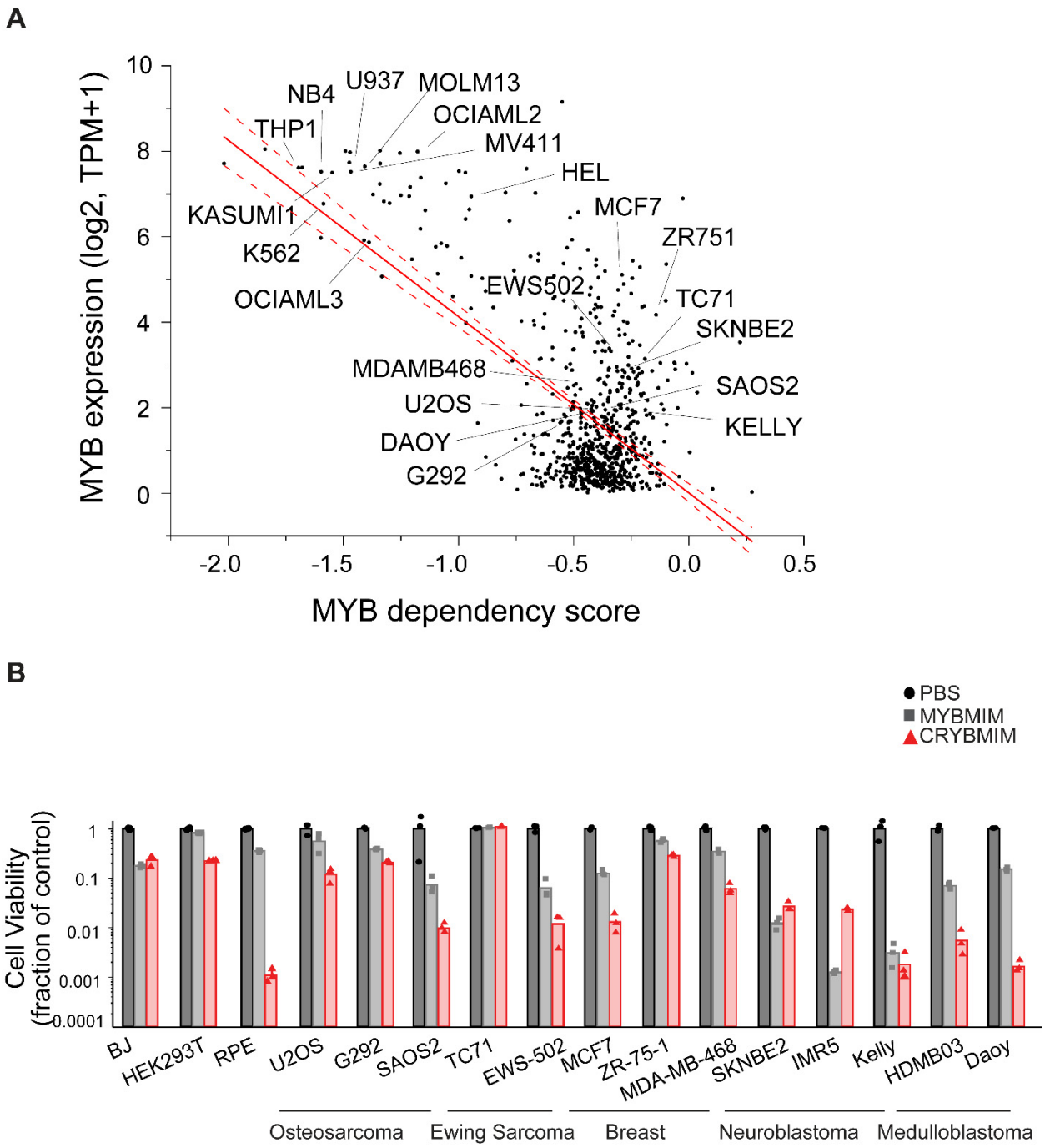

Figure 3-figure supplement 2. Activity of CRYBMIM on non-hematopoietic cells. (A) Expression of MYB as a function of its genetic dependency in tumor cell lines, as assessed by DepMap. Red line represents linear correlation, with dashed lines showing 95% confidence intervals. **(B)** Cell viability assays of non-leukemia tumor and non-tumor cell lines treated with control PBS (black), 20 μM MYBMIM (gray), or 20 μM CRYBMIM (red) as indicated for 6 days with media replacement every 48 hours in three biological replicates.

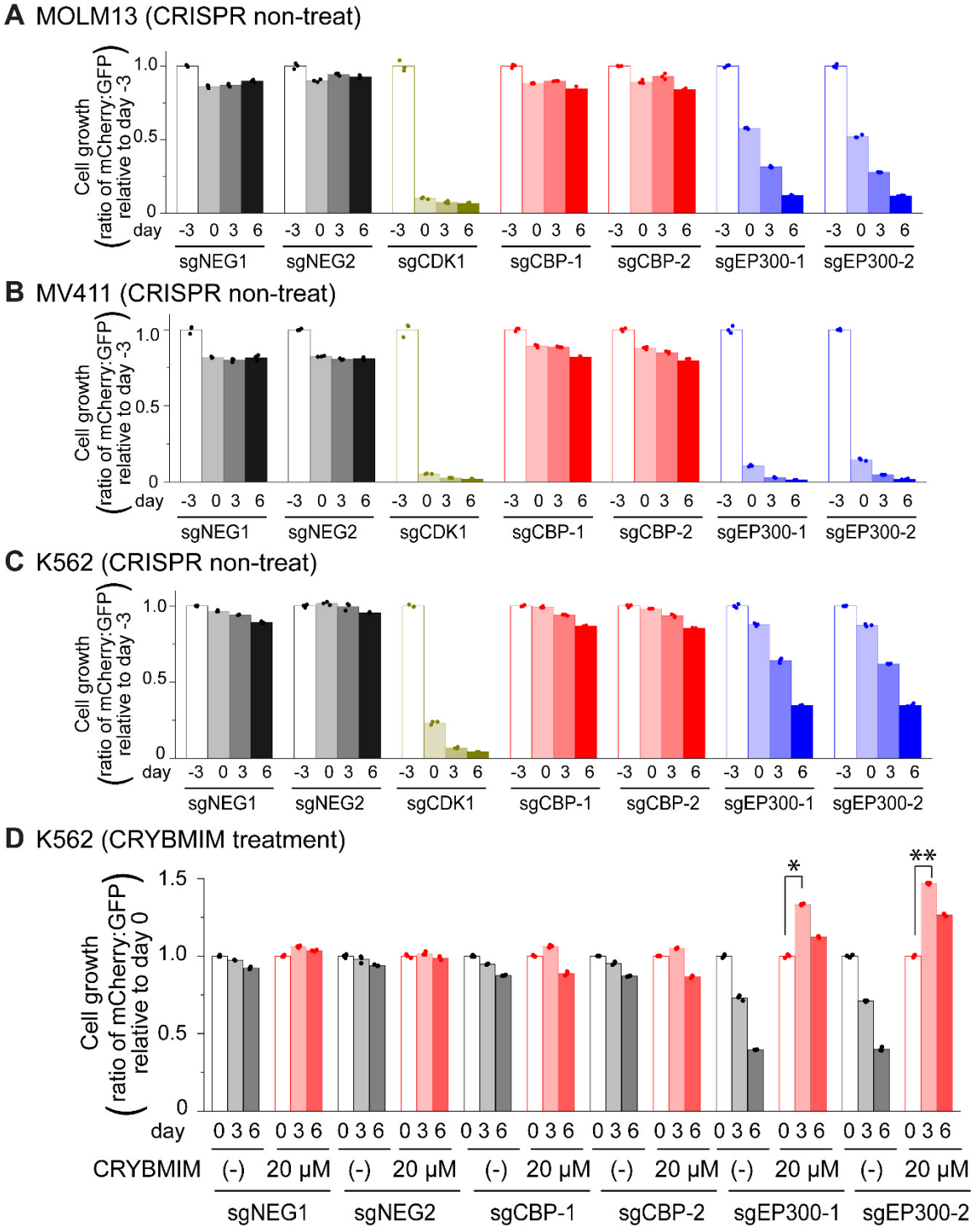

Figure 4-figure supplement 1. Genetic dependencies of CRYBMIM susceptibility in AML cells. (A-C) Relative growth of GFP-expressing MOLM13 (A), MV411 (B), and K562 (C) cells expressing mCherry and unique sgRNAs targeting negative control AAVS1 (sgNEG1 and sgNEG2), positive control CDK1 (sgCDK1), CBP (sgCBP-1 and sgCBP-2), and P300 (sgEP300-1 and sgEP300-2) and quantified by FACS on days –3, 0, 3, and 6 upon sgRNA transduction. **(D)** Relative growth of K562-Cas9 cells expressing specific sgRNAs upon treatment with 20 μM CRYBMIM for two days (*p = 1.0e-6, **p = 1.3e-7; t-test for day 3 versus day 0).

A

One hour

Lost MYB peaks

Rank	Motif	P-value	log P-pvalue	% of Targets	% of Background	STD(Bg STD)	Best Match/Details
1	AACCGTTA	1e-32	-7.510e+01	52.50%	9.24%	332.1bp (335.2bp)	BMYB(HTH)/Hela-BMYB-ChIP-Seq(GSE27030)/Homer(0.927)
2 *	AACCGACA	1e-7	-1.700e+01	46.67%	23.85%	534.5bp (519.5bp)	bHLH110(bHLH)/colamp-bHLH110-DAP-Seq(GSE60143)/Homer(0.919)
3 *	CAGTTCCT	1e-6	-1.474e+01	55.00%	32.68%	687.7bp (322.1bp)	PU.1(ETS)/ThioMac-PU.1-ChIP-Se (GSE21512)/Homer(0.851)
4 *	TTCGTTTC	1e-6	-1.400e+01	12.50%	2.67%	650.5bp (340.1bp)	T1ISRE(IRF)/ThioMac-Ifnb-Expression/Homer(0.810)

Gained MYB peaks

Rank	Motif	P-value	log P-pvalue	% of Targets	% of Background	STD(Bg STD)	Best Match/Details
1	GTGACTCA	1e-18	-4.195e+01	23.36%	7.45%	711.5bp (404.5bp)	AP-1(bZIP)/ThioMac-PU.1-ChIP-Seq(GSE21512)/Homer(0.894)
2 *	TTGCGGTT	1e-10	-2.437e+01	25.55%	12.03%	571.1bp (484.0bp)	RUNX2/MA0511.2/Jaspar(0.949)
3 *	AGAGGAAG	1e-8	-1.935e+01	32.40%	18.76%	561.5bp (475.6bp)	SPIB/MA0081.1/Jaspar(0.873)
4 *	CGATTGCC	1e-6	-1.605e+01	28.33%	16.62%	593.4bp (522.8bp)	NFY(CCAAT)/Promoter/Homer(0.914)
5 *	TTGCAAGA	1e-6	-1.530e+01	27.10%	15.88%	555.4bp (440.4bp)	CEBP-AP1(bZIP)/ThioMac-CEBPb-ChIP-Seq(GSE21512)/Homer(0.890)
6 *	CAGCTGTC	1e-5	-1.362e+01	66.36%	53.22%	697.6bp (474.6bp)	Myog/MA0500.1/Jaspar(0.934)
7 *	TGCCATGG	1e-4	-1.095e+01	26.17%	16.87%	591.2bp (470.5bp)	Rfx1(HTH)/NPC-H3K4me1-ChIP-Seq(GSE16256)/Homer(0.780)
8 *	ACGAGTGA	1e-4	-9.771e+00	18.69%	11.23%	669.5bp (399.4bp)	At5g04390(C2H2)/col200-At5g04390-DAP-Seq(GSE60143)/Homer(0.822)
9 *	GCGTCGAA	1e-3	-7.159e+00	5.12%	0.90%	248.1bp (583.3bp)	OP11/Literature(Harbison)/Yeast(0.701)
10 *	GGTCCGCC	1e-1	-4.294e+00	30.84%	25.24%	559.6bp (686.6bp)	Sp5(Zf)/mES-Sp5.Flag-ChIP-Seq(GSE72989)/Homer(0.807)
11 *	GCTGGTCG	1e-1	-3.857e+00	4.36%	2.35%	505.6bp (680.1bp)	ACE2/ACE2_YPD/2-SW15(Harbison)/Yeast(0.840)
12 *	TGAGTTAA	1e0	-6.503e-01	9.35%	9.32%	453.4bp (413.2bp)	ZCRB1(RRM)/Homo_sapiens-RNCMPT00087-PBM/HughesRNA(0.814)
13 *	GTACAGGT	1e0	-3.934e-02	0.93%	2.06%	307.4bp (428.8bp)	ZEB1(Zf)/PDAC-ZEB1-ChIP-Seq(GSE64557)/Homer(0.770)

* possible false positive

B

Four hour

Lost MYB peaks

Rank	Motif	P-value	log P-pvalue	% of Targets	% of Background	STD(Bg STD)	Best Match/Details
1	GACAGTTG	1e-149	-3.454e+02	55.95%	31.63%	709.7bp (502.7bp)	MYB77(MYB)col-MYB77-DAP-Seq(GSE60143)/Homer(0.918)
2	GCCAATCG	1e-67	-1.566e+02	27.30%	14.36%	683.7bp (686.8bp)	NFY(CCAAT)/Promoter/Homer(0.923)
3	CGGAAACG	1e-62	-1.445e+02	35.01%	21.03%	723.1bp (689.9bp)	Fli1(ETS)/CD8-FLI-ChIP-Seq(GSE20898)/Homer(0.910)
4	TGCGCGTTA	1e-59	-1.361e+02	25.31%	13.57%	676.0bp (658.0bp)	AT3G10030(Trihelix)/colamp-AT3G10030-DAP-Seq(GSE60143)/Homer(0.808)
5	CGTCACGT	1e-44	-1.035e+02	18.41%	9.54%	727.5bp (692.8bp)	CBF1(MacIsaac)/Yeast(0.874)
6	GCCCCGCC	1e-34	-7.921e+01	45.00%	33.59%	626.8bp (808.8bp)	Sp1(Zf)/Promoter/Homer(0.890)
7	TGTTGCAA	1e-30	-7.101e+01	19.54%	11.77%	911.0bp (413.8bp)	CEBP:AP1(bZIP)/ThioMac-CEBPb-ChIP-Seq(GSE21512)/Homer(0.956)
8	CGCCATTT	1e-29	-6.827e+01	15.72%	8.90%	783.8bp (645.1bp)	YY2/MA0748.1/Jaspar(0.850)
9	CTCGCGCG	1e-23	-5.385e+01	31.12%	22.72%	696.8bp (816.3bp)	TARK(RRM,Znf)/Drosophila_melanogaster-RNCMPT00035-PBM/HughesRNA(0.931)
10	CTGTGGTT	1e-22	-5.175e+01	20.57%	13.67%	851.3bp (457.7bp)	RUNX1(Runt)/Jurkat-RUNX1-ChIP-Seq(GSE29180)/Homer(0.971)
11	AACGTTCG	1e-19	-4.501e+01	38.17%	29.94%	686.3bp (703.1bp)	Lm_0254(RRM)/Leishmania_major-RNCMPT00254-PBM/HughesRNA(0.802)
12	GACCGGAC	1e-15	-3.614e+01	44.49%	36.86%	761.1bp (787.5bp)	CAT8/MA0280.1/Jaspar(0.791)
13 *	GCCGCCGC	1e-11	-2.748e+01	34.31%	28.13%	612.3bp (835.5bp)	ERF094/MA1049.1/Jaspar(0.888)
14 *	TAACCCTA	1e-3	-8.086e+00	2.06%	1.25%	495.8bp (468.0bp)	MUB(KH)/Drosophila_melanogaster-RNCMPT00137-PBM/HughesRNA(0.891)

Gained MYB peaks

Rank	Motif	P-value	log P-pvalue	% of Targets	% of Background	STD(Bg STD)	Best Match/Details
1	GTGAGTCA	1e-124	-2.875e+02	40.69%	10.49%	294.9bp (230.9bp)	GCN4/GCN4_SM/121-GCN4(Harbison)/Yeast(0.965)
2	CACTTCCT	1e-67	-1.563e+02	63.64%	35.29%	326.1bp (232.4bp)	PU.1(ETS)/ThioMac-PU.1-ChIP-Seq(GSE21512)/Homer(0.948)
3	AACCGGAA	1e-26	-6.129e+01	60.61%	42.91%	330.9bp (236.3bp)	ETV2/MA0762.1/Jaspar(0.806)
4	TGTGGTTT	1e-22	-5.202e+01	35.82%	21.56%	317.4bp (225.7bp)	RUNX1(Runt)/Jurkat-RUNX1-ChIP-Seq(GSE29180)/Homer(0.969)
5	TTGCGTAA	1e-18	-4.374e+01	31.39%	18.93%	432.0bp (229.6bp)	CEBPB/MA0466.2/Jaspar(0.918)
6	AGTGACTT	1e-16	-3.745e+01	24.68%	14.29%	379.6bp (230.5bp)	STZ(C2H2)/colamp-STZ-DAP-Seq(GSE60143)/Homer(0.788)
7 *	CCCCGTAG	1e-6	-1.465e+01	11.69%	7.13%	307.8bp (237.9bp)	RPH1/Literature(Harbison)/Yeast(0.724)
8 *	CCCCGCAG	1e-6	-1.464e+01	4.98%	2.19%	395.5bp (255.1bp)	gcm2/MA0917.1/Jaspar(0.733)
9 *	AGCGTCGC	1e-5	-1.264e+01	9.09%	5.39%	363.4bp (259.0bp)	Rbm4_N(RRM)/Danio_rerio-RNCMPT00248-PBM/HughesRNA(0.798)
10 *	CGTGTGAT	1e-5	-1.165e+01	11.26%	7.28%	645.5bp (244.4bp)	CMTA3/MA0970.1/Jaspar(0.797)
11 *	AACCTCTA	1e-4	-1.027e+01	10.28%	6.73%	346.2bp (227.8bp)	RPI11/MA0372.1/Jaspar(0.696)
12 *	GAGGGATT	1e-4	-9.924e+00	6.82%	4.03%	286.4bp (229.1bp)	PH0137.1 Pitx1/Jaspar(0.778)
13 *	GCCGTTAC	1e-3	-7.136e+00	5.74%	3.61%	332.4bp (237.2bp)	MYB98(MYB)/col-MYB98-DAP-Seq(GSE60143)/Homer(0.877)
14 *	GCCCTGCG	1e-2	-5.775e+00	2.71%	1.47%	776.4bp (245.6bp)	Vts1p(SAM)/Saccharomyces_cerevisiae-RNCMPT00111-PBM/HughesRNA(0.779)
15 *	GTCGGGAT	1e-1	-4.352e+00	0.76%	0.27%	755.6bp (240.5bp)	ARF3/MA1009.1/Jaspar(0.759)
16 *	GGACGGGT	1e-1	-2.761e+00	0.97%	0.54%	589.8bp (238.8bp)	FXR2(KH)/Homo_sapiens-RNCMPT00026-PBM/HughesRNA(0.831)
17 *	GATATCAC	1e0	-2.169e+00	1.95%	1.42%	591.0bp (222.8bp)	Optix/dmmpmm(Noyes_2d)/fly(0.822)

* possible false positive

Figure 6-figure supplement 1. CRYBMIM remodels MYB chromatin occupancies in AML cells. (A-B) Full lists of sequence motifs found in CRYBMIM-induced MYB-depleted (left) and MYB-enriched loci (right) after one hour treatment (A) and four hour treatment (B) of 20 μM CRYBMIM are shown.

```
CBP_HUMAN        375 GEVRACSLPHCRTMKNVLNHMTHCQAGKACQVAHCASSRQIISHWKNCTR    424
                     ||||.|:||||||||||||||||||:||:||||||||||||||||||||
EP300_HUMAN      359 GEVRQCNLPHCRTMKNVLNHMTHCQSGKSCQVAHCASSRQIISHWKNCTR    408

CBP_HUMAN        425 HDCPVCLPLKNASDKRNQQTILGSPASGIQNTIGSVGTGQQNATSLSNPN    474
                     ||||||||||||.||||||.||.....|:.|. .|:|.|||:|.:||..:
EP300_HUMAN      409 HDCPVCLPLKNAGDKRNQQPILTGAPVGLGNP-SSLGVGQQSAPNLSTVS    457

CBP_HUMAN       1487 HPPDQKIPKPKRLQEWYKKMLDKAFAERIIHDYKDIFKQATEDRLTSAKE   1536
                     ||||||||||||||||||||||||.:|||:||||||||||||||||||||
EP300_HUMAN     1451 HPPDQKIPKPKRLQEWYKKMLDKAVSERIVHDYKDIFKQATEDRLTSAKE   1500

CBP_HUMAN       1628 HKEVFFVIHLHAGPVINTLPPIVDPDPLLSCDLMDGRDAFLTLARDKHWE   1677
                     ||||||||.|.|||..|:||||||||||:.||||||||||||||||||.|
EP300_HUMAN     1591 HKEVFFVIRLIAGPAANSLPPIVDPDPLIPCDLMDGRDAFLTLARDKHLE   1640

CBP_HUMAN       1828 YHAKHCQENKCPVPFCLNIKHKLRQQQIQHRLQQAQLMRRRMATMNTRNV   1877
                     ||||||||||||||||||||.||||||:||||||||::|||||:|....|
EP300_HUMAN     1791 YHAKHCQENKCPVPFCLNIKQKLRQQQLQHRLQQAQMLRRRMASMQRTGV   1840
```

Figure 7-figure supplement 1. CBP is the primary binding partner of MYB in AML cells. Sequence alignment of relevant CBP (top row) and P300 (bottom row) amino acids. Highlighted peptides identified in mass spectrometry analysis aligned to either CBP only (green) or both CBP and

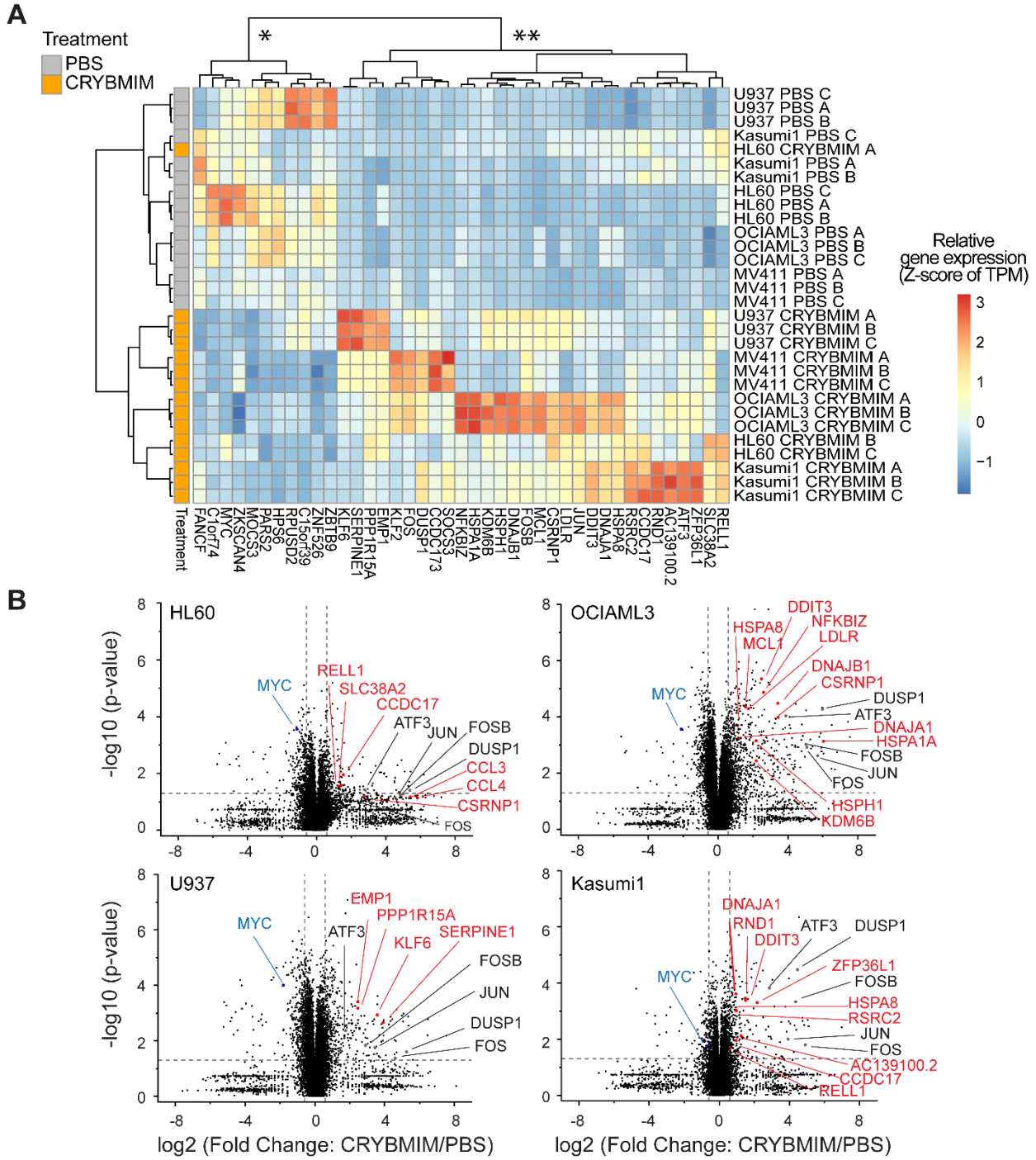

Figure 9-figure supplement 1. MYB transcription complexes induce shared and repress distinct gene expression programs in genetically diverse AML cells, as remodeled by peptidomimetic CRYBMIM inhibition. (A) Gene expression of five genetically diverse AML cell lines treated with 20 μM CRYBMIM (brown) as compared to PBS control (gray) for one hour, and measured by transcriptome RNA sequencing. Blue to red color gradient denotes relative gene expression of transcripts per million reads (TPM). Unsupervised clustering demonstrates gene sets that are repressed (*) and induced (**) by CRYBMIM and are shared and distinct among diverse AML cell lines, respectively, with top differentially expressed genes labeled. Data represent biological triplicates (A, B, C). **(B)** Volcano plots of differentially expressed genes following treatment with 20 μM CRYBMIM for one hour in genetically diverse AML cell lines. Vertical dashed lines denote relative changes in transcript abundance, and horizontal dashed line denotes statistical significance of biological triplicates (p = 0.05).

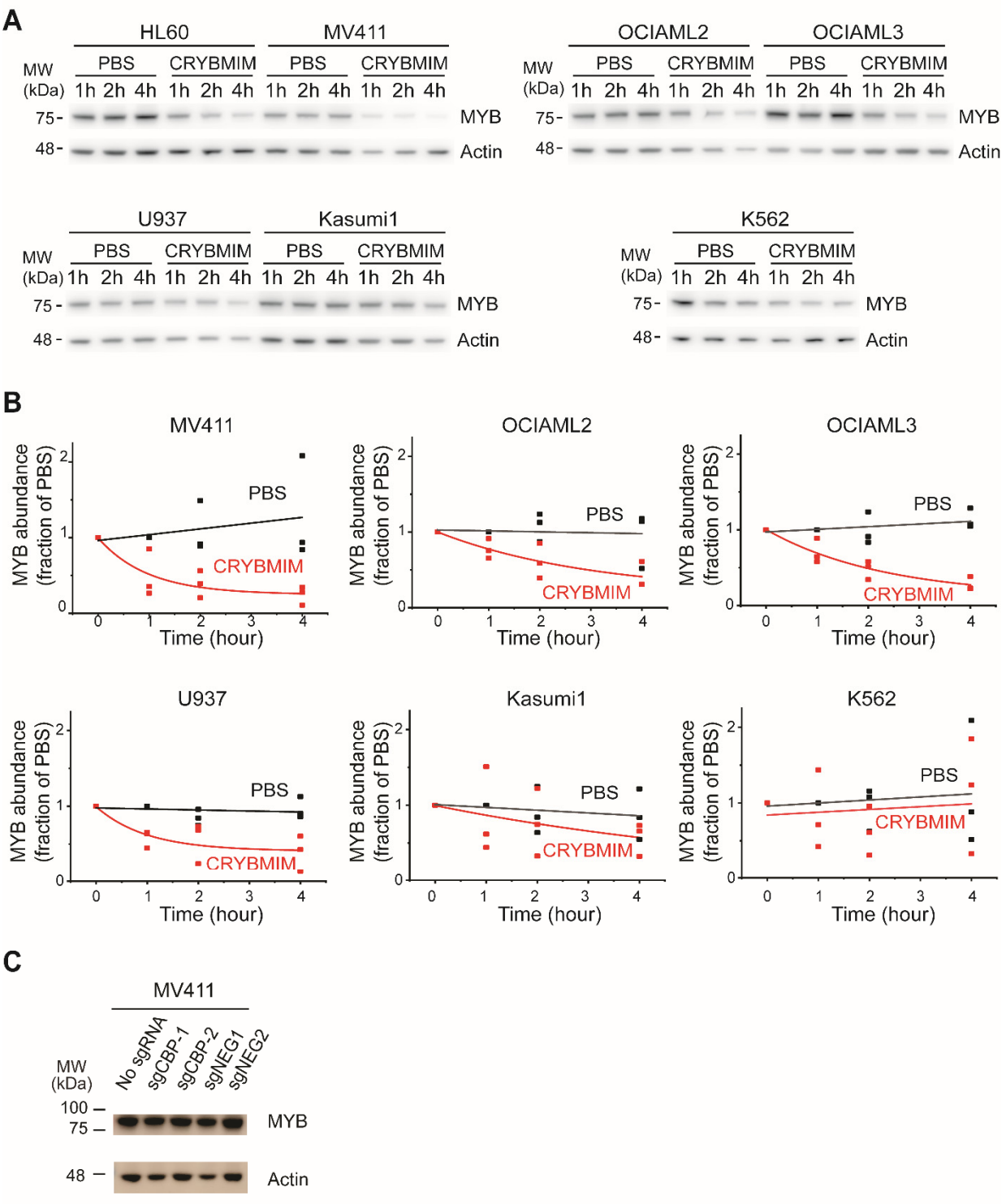

Figure 10-figure supplement 1. CRYBMIM causes MYB proteolysis with differential degradation rates in AML cells. (A-B) Western blots (A) and quantification of MYB protein abundance (B) in AML cells upon 1, 2, or 4 hours of 20 μM CRYBMIM (red) or PBS (black) treatment using image densitometry. Lines indicate single exponential fits. Actin serves as loading control. **(C)** Western blots demonstrating MYB protein abandunce in MV411 cells expressing sgCBP-1 and sgCBP-2 as comapred to control sgNEG1 and sgNEG2. Actin sereves as the loading control.

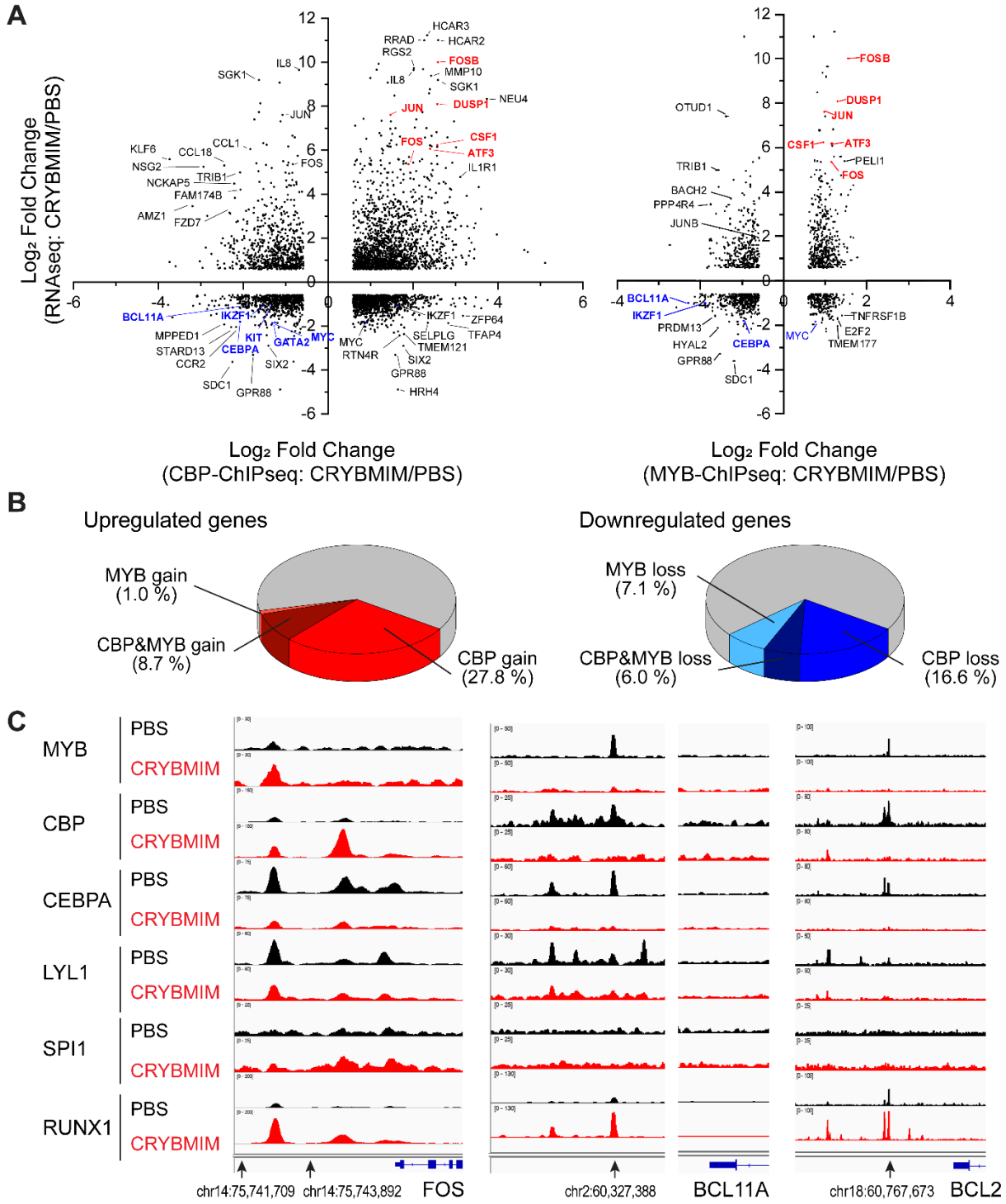

Figure 11-figure supplement 1. Oncogenic MYB transcription complexes sequester CBP/P300 to control AML gene expression. (A) Relative gene expression as measured by transcriptome RNA-seq as a function of relative chromatin occupancy of CBP/P300 (left) and MYB (right) as measured by ChIP-seq in MV411 cells treated with 20 μM CRYBMIM versus PBS control for four hours. Genes are labeled for greatest peak fold change > 1.5 and FDR < 0.1. **(B)** Distribution of upregulated (left) and downregulated (right) genes with respect to the relative gain (red) and loss (blue) chromatin occupancy of CBP/P300 and MYB. **(C)** Chromatin occupancy of specific factors in FOS (left), BCL11A (middle) and BCL2 (right) loci that are upregulated, downregulated and not changed, respectively, upon CRYBMIM (red) as compared to PBS control (black).

SUPPLEMENTAL FIGURE LEGENDS

Figure 1-figure_supplement 1. CBP depletion is dispensable in AML cells. Volcano plot showing the relative abundance of MOLM13-Cas9 cell clones expressing sgRNAs targeting specific genes (fold change of PBS-treated cells at T1 versus T0) and their statistical significance from biological replicates. Dashed line represents no enrichment, with positive values representing genes whose depletion confers relative resistance to MYBMIM. CBP is marked in red.

Figure 2-figure supplement 1. Molecular models of CREB and MLL structures in complex with CBP KIX, and CRYBMIM selectively binds to KIX domain in CBP/P300. (A) Molecular model of the CREB:KIX complex assembled in Maestro (Schrödinger) using PDB 1KDX showing phosphor-Serine 133. **(B)** Molecular model of the MLL:KIX complex assembled in Maestro (Schrödinger) using PDB 2LXS shown from the MYB/CREB binding site on KIX. **(C)** Molecular model of the MLL:KIX complex assembled in Maestro (Schrödinger) using PDB 2LXS rotated to show the full MLL peptide. **(D)** Sequence alignment of KIX domains in different human proteins. Identity/similarity of each set of sequences were 88%/96% (CBP vs P300), 21%/38% (CBP vs MED15) and 17%/34% (CBP vs RECQL5). **(E)** Western blots following affinity purification of MV411 nuclear extracts, showing specific binding of CBP/P300 but not MED15 to biotinylated CRYBMIM (Bio-CRYBMIM), immobilized on streptavidin beads. Purification with beads alone (Strept-empty) and LaminB1 serve as specificity controls.

Figure 3-figure supplement 1. CRYBMIM relatively spares normal hematopoietic progenitor cells in vitro. (A) Phase contrast photographs of MV411 and CD34+ cells isolated from human umbilical cord blood (CD34+ CB) and cultured in MethoCult H3040 with drug treatment, as indicated. **(B)** Colony forming ability of MV411 and CD34+ CB cells cultured in MethoCult H3040 following doxorubicin treatment. **(C)** Formation of BFU-E (light gray) and CFU-GM (gray) colonies of CD34+ CB cells cultured in MethoCult H3040 upon doxorubicin treatment. **(D)** Growth of MV411 and CD34+ CB cells upon CRYBMIM treatment in serum-containing suspension culture (IC_{50} = 6.9 ± 3.4 vs 13 ± 3.6 μM, p = 1.1e-15, ANOVA). Symbols represent biological triplicates.

Figure 3-figure supplement 2. Activity of CRYBMIM on non-hematopoietic cells. (A) Expression of MYB as a function of its genetic dependency in tumor cell lines, as assessed by DepMap. Red line represents linear correlation, with dashed lines showing 95% confidence intervals. **(B)** Cell viability assays of non-leukemia tumor and non-tumor cell lines treated with control PBS (black), 20 μM MYBMIM (gray), or 20 μM CRYBMIM (red) as indicated for 6 days with media replacement every 48 hours in three biological replicates.

Figure 4-figure supplement 1. Genetic dependencies of CRYBMIM susceptibility in AML cells. (A-C) Relative growth of GFP-expressing MOLM13 (A), MV411 (B), and K562 (C) cells expressing mCherry and unique sgRNAs targeting negative control *AAVS1* (sgNEG1 and

sgNEG2), positive control *CDK1* (sgCDK1), *CBP* (sgCBP-1 and sgCBP-2), and *P300* (sgEP300-1 and sgEP300-2) and quantified by FACS on days –3, 0, 3, and 6 upon sgRNA transduction. **(D)** Relative growth of K562-Cas9 cells expressing specific sgRNAs upon treatment with 20 μM CRYBMIM for two days (*p = 1.0e-6, **p = 1.3e-7; t-test for day 3 versus day 0).

Figure 5-figure supplement 1. CRYBMIM but not CREBMIM causes significant changes in gene expression in AML cells upon short duration exposure. (A-B) Gene expression of MYB target genes *MYC* (A) and *BCL2* (B) in AML after 20 μM peptide treatment as measured by qPCR. **(C)** Gene expression changes in MV411 cells treated with 20 μM CREBMIM for 4 hours as measured by RNA-seq.

Figure 6-figure supplement 1. CRYBMIM remodels MYB chromatin occupancies in AML cells. (A-B) Full lists of sequence motifs found in CRYBMIM-induced MYB-depleted (left) and MYB-enriched loci (right) after one hour treatment (A) and four hour treatment (B) of 20 μM CRYBMIM are shown.

Figure 7-figure supplement 1. CBP is the primary binding partner of MYB in AML cells. Sequence alignment of relevant CBP (top row) and P300 (bottom row) amino acids. Highlighted peptides identified in mass spectrometry analysis aligned to either CBP only (green) or both CBP and P300 (yellow).

Figure 9-figure supplement 1. MYB transcription complexes induce shared and repress distinct gene expression programs in genetically diverse AML cells, as remodeled by peptidomimetic CRYBMIM inhibition. (A) Gene expression of five genetically diverse AML cell lines treated with 20 μM CRYBMIM (brown) as compared to PBS control (gray) for one hour, and measured by transcriptome RNA sequencing. Blue to red color gradient denotes relative gene expression of transcripts per million reads (TPM). Unsupervised clustering demonstrates gene sets that are repressed (*) and induced (**) by CRYBMIM and are shared and distinct among diverse AML cell lines, respectively, with top differentially expressed genes labeled. Data represent biological triplicates (A, B, C). **(B)** Volcano plots of differentially expressed genes following treatment with 20 μM CRYBMIM for one hour in genetically diverse AML cell lines. Vertical dashed lines denote relative changes in transcript abundance, and horizontal dashed line denotes statistical significance of biological triplicates (p = 0.05).

Figure 10-figure supplement 1. CRYBMIM causes MYB proteolysis with differential degradation rates in AML cells. (A-B) Western blots (A) and quantification of MYB protein abundance (B) in AML cells upon 1, 2, or 4 hour of 20 μM CRYBMIM (red) or PBS (black) treatment using image densitometry. Lines indicate single exponential fits. Actin serves as loading control. (C) Western blots demonstrating MYB protein abundance in MV411 cells expressing sgCBP-1 and sgCBP-2 as compared to control sgNEG1 and sgNEG2. Actin serves as the loading control.

Figure 11-figure supplement 1. Oncogenic MYB transcription complexes sequester CBP/P300 to control AML gene expression. (A) Relative gene expression as measured by transcriptome RNA-seq as a function of relative chromatin occupancy of CBP/P300 (left) and MYB (right) as measured by ChIP-seq in MV411 cells treated with 20 μM CRYBMIM versus PBS control for four hours. Genes are labeled for greatest peak fold change > 1.5 and FDR < 0.1. **(B)** Distribution of upregulated (left) and downregulated (right) genes with respect to the relative gain (red) and loss (blue) chromatin occupancy of CBP/P300 and MYB. **(C)** Chromatin occupancy of specific factors in *FOS* (left), *BCL11A* (middle) and BCL2 (right) loci that are upregulated, downregulated and not changed, respectively, upon CRYBMIM (red) as compared to PBS control (black) treatment.

Source Data File Legends

Figure 1-source data 1

Genome-wide CRISPR knockout screen (GeCKO) gene summary.

Figure 5-source data 1

Differential gene expression analysis by RNA-seq in CRYBMIM, CREBMIM vs PBS treated MV411 cells (1 hour and 4 hours).

Figure 6-source data 1

Differentially occupied chromatin loci measured by MYB and CBP/P300 ChIP-seq in CRYBMIM vs PBS treated MV411 cells (1 hour and 4 hours).

Figure 7-source data 1

Lists of proteins identified by IP-MS of IgG control and MYB or CBP/P300 complex purifications from MV411 cell nuclei.

Figure 9-source data 1

All coding gene expression changes measured by RNA-seq in 1 hour CRYBMIM vs PBS treated 5 AML cell lines.

Figure 11-source data 1

Differentially increased or decreased peaks measured by multiple TF ChIP-seq in 1 hour CRYBMIM vs PBS treated MV411 cells.

Supplementary File Legends

Supplementary File 1. Key material detailed information.

1a. Peptide list. List of retro-inverso peptides with extinction coefficients.

1b. AML Cell line sequencing. Mutational landscape of human AML cell lines determined by whole genome sequencing

1c. sgRNA sequence list.

Supplementary File 2. Genom-wide CRISPR screen and Gene expression analysis.

2a. MYBMIM GeCKO CRISPR screen gene summary. Top 50 genes are shown. The complete tables are listed in Figure 1-source data 1 and Zenodo (DOI:10.5281/zenodo.4321824)

2b-e. Differentially expressed genes measured by RNA-seq in CRYBMIM, CREBMIM vs PBS-treated MV411 cells (1 hour and 4 hours). Top 50 differentially expressed genes in response to CRYBMIM are shown. The complete tables are listed in Figure 5-source data 1 and Zenodo (DOI:10.5281/zenodo.4321824).

2f. Gene set enrichment analysis (GSEA) for differentially expressed genes measured by RNA-seq in CRYBMIM, CREBMIM vs PBS-treated MV411 cells. Summary of GSEA on CRYBMIM-induced differentially expressed genes are shown. The complete tables are listed in Zenodo (DOI:10.5281/zenodo.4321824).

Supplementary File 3. IP-MS and ChIP-seq analysis.

3a. Protein lists identified by IP-MS of MYB and CBP complex purification from MV411 cell nuclei. Summary of identified proteins is shown. The complete tables are listed in Figure 7-source data 1 and Zenodo (DOI:10.5281/zenodo.4321824).

3b. MYB complex functional groups.

3c. Pathway analysis for 9 clusters of transcription factor-remodeled genes in response to CRYBMIM measured by ChIP-seq. Top 20 pathways in each cluster are shown. The complete tables are listed in Zenodo (DOI:10.5281/zenodo.4321824).

LISTS OF SUPPLEMENTAL DATA DEPOSITED IN ZENODO (DOI:10.5281/zenodo.4321824)

MYBMIM Genome-wide CRISPR screen (Figure 1)

01_MYBMIM_GeCKO_gene_summary.xlsx	Genome-wide GeCKO CRISPR screen in MYBMIM treated MOLM13 cells
02_Control_GeCKO_gene_summary.xlsx	Genome-wide GeCKO CRISPR screen in PBS treated MOLM13 cells

RNA-seq and GSEA with CRYBMIM and CREBMIB (Figure 5)

03_RNAseq_DESeq2_CRYBMIM_1hr-vs-PBS_1hr_SignificantAll.xlsx	Excel file of differentially expressed genes measured by RNA-seq in 1 hr CRYBMIM vs PBS treated MV411
04_RNAseq_DESeq2_CRYBMIM_4hr-vs-PBS_4hr_SignificantAll.xlsx	Excel file of differentially expressed genes measured by RNA-seq in 4 hr CRYBMIM vs PBS treated MV411
05_RNAseq_DESeq2_CREBMIM_1hr-vs-PBS_1hr_SignificantAll.xlsx	Excel file of differentially expressed genes measured by RNA-seq in 1 hr CREBMIM vs PBS treated MV411
06_RNAseq_DESeq2_CREBMIM_4hr-vs-PBS_4r_SignificantAll.xlsx	Excel file of differentially expressed genes measured by RNA-seq in 4 hr CREBMIM vs PBS treated MV411
07_gsea_report_for_na_pos_1552361301359_CRYBMIM-vs-PBS_1hr.xlsx	Gene set enrichment analysis for differentially expressed genes measured by RNA-seq in 1 hr CRYBMIM vs PBS (positive enrichment)
08_gsea_report_for_na_neg_1552361301359_CRYBMIM-vs-PBS_1hr.xlsx	Gene set enrichment analysis for differentially expressed genes measured by RNA-seq in 1 hr CRYBMIM vs PBS (negative enrichment)
09_gsea_report_for_na_pos_1552361302266_CRYBMIM-vs-PBS_4hr.xlsx	Gene set enrichment analysis for differentially expressed genes measured by RNA-seq in 4 hr CRYBMIM vs PBS (positive enrichment)

10_gsea_report_for_na_neg_1552361302266_CRYBMIM-vs-PBS_4hr.xlsx	Gene set enrichment analysis for differentially expressed genes measured by RNA-seq in 4 hr CRYBMIM vs PBS (negative enrichment)
11_gsea_report_for_na_pos_1552361302042_CREBMIM-vs-PBS_1hr.xlsx	Gene set enrichment analysis for differentially expressed genes measured by RNA-seq in 1 hr CREBMIM vs PBS (positive enrichment)
12_gsea_report_for_na_neg_1552361302042_CREBMIM-vs-PBS_1hr.xlsx	Gene set enrichment analysis for differentially expressed genes measured by RNA-seq in 1 hr CREBMIM vs PBS (negative enrichment)
13_gsea_report_for_na_pos_1552361302044_CREBMIM-vs-PBS_4hr.xlsx	Gene set enrichment analysis for differentially expressed genes measured by RNA-seq in 4 hr CREBMIM vs PBS (positive enrichment)
14_gsea_report_for_na_neg_1552361302044_CREBMIM-vs-PBS_4hr.xlsx	Gene set enrichment analysis for differentially expressed genes measured by RNA-seq in 4 hr CREBMIM vs PBS (negative enrichment)

ChIP-seq analysis for MYB and CBP (Figure 6 and 11)

15_ChIPseq_DESeq2_Named_SignificantIncrease_All_CRYBMIM-vs-PBS_1hr_MYB.xlsx	Differentially increased peaks measured by MYB ChIP-seq in 1hr CRYBMIM vs PBS treated MV411
16_ChIPseq_DESeq2_Named_SignificantDecrease_All_CRYBMIM-vs-PBS_1hr_MYB.xlsx	Differentially decreased peaks measured by MYB ChIP-seq in 1hr CRYBMIM vs PBS treated MV411
17_ChIPseq_DESeq2_Named_SignificantIncrease_All_CRYBMIM-vs-PBS_1hr_CBP.xlsx	Differentially increased peaks measured by CBP ChIP-seq in 1hr CRYBMIM vs PBS treated MV411
18_ChIPseq_DESeq2_Named_SignificantDecrease_All_CRYBMIM-vs-PBS_1hr_CBP.xlsx	Differentially decreased peaks measured by CBP ChIP-seq in 1hr CRYBMIM vs PBS treated MV411
19_ChIPseq_DESeq2_Named_SignificantIncrease_All_CRYBMIM-vs-PBS_4hr_MYB.xlsx	Differentially increased peaks measured by MYB ChIP-seq in 4hr CRYBMIM vs PBS treated MV411

20_ChIPseq_DESeq2_Named_SignificantDecrease_All_CRYBMIM-vs-PBS_4hr_MYB.xlsx	Differentially decreased peaks measured by MYB ChIP-seq in 4hr CRYBMIM vs PBS treated MV411
21_ChIPseq_DESeq2_Named_SignificantIncrease_All_CRYBMIM-vs-PBS_4hr_CBP.xlsx	Differentially increased peaks measured by CBP ChIP-seq in 4hr CRYBMIM vs PBS treated MV411
22_ChIPseq_DESeq2_Named_SignificantDecrease_All_CRYBMIM-vs-PBS_4hr_CBP.xlsx	Differentially decreased peaks measured by CBP ChIP-seq in 4hr CRYBMIM vs PBS treated MV411

MYB and CBP IP-MS data (Figure 7)

23_IP-MS_MYB_IgG_protein list.xlsx	List of proteins identified by IP-MS of IgG control and MYB complex purifications from MV411 cell nuclei
24_IP-MS_CBP_IgG_protein_list.xlsx	List of proteins identified by IP-MS of IgG control and CBP complex purifications from MV411 cell nuclei

RNA-seq analysis with CRYBMIM in 5 AML cell lines (Figure 9-figure supplement 1)

25_RNAseq_expression_all_coding_5AML_celllines.xlsx	All coding gene expression changes measured by RNA-seq in 1 hr CRYBMIM vs PBS treated MV411, HL-60, Kasumi-1, OCI-AML3 and U937

ChIP-seq anaysis for multiple TFs (Figure 11)

26_ChIPseq_DESeq2_FilteredNormalizedCounts_PeakNorm_CRYBMIM-vs-PBS_1hr_allTFs.xlsx	Differentially increased peaks measured by multiple TF ChIP-seq in 1hr CRYBMIM vs PBS treated MV411
27_ChIPseq_pathway_analysis_9 clusters.xlsx	Pathway analysis for 9 clusters of transcription factor-remodeled genes measured by ChIP-seq

APPENDIX

Key Resources Table				
Reagent type (species) or resource	**Designation**	**Source or reference**	**Identifiers**	**Additional information**
cell line (*Homo-sapiens*)	MV411	ATCC	Cat# CRL-9591, RRID:CVCL_0064	
cell line (*Homo-sapiens*)	MOLM13	DSMZ	Cat# ACC-554, RRID:CVCL_2119	
cell line (*Homo-sapiens*)	OCIAML2	DSMZ	Cat# ACC-99, RRID:CVCL_1619	
cell line (*Homo-sapiens*)	THP1	ATCC	Cat# TIB-202, RRID:CVCL_0006	
cell line (*Homo-sapiens*)	NB4	DSMZ	Cat# ACC-207, RRID:CVCL_0005	
cell line (*Homo-sapiens*)	Kasumi1	ATCC	ATCC Cat# CRL-2724, RRID:CVCL_0589	
cell line (*Homo-sapiens*)	HEL	ATCC	Cat# TIB-180, RRID:CVCL_2481	
cell line (*Homo-sapiens*)	OCIAML3	DSMZ	Cat# ACC-582, RRID:CVCL_1844	
cell line (*Homo-sapiens*)	SKM1	DSMZ	Cat# ACC-547, RRID:CVCL_0098	
cell line (*Homo-sapiens*)	U937	ATCC	Cat# CRL-1593.2, RRID:CVCL_0007	

cell line (*Homo-sapiens*)	HL60	ATCC	Cat# CCL-240, RRID:CVCL_0002	
cell line (*Homo-sapiens*)	K562	ATCC	Cat# CCL-243, RRID:CVCL_0004	
antibody	anti-v-Myb + c-Myb (phospho S11) (Rabbit monoclonal, EP769Y)	Abcam	Cat# ab45150, RRID: AB_778878	IP (7.5 µg for 100 million cells)
antibody	anti-c-Myb (Rabbit monoclonal, D1B9E)	Cell Signaling Technology	Cat# 59995, RRID: AB_2799836	WB (1:1000)
antibody	anti-CBP (Rabbit monoclonal, D9B6)	Cell Signaling Technology	Cat# 7425, RRID: AB_10949975	WB (1:500-1000), IP (15 µg for 100 million cells)
antibody	anti-CBP (Rabbit polyclonal, PA1-847)	Invitrogen	Cat# PA1-847, RRID: AB_2083939	WB (1:500-1000)
antibody	anti-p300 (Rabbit monoclonal, D8Z4E)	Cell Signaling Technology	Cat# 86377, RRID: AB_2800077	WB (1:500)
antibody	anti-RUNX1 (Rabbit monoclonal, D33G6)	Cell Signaling Technology	Cat# 4336, RRID: AB_10859035	WB (1:1000)
antibody	anti-RUNX1 (Mouse monoclonal, 1C5B16)	BioLegend	Cat# 659302, RRID: AB_2563194	WB (1:1000)
antibody	anti-LYL1 (Mouse monoclonal, C-4)	Santa Cruz Biotechnology	Cat# sc-374164, RRID: AB_10986408	WB (1:500)
antibody	anti-SATB1 (Rabbit monoclonal, P472)	Cell Signaling Technology	Cat# 3643, RRID: AB_2184328	WB (1:1000)

antibody	anti-E2A (Rabbit monoclonal, D2B1)	Cell Signaling Technology	Cat# 12258, RRID: AB_2797860	WB (1:1000)
antibody	anti-CEBPA (Rabbit monoclonal, D56F10)	Cell Signaling Technology	Cat# 8178, RRID: AB_11178517	WB (1:1000)
antibody	anti-CEBPA (Mouse monoclonal, G-10)	Santa Cruz Biotechnology	Cat# sc-166258, RRID: AB_2078042	WB (1:500)
antibody	anti-SPI1 (Rabbit monoclonal)	Cell Signaling Technology	Cat# 2266, RRID: AB_10692379	WB (1:1000)
antibody	anti-LDB1 (Rabbit polyclonal)	Cell Signaling Technology	Cat# 55476, RRID: AB_2799486	WB (1:1000)
antibody	anti-LMO2 (Rabbit monoclonal, E8K6I)	Cell Signaling Technology	Cat# 87182, RRID: NA	WB (1:1000)
antibody	anti-c-Jun (Rabbit monoclonal, 60A8)	Cell Signaling Technology	Cat# 9165, RRID: AB_2130165	WB (1:1000)
antibody	anti-β-Actin (Mouse monoclonal, 8H10D10)	Cell Signaling Technology	Cat# 3700, RRID: AB_2242334	WB (1:5000)
antibody	anti-β-Actin (Rabbit monoclonal, 13E5)	Cell Signaling Technology	Cat# 4970, RRID: AB_2223172	WB (1:5000)
antibody	anti-Lamin B1 (Mouse monoclonal, A-11)	Santa Cruz Biotechnology	Cat# sc-377000, RRID: AB_2861346	WB (1:500)
antibody	anti-Lamin B1 (Rabbit monoclonal, HRP Conjugate, D9V6H)	Cell Signaling Technology	Cat# 15068, RRID: AB_2798695	WB (1:1000)

antibody	anti-MED15 (Rabbit polyclonal)	Bethyl	Cat# A302-422A, RRID: AB_1907305	WB (1:2000)
recombinant DNA reagent	Human CRISPR Knockout Pooled Library GeCKO v2	Sanjana et al., 2014	Addgene Pooled Library #1000000049	
recombinant DNA reagent	LRG2.1 (U6-sgRNA-GFP) (Plasmid)	Tarumoto et al., 2018; Lu et al., 2018	Addgene Plasmid #108098, RRID:Addgene_108098	
recombinant DNA reagent	LRC2.1 (U6-sgRNA-mCherry) (Plasmid)	Tarumoto et al., 2018; Lu et al., 2018	Addgene Plasmid #108099, RRID:Addgene_108099	
recombinant DNA reagent	LentiV_Cas9_Blast (Plasmid)	Tarumoto et al., 2020	Addgene Plasmid #125592, RRID:Addgene_125592	
recombinant DNA reagent	LentiV_Cas9_puro (EFS-Cas9-P2A-Puro) (Plasmid)	Tarumoto et al., 2018; Lu et al., 2018	Addgene Plasmid #108100, RRID:Addgene_108100	
recombinant DNA reagent	MSCV-BCL2-IRES-GFP (Plasmid)	Sanda et al., 2013	RRID:N.A.	
sequence-based reagent	sgCBP-1; sgCBP-2; sgEP300-1; sgEP300-2; sgCDK1; sgNEG1; sNEG2	Tarumoto et al., 2018; Lu et al., 2018	RRID:N.A.	sgRNAs See Supplementary file 1c
peptide, recombinant protein	MYBMIM	Ramaswamy et al., 2018	RRID:N.A.	See Supplementary file 1a
peptide, recombinant protein	CRYBMIM; CREBMIM; CG3; TG3; MLLMIM	This study	RRID:N.A.	See Supplementary file 1a

peptide, recombinant protein	Bio-CRYBMIM; Bio-CREBMIM; FITC-CRYBMIM; FITC-CREBMIM	This study	RRID:N.A.	See Supplementary file 1a
peptide, recombinant protein	RI-TAT	This study	RRID:N.A.	See Supplementary file 1a
commercial assay or kit	CellTiter-Glo Luminescent Cell Viability Assay	Promega	G7571	
commercial assay or kit	CD34 MicroBead Kit UltraPure, human	Miltenyi Biotech	130-100-453	
commercial assay or kit	Dynabeads Antibody Coupling Kit	Thermo Fisher	14311D	
chemical compound, drug	Doxorubicin	Sigma Aldrich	D1515	
software, algorithm	DepMap 19Q4	Cancer Dependency Map Portal	RRID:SCR_017655	
software, algorithm	EMBOSS Needle	European Bioinformatics Institute	RRID:SCR_004727	Alignment of protein sequences
software, algorithm	MacroModel	Schrodinger	RRID:SCR_014879	Force Field-based Molecular Modeling
software, algorithm	MAGeCK	W. Li et al., 2014	RRID:N.A.	Genome-wide CRISPR screen
software, algorithm	MaxQuant (version 1.6.0.16)	Max planck institute of biochemistry	RRID:SCR_014485	mass-spectrometric data analysis

software, algorithm	trim_galore	Babraham Institute	RRID:SCR_011847	ChIP-seq data analysis
software, algorithm	bowtie2	Johns Hopkins University	RRID:SCR_016368	ChIP-seq data analysis
software, algorithm	BEDTools suite	Quinlan AR and Hall IM, 2010, Bioinformatics	RRID:SCR_006646	ChIP-seq data analysis
software, algorithm	MACS 2.0	Zhang et al., 2008, Genomebiol	RRID:SCR_013291	ChIP-seq data analysis
software, algorithm	CollectRNASeqMetrics	Picard tool	RRID:SCR_006525	RNA-seq data analysis
software, algorithm	HTSeq v0.6.1.	Fabio Zanini et al., 2021, Simon Anders, Paul Theodor Pyl, Wolfgang Huber, 2014	RRID:SCR_005514	RNA-seq data analysis
software, algorithm	DESeq2	Bioconductor	RRID:SCR_015687	RNA-seq and ChIP-seq data analysis
software, algorithm	UCSC knownGene	Meyer et al., 2013	RRID:SCR_005780	RNA-seq data analysis
software, algorithm	Ensembl 71	Flicek et al., 2013	RRID:SCR_002344	RNA-seq data analysis

software, algorithm	MISO v.2.0	Katz et al., 2010	RRID:SCR_003124	RNA-seq data analysis
software, algorithm	RSEM v.1.2.4	B. Li & Dewey, 2011	RRID:SCR_013027	RNA-seq data analysis
software, algorithm	Bowtie v.1.0.0	Langmead et al., 2009	RRID:SCR_005476	RNA-seq data analysis
software, algorithm	TopHat v.2.1.1	Trapnell et al., 2009	RRID:SCR_013035	RNA-seq data analysis
software, algorithm	TMM method	Robinson & Oshlack, 2010	RRID:SCR_012802 (edgeR)	RNA-seq data analysis
software, algorithm	pheatmap package	Kolde, 2012/2020	RRID:SCR_016418	RNA-seq data analysis
software, algorithm	R programming environment with Bioconductor	Huber et al., 2015	RRID:SCR_001905	RNA-seq data analysis
software, algorithm	dplyr	Wickham et al., 2020	RRID:SCR_016708	RNA-seq data analysis
software, algorithm	ggplot2	Wickham, 2016	RRID:SCR_014601	RNA-seq data analysis
software, algorithm	RStudio	RStudio	RRID:SCR_000432	Statistical analysis
software, algorithm	ImageJ	Fiji	RRID:SCR_002285	Image processing
software, algorithm	FCS express 7	De Novo	RRID:SCR_016431	Flow cytometry data analysis

software, algorithm	OriginPro 2018	OriginLab	RRID:SCR_014212	Statistical analysis